CHARACTERIZATION OF HYDROTHERMAL MINERALS IN UP-FLOW, OUT-FLOW AND COLD IN-FLUX ZONES IN OLKARIA GEOTHERMAL SYSTEM USING SWIR HYPERSPECTRAL IMAGING TECHNIQUE.

KAMAU MATHEW WAWERU

February 2019

SUPERVISORS:

Dr. Chris Hecker

Dr. Caroline Lievens

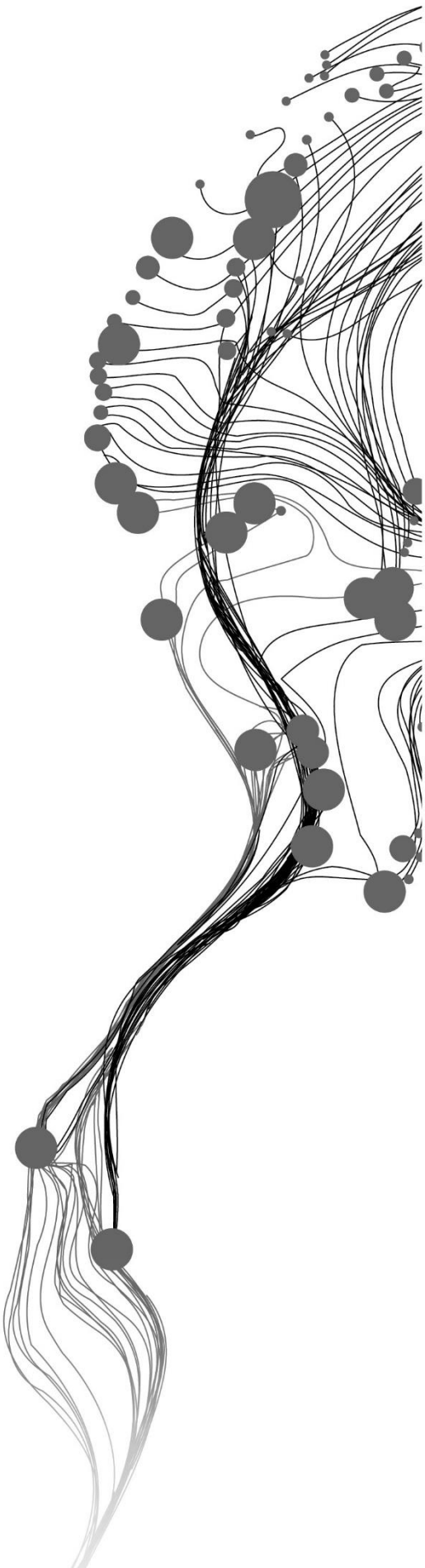

CHARACTERIZATION OF HYDROTHERMAL MINERALS IN UP-FLOW, OUT-FLOW AND COLD IN-FLUX ZONES IN OLKARIA GEOTHERMAL SYSTEM USING SWIR HYPERSPECTRAL IMAGING TECHNIQUE.

KAMAU MATHEW WAWERU
Enschede, The Netherlands, FEBURUARY 2019

Thesis submitted to the Faculty of Geo-Information Science and Earth Observation of the University of Twente in partial fulfilment of the requirements for the degree of Master of Science in Geo-information Science and Earth Observation.
Specialization: Applied Earth Sciences in Geological Remote Sensing

SUPERVISORS:
Dr. Chris Hecker
Dr. Caroline Lievens

THESIS ASSESSMENT BOARD:
Prof.dr.Mark van der Meijde(Chair)
Dr. Fred Beekman (External Examiner, Utrecht University)

ABSTRACT

Hydrothermal minerals and mineral assemblages formed in a geothermal system provide information on both present and past geothermal reservoir conditions. Besides being used for inferring formation temperature and fluid composition, hydrothermal alteration minerals can also be used to interpret hydrologic structure by locating zones of up-flow, out-flow and cold in-flux zones in a geothermal system. In addition, fast identification and analysis of hydrothermal alteration minerals can be used to address challenges during drilling process. In Olkaria geothermal system, identification and characterization of hydrothermal minerals is commonly done using conventional methods such as binocular microscopes, petrography and XRD. These methods require lengthy sample preparation procedure and analysis thus making it difficult for timely use of data acquired to address on-site drilling challenges. This study utilized SWIR hyperspectral imaging technique to identify and characterize hydrothermal alteration minerals from three geothermal wells in Olkaria geothermal system. A total of 135 images were acquired from drill cuttings samples in three wells. Pre-processing steps first involved calibration with dark and white reference images in order to convert sample images into reflectance. Hydrothermal mineral spectra were identified by comparing them with USGS spectral library, TSG software and GMEX spectral identification field manual. For mineral quantification, endmember spectra were collected using the wavelength mapping algorithm in HypPy3 software. Mineral classification was done using SAM classification algorithm. Validation of the SWIR identified minerals was done using XRD measurements on selected samples. Identified minerals and mineral assemblages generally corroborated with the hypothesized up-flow, out-flow and cold-influx zones. Generally, low-temperature indicator minerals such as zeolite and smectite were formed at shallow depth while low high-temperature indicator minerals formed at deeper level. High-temperature indicator minerals identified in zone of cooling were interpreted as relict. Compositionally, illite is predominantly phengite with Al^{3+} species being replaced by Fe^{2+} and/or Mg^{2+} while chlorite is predominantly Fe-rich in all the three wells studied. There was high variation in illite crystallinity per sample with high variance being observed in zones experiencing temperature reversal.

ACKNOWLEDGMENTS

I would like first to thank God for giving me the strength and ability to complete this study.

Many thanks to NUFFIC for granting me a fellowship in Netherlands Fellowship Programme(NFP) to enable me to pursue an MSc course in Geo-information Science and Earth Observation for Applied Earth Sciences with specialization in Geological remote sensing. Special appreciation to my employer Kenya Electricity Generating Company(KENGEN) for providing me with study leave to pursue further studies at the University of Twente, ITC, Netherlands.

Special thanks and appreciation to my supervisors Dr. Chris Hecker and Dr. Caroline Lievens for their continuous support, motivation and patience during this research period. Your guidance and knowledge you have imparted to me was not only significant for this research but also for future application as i navigate through this career path.

Much appreciation to KENGEN for allowing me to use company data to achieve the objective of this study. This is extended to my colleagues at the Geology section for facilitating quick repackaging and despatch. Special thanks to Senior geologist Joyce Okoo for allowing and facilitating this to happen smoothly. May God bless you all abundantly.

Special thanks to CRADO Mr. Kizito Opondo for your invaluable advice during geothermal wells selection phase. Your advice is highly appreciated. Equally, am grateful to Mr. Victor Otieno for the advice, comments and time for making sure the whole of this thesis period was successful. May God bless you abundantly. Special thanks to all workmates who contributed in one way or another for the success of this research.

To my fellow students, you had been of encouragement to me and the support we accorded each other in tackling challenges was motivating and encouraging. I will always remember you.

My deepest gratitude to my wife Judy, my sons Ian, Melvin and Jayden for the encouragement and endurance during the entire 18 months period. For sure, it was not easy and without your moral support i couldn't have made it. May almighty God bless you abundantly. Special thanks to my mother, brothers and sister together with all my entire family members for the prayers, support and encouragement. May God bless you abundantly.

Lastly, i would like to dedicate this thesis to my late father Boniface Kamau because it is through his advice on value of education has made me come all this along. May his soul RIP.

TABLE OF CONTENTS

LIST OF FIGURES

LIST OF TABLES

1. INTRODUCTION

1.1. Background information

Geothermal resources are formed by natural heat produced by either magma cooling at depth, high surface heat flow due to thinning crust or by decay reaction of radioactive elements (Lund et al, 2006). High-temperature geothermal resources mostly occur in regions of active or recently active volcanism (Henley & Ellis, 1983). Abnormally high heat flow in these regions causes thermal convection of groundwater leading to the formation of geothermal resources at the interface of the hot fluids and the surface (Khodayar et al., 2010). At the surface, the resource can be exploited for either direct or indirect (electricity generation) use.

In a geothermal system, an up-flow zone occurs when hydrothermal fluids ascent through permeable geological structures to reach or near the earth's surface. Correspondingly, an out-flow zone is generated when fluid at the surface flow laterally due to the hydrologic gradient (Skord et al., 2011). Moreover, in up-flow zones, temperature increase with depth while in out-flow zones, it decreases with depth. On the other hand, cold water incursion occurs when cooler groundwater percolates into the system through subsurface structures causing cooling-effect in the potential up-flow zones and ultimately changing the system environment (Cumming, 2009). These zones are structurally controlled, thus permit both the percolation for the meteoric water and convection along the fault system (Moeck, 2014).

Identification and interpretation of hydrothermal mineral assemblages is an important aspect of surface and sub-surface exploration of the geothermal resource (Milicich et al., 2015). They provide insight into the present and/or past nature of the geothermal reservoir. Hydrothermal alteration minerals are formed as a result of rock alteration by circulating hot water in the Earth's crust and is controlled by variations in temperature, pressure and fluid composition (Inoue, 1995). Therefore, gaining information such as formation temperatures, chemical compositions and alteration intensity of alteration minerals is fundamental to locating cold water in-flux zones, pathways for up-flow fluids as well as delineating margins of geothermal systems (Reyes, 1990).

Conventionally, hydrothermal minerals are best identified by the aid of analytical techniques which encompass but not limited to the binocular microscope, petrographic microscope, scanning electron microscope and X-ray diffractometer (XRD) analyses. Most recently, Infrared reflectance(IR) spectroscopy is increasingly being used with varying levels of success as an exploration tool in the mining industry (Kruse, 1996 & Taylor, 2000) and to a lesser extent for geothermal exploration (Calvin & Pace, 2016). This technique rapidly collects mineralogical information particularly alteration minerals that are difficult to distinguish in hand sample, binocular or by petrographic methods (Calvin & Pace, 2016). It works by the acquisition of reflectance spectra within Visible Near Infrared(VNIR)-Short Wave Infrared (SWIR) with a wavelength range of between 350-2500 nm in the electromagnetic spectrum (Mathieu et al., 2017).

Typically, SWIR spectroscopy involves the detection of the reflected energy modulated by molecular bond vibrations within the 1300-2500 nm wavelength range. In this range, some minerals exhibit characteristic spectra with diagnostic features as a result of bending and stretching of certain molecules and radicals within the mineral crystal lattice such as OH, H_2O, NH_4, CO_3 and metal-OH bonds(e.g., Al-OH, Fe-OH, and Mg-OH) (Pontual et al., 1997). Each molecular group has characteristics absorption features occurring at a specific wavelength range. For instance, Thompson et al. (1999), showed the occurrence of OH and H_2O features at 1400 nm, H_2O at 1900 nm and diagnostic features related to Al-OH, Fe-OH and Mg-OH occurring at 2200 nm, 2250 nm and 2330 nm respectively.

Although field-based SWIR spectroscopy gives comprehensive information on the alteration mineral assemblages, identification and quantification of mineral abundances in an intimate mineral mixture is quite challenging. This is especially true for minerals that are not spectrally dominating the mixed reflectance spectrum. However, recent development of laboratory-based SWIR hyperspectral imaging sensors allows rapid analyses and the creation of high-resolution mineral maps. After that, mineral maps generated can be used for determining relative proportions of mineral mixtures in rock samples (Zaini et al., 2014). The technique combines both spectral and spatial imaging methods by acquiring images with a high number of contiguous spectra which allow spectral analysis of each discrete pixel thus compositionally distinguishing them (Goetz et al., 1985). It enables surface scanning of the sample hence enabling new investigations and yield in a novel or unexpected mineralogical and petrological insight into a variety of geological processes (Thomas & Walter, 2002).

1.2. The significance of Hydrothermal alteration minerals in a geothermal system

Study of hydrothermal minerals plays a significant role in exploration, characterization, exploitation and development of geothermal resources. Together with data from other scientific disciplines (e.g. geochemistry, well reservoir conditions, structural geology, stratigraphy), hydrothermal minerals can assist in the development of a conceptual model by defining zones of up-flow, out-flow and areas of cold-water incursions (Reyes, 1990). As highlighted by Skord et al. (2011), identification and delineating these zones is critical as the most productive portion of a geothermal system is usually in the up-flow zone. Therefore, the main focus during exploration and production drilling is to target zones with faults associated with up-flow of hot geothermal fluids. Equally, hydrothermal alteration information can assist in setting the various types of the casing in respect to temperature, permeability and cooler zones and predicting drilling challenges such as stuck drill pipes caused by swelling clays (e.g., smectite) during the drilling process. Ultimately, information derived from hydrothermal minerals studied can be used to define the best areas to site both production and re-injection wells as well as the best way to exploit the existing resource sustainably.

1.3. Studies in Olkaria geothermal systems

Several studies have been done on hydrothermal alteration minerals in Olkaria geothermal systems. Muchemi (1987); Omenda (1998) and Lagat (2007), identified, opaline, quartz, calcite, siderite, calc-silicates, clays, zeolite, pyrite, and albite minerals in various sub-fields of the greater Olkaria geothermal systems. Practically, all these studies were based on the examination of drill cores/cutting using binocular and petrographic microscopes, XRD and fluid inclusion analyses. Together with data from other disciplines, Ofwona (2002) used hydrothermal minerals to infer the existence of three up-flow zones in Olkaria geothermal system. Similarly, Ronoh (2015) indicated the presence of up-flow zones and cold in-flux zones at Olkaria Domes sub-field.

1.4. Problem Statement

Although much has been studied about hydrothermal minerals in the Olkaria geothermal system using conventional methods listed above*(section 1.2)*, most of the studies focused on the identification, occurrence depths and alteration characteristics of hydrothermal alteration minerals. Research on mineral mixtures, composition variations, crystallinity and quantification of hydrothermal minerals relative to depth is insufficient. Besides, these methods involve complex sample preparation and analysis procedures and thus only a limited number of samples can be analyzed at one go (Taylor, 2000). Consequently, results derived from these methods provide much-delayed solutions for challenges arising during the drilling process(e.g., stuck drill pipes due to swelling clays) and therefore more useful for post-drilling studies.

In addition, though XRD technique is widely used and capable of discriminating between minerals, Brindley (1955) pointed out its ineffectiveness to identify and distinguish chemical species of minerals. The technique also has the inability to identify and map minerals with poor crystallinity or with small crystal size. Therefore,

this research will employ SWIR hyperspectral imaging spectroscopy technique to determine and estimate mineral composition, crystallinity and relative abundance of mineral mixtures in geothermal drill cuttings. This data can then be used to acquire comprehensively fundamental well information within a limited time frame. Subsequently, information derived can then be used to infer the prevailing sub-surface conditions such as reservoir temperature, fluid source and relative abundance of swelling clays.

1.5. Objectives

The general objective of this research is to evaluate the usability of SWIR imaging spectroscopy technique on drill cuttings in solving potential drilling challenges and improving understanding of Olkaria geothermal system.

1.5.1. Specific Objectives & Research Questions

The specific objectives and research questions of the research are:

- To identify hydrothermal minerals and mineral assemblages associated with up-flow, out-flow and cold in-flux wells.
    - Is there difference in hydrothermal minerals and assemblages mapped in these zones?
    - If yes, which hydrothermal minerals and assemblages are associated with each zone?
    - Are there previously unreported hydrothermal minerals revealed using SWIR imaging technique?
- To establish the variation in mineralogical assemblages along the wellbore.
    - What factors control the variation in alteration mineralogy within the three zones? Is it temperature, permeability or host lithology related?
    - How does relative abundance of minerals vary downhole?

- To identify changes in chemical composition and crystallinity in different hydrologic zones which could be derived using SWIR hyperspectral imaging technique.
    - Is there difference in mineral crystallinity?
    - What is the difference in chemical composition between different hydrothermal minerals? e.g. Fe or Mg-rich chlorite or variety of white mica (illite, muscovite)

1.6. Hypothesis

- Different mineral assemblages to be formed in each of the three hydrologic zones.
- Depth experiencing temperature reversal or cold influxes to have low abundance/absent SWIR active minerals.
- The absorption features of spectral reflectance characteristics of the drill cuttings samples in the SWIR region indicates change in temperature and permeability.

1.7. Datasets, Softwares and Research setups

1.7.1. Datasets

Datasets and materials required for this study was collected during field visit at Olkaria geothermal field in Kenya. It included the following;

- Drill cuttings.
- XRD data.
- Down hole temperature data.
- Licensed geothermal fields and well locations shape files.
- Internal Company reports.
- Geological map of the area.

1.7.2. Software's

- ArcGIS
- ENVI-IDL
- HypPy3
- The spectral geologist (TSG)

ENVI 5.2 was mainly used for hyperspectral image analysis while HypPy3 was mainly used for image pre-processing and processing. ArcGIS 10.5.1 was used for making the maps of the study area and plotting the location of the geothermal wells. TSG was used to analyze and interpret spectral data derived from the image spectra.

1.7.3. Research setup

The research has been conducted as an integrated process that involved the following methods:

- Literature review: This was done to understand the geology and the geological setting of the area. In addition, it was done to know hydrothermal minerals identified by previous studies in the area and to understand the link between the geology and the hydrothermal mineralogy in the area.
- Field site visit (between 21st September-12th October,2018): Involved drill cuttings and auxiliary data collection necessary for this study.
- Laboratory measurements: Involved acquisition of drill cutting images using SWIR camera at Geoscience Laboratory(ITC laboratories).
- Hyperspectral images pre-processing, processing, analysis and interpretation.
- Data integration: Involved integration of lithology and temperature data with the spectral data to know the relationship between lithology and temperature with spectral information.

1.8. Thesis Structure

- Chapter 1 emphasizes on the research problem, general objective, specific objectives, research questions, hypothesis, datasets and softwares used for the research.
- Chapter 2 deals with the literature review about study area location, geology(surface and subsurface), geological setting and a review on the use of infrared spectroscopy in mapping hydrothermal minerals.
- Chapter 3 describes dataset, instrumentation, and methodology used for this research in terms of processing and analysis of the data.
- Chapter 4 present the results achieved from the various methods used.
- Chapter 5 deals with the result discussion which involves the relationship between hydrothermal alteration minerals identified and hydrologic zones.
- Chapter 6 describes the conclusion and recommendations of this study.

1.9. Research methodology flow chart

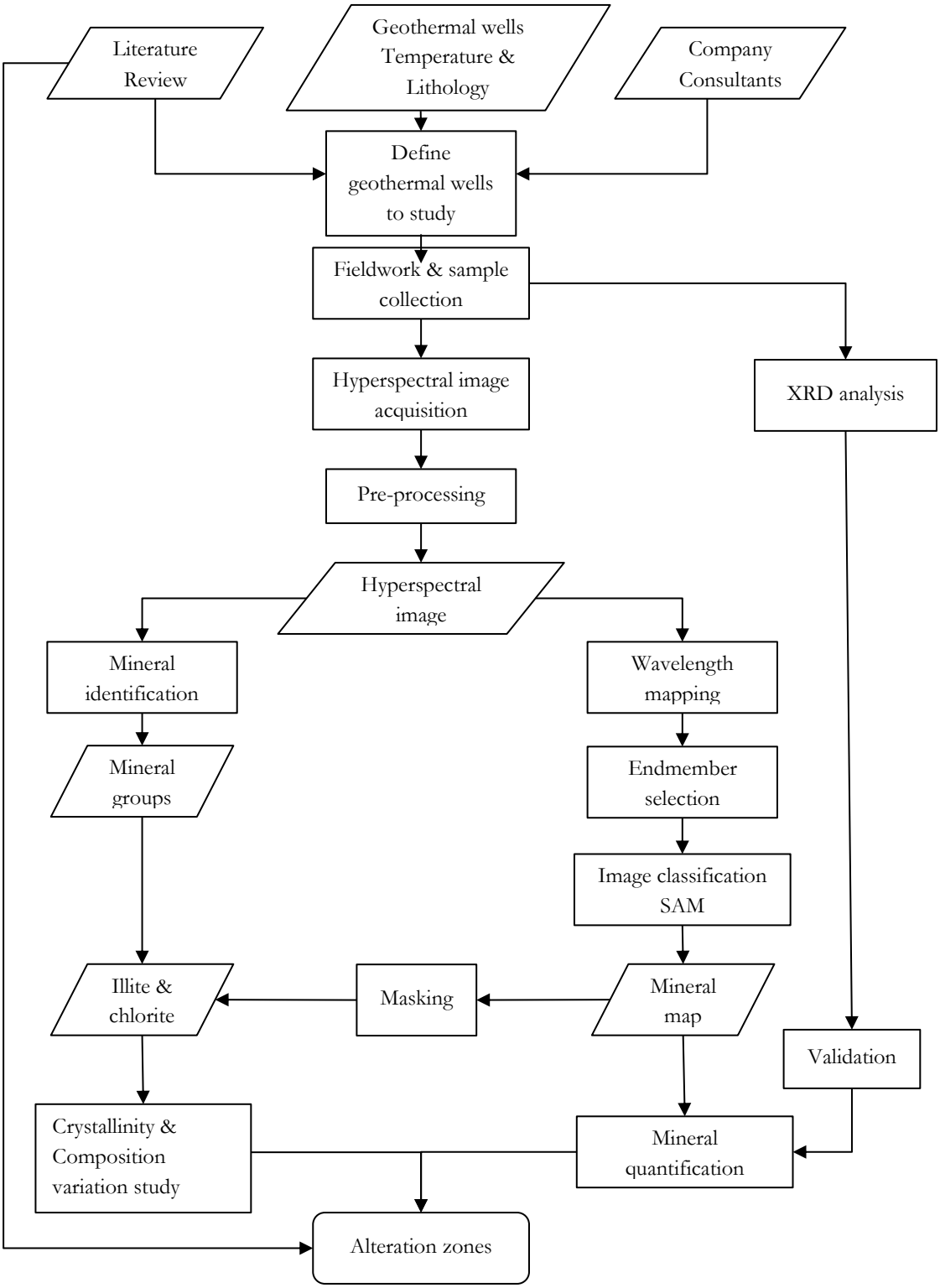

Figure 1-1: Flow chart.

2. LITERATURE REVIEW

This chapter presents collection of relevant information about the geology, geological setting, structural geology of the study area, hydrothermal minerals associated with geothermal systems and SWIR reflectance study of minerals in a geothermal system.

2.1. Location of the Study Area

Olkaria geothermal field is located in Kenyan Rift valley to the south of Lake Naivasha about 120 km NW of Nairobi(Figure 2-1). It is a high-temperature geothermal system with an approximate area of about 240 km^2. The geothermal system is associated with one of the several volcanic centers situated within the Kenyan Rift which includes amongst them Longonot, Eburru, Suswa, Menengai and Silali (Ofwona, 2002). Production in the field began in the early 1980s with the installation of 45MWe power plant. To date close to 300 wells have been drilled with a depth range of between 1000-3600m. The installed aggregate capacity of the field is estimated at 688 MWe. It has been divided into seven sub-fields with Olkaria Hill a prominent geological feature being the reference point (Otieno, 2016).

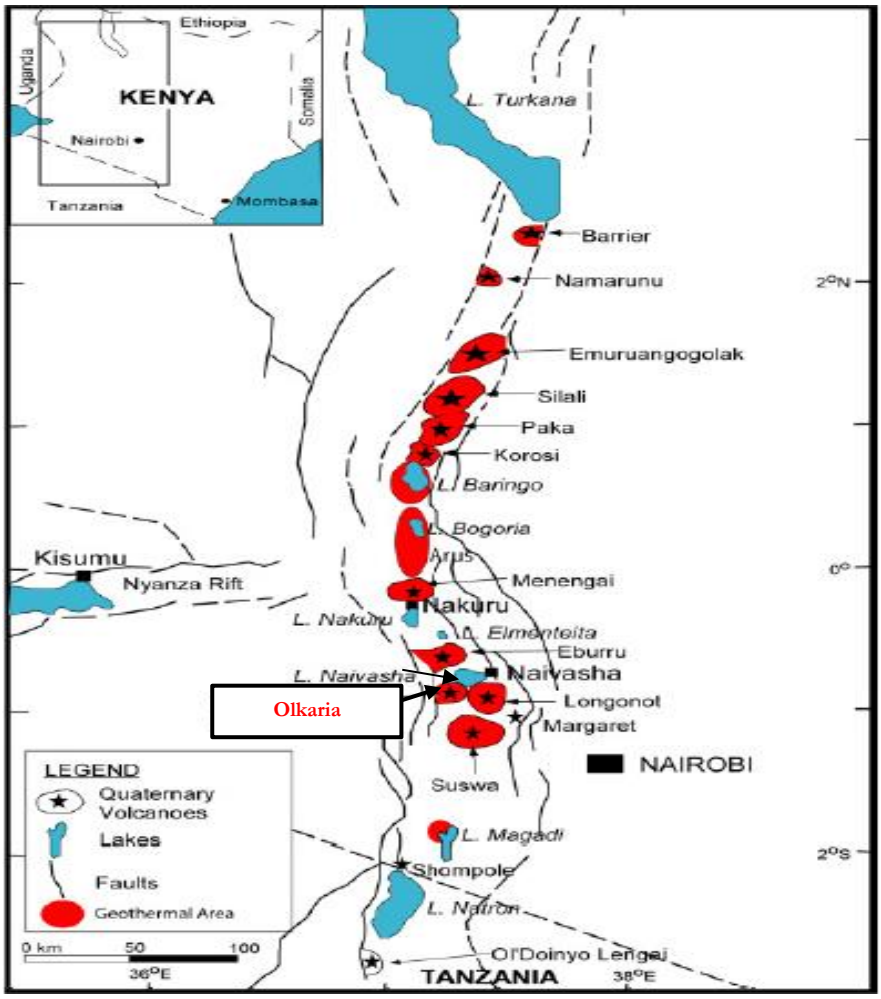

Figure 2-1: Map showing Olkaria volcanic centre together with other volcanoes along the Kenyan Rift (Omenda, 2005)

2.2. Geology and geological setting of Olkaria geothermal system

2.2.1. Geological setting

Kenyan rift is formed as a result of continental rifting between the Nubian and the Somalian plate causing crustal extension and volcanism between the two plates (Bonini et al., 2005). Volcanism in the Kenyan rift extends from Turkana in the north to the south of Lake Magadi near Tanzania. Associated with this volcanism are thirteen high-temperature geothermal systems three of which are being utilised for electricity generation. The rift floor which formed during the early Pleistocene is dominated by erupted lava flows of basaltic and trachytic composition intercalated with tuffs (Omenda, 2005). Thereafter, large shield volcanoes of silicic composition were formed in the axis of the rift during Quaternary times.

Olkaria geothermal system is inside a major volcanic complex that has been cut by a N-S trending normal rifting faults inside the Kenyan rift (Axelsson et al., 2013). Activities associated with it entails at least 80 smaller volcanic centres consisting of comendite or peralkaline rhyolites (Clarke &Woodhall; 1990). Most of these volcanic centres are structurally controlled and occur as either steep-sided domes form of lava and/or pyroclastic rock or as thick lava flows. Individual domes range from being small topographic features to prominent features such as Olkaria Hills which is 340 m high with a basal diameter of approximately 2 km (Clarke et al.; 1990). The rocks within Olkaria geothermal systems are associated with Quaternary Volcanism (Omenda, 1998) and consist of mildly peralkaline silicic volcanic domes, lava flows and air fallen pumice and peripheral basalts (Lagat et al., 2005).

2.2.2. Sub-surface Geology

Detailed study of drill cuttings and cores obtained from the geothermal wells has resulted in the documentation of the sub-surface geology of the Olkaria geothermal complex over time. Studies by Muchemi (1987), described sub-surface geology of Olkaria as consisting thick volcanic pile of predominantly alkaline, silicic rocks and pyroclastic materials with minor basaltic intercalations. A study by Omenda (1998), showed sub-surface geology as consisting of six litho-stratigraphic units(Figure 2-2). Continuous drilling of deep geothermal wells up to (3000 m) have contributed to an improved understanding of the downhole stratigraphy with six distinct groups described by previous studies being present in all confirmed. According to Lagat et al. (2005), the litho-stratigraphic sequence derived from wells drilled across all Olkaria fields are typically similar. The following lithostratigraphic sequence exists in Olkaria geothermal systems starting from the youngest to the oldest (Omenda, 1998).

- **Upper Olkaria volcanic**: They consists of comendite, rhyolites, trachyte and minor basalts together with pyroclastic materials (Clarke et al.; 1990). Previous studies show their occurrence from the surface to a depth of about 500 m below the surface with comendite being the dominant rock in this formation (Lagat et al., 2005).

- **Olkaria basalt**: The formation consists of basaltic flows separated by thin layers of tuffs, minor trachytes and rhyolites. It underlies the Upper Olkaria volcanic and varies in thickness from 100-500 m.

- **Plateau trachyte**: This precede the Olkaria basalt and is mainly characterized by trachyte with minor intercalation of tuffs, rhyolites and basalts. Based on the boreholes drilled, the trachytic flows penetrated by the wells occurs in two petrographic variety where one is strongly feldspars-phyric and dense and the other one is fine-grained, aphyric with abundant feldspars.

- **Mau tuffs**: They are the oldest units of rocks cropping out and encountered during drilling process in the Olkaria geothermal system. The unit correlates with Mau ranges tuff on the western escarpment of the Kenyan rift. They are mainly composed of tuffs with minor interbeds of rhyolites, basalts and trachyte.

- **Pre-Mau volcanic**: According to Lagat et al. (2005), this rock unit is not exposed in the study area but outcrops on the rift scarps in the part of the southern Kenyan rift. It is composed of trachyte, basalts, phonolites and tuffs of unknown thickness overlying the basement rock.

- **Basement system**: This comprises of Proterozoic metamorphic amphibolite grade gneisses and schists, accompanied by marble and quartzites of the Pan-African system (Shackleton, 1996). Olkaria intrusive is inferred from gravity and seismic studies which indicates a large dense body below Olkaria volcanic complex at a depth of about 6km (Omenda, 1998).

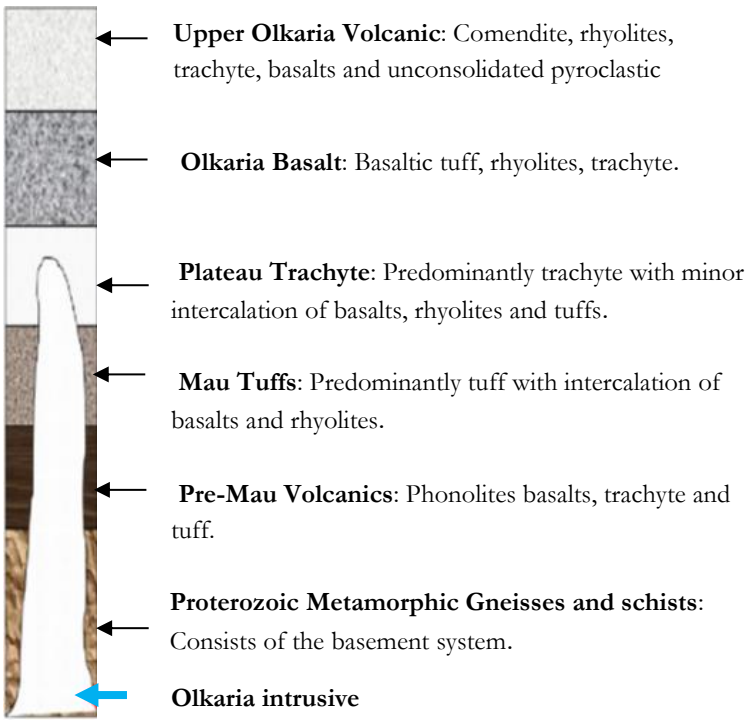

Figure 2-2: Sub-surface geology of Olkaria geothermal system (modified from Musonye, 2015)

2.2.3. Structural geology of the Greater Olkaria Volcanic Complex(GOVC)

Development of the geothermal system is largely influenced by regional structures and tectonics. Typically, structures such as faults and fractures facilitate geothermal fluid flows by providing channels for fluid pathways. In Olkaria, the main structures controlling fluid flows include faults, fractures, Ol Njorowa gorge, the rings structures and dyke swarms (Omenda, 1998). Previous studies showed N-S trending fault e.g. Ololbutot fault, NW-SE,NNW-SSE e.g. Gorge farm fault and ENE-WSW e.g. Olkaria fault as the main faults characterizing Olkaria structural patterns(Figure 2-3). According to Lagat et al. (2005), faults are more prominent in the Olkaria East, Olkaria North-east, Olkaria Central, Olkaria West but are scarce in the Olkaria domes. The oldest are thought to be NW-SE and WNW-ESE striking faults which are associated with rift development. An example is Gorge Farm fault bound by the geothermal field in the north-eastern part up to the domes field (Lagat et al., 2005). The latest tectonic activities are represented by younger N-S and NNE-SSW faults and fractures such Ololbutot fault. Dike swarms are mainly exposed in the Ol Njorowa gorge trending in a NNE direction confirming to the trend of the main fault lines. More importantly, subsurface faults have been encountered in most wells drilled in Olkaria. This was attested by drilling problems(e.g. cave-ins and loss of drilling fluid) encountered when these faults were dissected during drilling process.

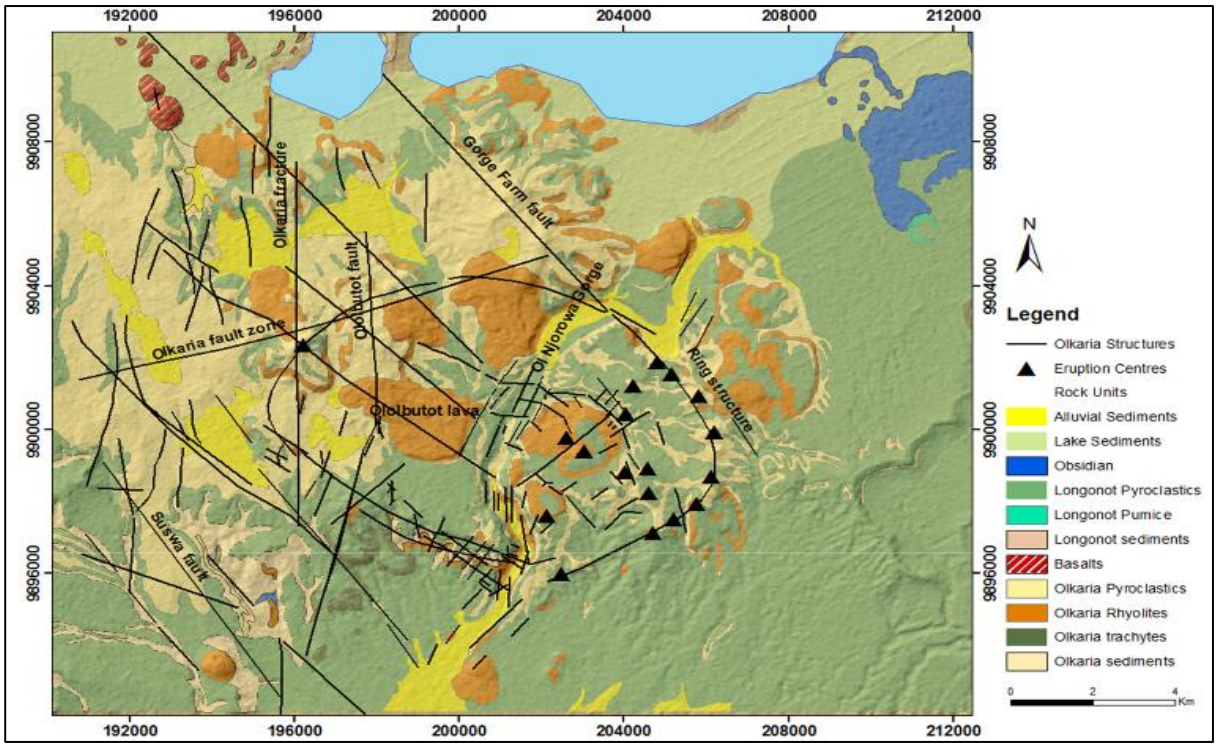

.

Figure 2-3: Structural map of Olkaria on a detailed geological map (Munyiri, 2016)

2.3. Hydrothermal alteration minerals in a geothermal system

Hydrothermal alteration minerals are formed as a result of the interaction between hydrothermal fluids and the host rock as the system strives to achieve a state of equilibrium (Browne, 1978). They reflect the mineralogical, textural and chemical response of rocks to a changing thermal and chemical environment in the presence of hot water, steam or gas (Henley & Ellis, 1983). In geothermal system, hydrothermal alteration provides information on the reservoir and fluid characteristics, and the evolution of the geothermal system (Browne & Ellis, 1970). In conjunction with other data from other scientific disciplines, it is then used to evaluate the potential of a geothermal resource.

Formation of hydrothermal minerals is dependent on a combination of several factors which includes temperature, pressure, rock type, permeability, fluid composition and the duration of time taken during mineral formation (Browne, 1978). Subsequently, this results in the formation of different alteration minerals and assemblage from one zone to another depending on the prevailing conditions. Principally, these factors are independent though the effect on one or more of the factors can influence in the location and the extent of the hydrothermal alteration mineral formed (Lagat et al., 2005). For instance, Bird et al. (1983) indicated the formation of epidotes and prehnite at a temperature above 230 ^{0}C and often in excess of 300 ^{0}C in an active geothermal field. Equally, clinopyroxenes and amphiboles which are also high-temperature minerals are usually formed at a temperature above 300 ^{0}C. As pointed out by Browne (1978), other minerals which are temperature dependent includes illite which forms above 230 ^{0}C and zeolites where mordenite forms near 50 ^{0}C and wairakite usually above 215 ^{0}C.

On the other hand, mineralogy of parental rocks has little effect on hydrothermal alteration minerals formed other than influencing rock permeability (Browne, 1978). However, at a lower temperature, the nature of parent rocks influences some of the alteration product formed. For example, high silica rocks common in rhyolitic units forms silica-rich zeolites e.g. mordenite while silica-poor rocks form silica poor zeolites such as chabazite and thomsonite (Mortensen, 2012). Equally, illite is dominant clay minerals at a higher temperature in andesite regions whereas chlorite predominates in basaltic regions. Nontronite an iron-rich

smectite group is usually formed as an alteration product of the hydrothermal process on basalt and ultramafic rocks (Haldar & Tišljar, 2014). Fluid composition influences the formation of alteration minerals due to the fluid chemistry, pH (e.g. neutral and acid) and partial pressure of gases in solution with the fluids (Browne, 1978). Study by Reyes (1990) describes neutral pH alteration as formed by hot water near neutral pH while acid alteration as being formed by the passage of low-pH high sulphur bearing fluids. Formation of pyrrhotite instead of pyrite and which is common minerals in an active geothermal field is related to partial pressure of H_2S, H_2 and temperature (Browne, 1970).

Permeability controls the amount of alteration at a particular depth by controlling the volume of water passing through the rocks (Lagat et al., 2005). Consequently, types of hydrothermal minerals can be used as an indicator of high-permeability as well as poor permeability systems. Reyes, (1990) indicated minerals such as quartz, anhydrite, wairakite, illite, adularia, hyalophane, abundant pyrite and calcite as an indicator of high permeability while prehnite, pumpellyite, pyrrhotite and abundant laumontite as indicators of poor permeability. Moreover, hydrothermal minerals formed as a result of the permeability effect can also be used as indicators of cold water influx (Reyes, 1990). Possible zones of influx are indicated by abundant goethite/hematite in veins, abundance of magnesium-rich minerals such as vermiculite, dolomite, ankerite, calcite and magnesium-rich chlorite.

In Olkaria, hydrothermal minerals appear both as replacement of the primary minerals as well as in vesicles, vugs and fractures (Lagat et al., 2005). Identification and mapping of hydrothermal mineral distribution and abundance is mainly obtained from petrographic studies of drill cuttings samples. Study by Omenda (1998), showed their formation as mainly being influenced by temperature, permeability and rock type. Main hydrothermal minerals found in Olkaria geothermal systems as described by Mortensen (2012), includes albite, amphibole(actinolite), biotite, calcite, chlorite, chalcedony, epidote, adularia, illite, pyrite, mordenite, quartz, sphene, garnet, hematite and opal.

2.4. Fundamental concept of SWIR Spectroscopy

Spectroscopy is the study of light as a function of the wavelength emitted, reflected or scattered after light interacts with solid, liquid or gas (Clark, 1999). Reflectance property of an object depends on its physical and chemical properties, surface roughness and the incidence angle of the incoming radiation. After interaction with the material, the light undergoes either electronic, vibrational or rotational transition which results in the formation of absorption bands in the spectra of the materials (Hunt, 1977). Absorption features in the SWIR region are a function of the chemical composition. The absorption bands are observed as a consequence of molecular vibrations of bonds in a crystal lattice within 1000-2500nm wavelength range (Clark, 1999). The energy of absorption corresponds to distinct energy levels and occur in well-defined wavelength positions (Hauff, 2008).

In geothermal systems, commonly formed hydrothermal minerals have mineral groups such as OH, H_2O, CO_3, NH_4 Al-OH, Fe-OH and Mg-OH (Bignall & Mark, 2015). They include mineral groups such as phyllosilicates(illite, muscovite, chlorite), sorosilicate(epidotes), inosilicates(actinolite), carbonates(calcites, ankerite, siderite) and sulphates(alunite, jarosite, gypsum). These mineral groups have defined absorption features due to their compositional differences. For example, 1400 nm(OH), 1900 nm(H_2O), 2200 nm(Al-OH), 2330 nm(CO_3, Mg-OH). Resultant spectra from SWIR spectrometer measurement consist of diagnostic absorption features superimposed on a broad background continuum with individual absorption due to molecular vibrations being represented as minima below the baseline of the spectra. To accurately identify them, background signal(continuum) is removed in order to enhance absorption features by a process called continuum removal or hull correction(Figure 2-4). Below is a summary of parameters that define and describes hydrothermal alteration minerals mapped in a geothermal system and active in the SWIR region of an electromagnetic spectrum.

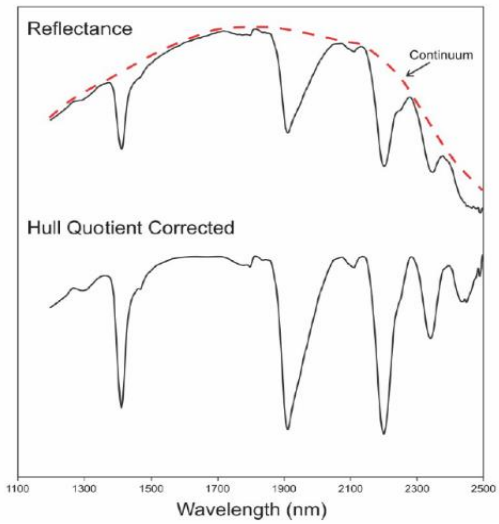

Figure 2-4: A reflectance spectra showing a normal continuum and a continuum removed(hull corrected) spectra (Simpson & Christie, 2016)

2.4.1. Aluminum phyllosilicates group

They are also referred to as clay or sheet silicate minerals and includes montmorillonite, nontronite, illite-smectite, illite and muscovite. They have shared absorption features at 1400 nm, 1900 nm and 2200 nm (Clark et al., 1990). To distinguish them, additional spectral characteristics in other bands within the spectrum are used. For example, Hunt (1986) suggested the use of 2350 nm and 2450 nm absorption features to distinguish illite and muscovite from montmorillonite. Clark et al. (1990) indicated the use of poorly developed or absent 2450 nm features in illite to differentiate it from muscovite. Recently, Pontual et al. (2008) suggested use of relative depth of both Al-OH and H_2O as spectral parameters for distinguishing aluminium phyllosilicates minerals. In this case, illite is distinguished by having a deeper Al-OH feature than H_2O feature and on the contrary, montmorillonite is distinguished by having a much deeper H_2O feature compared to Al-OH(Figure 2-5). Lastly, mixed layer illite-montmorillonite is differentiated from other groups of phyllosilicates minerals by having spectra with profile intermediate that of illite and montmorillonite.

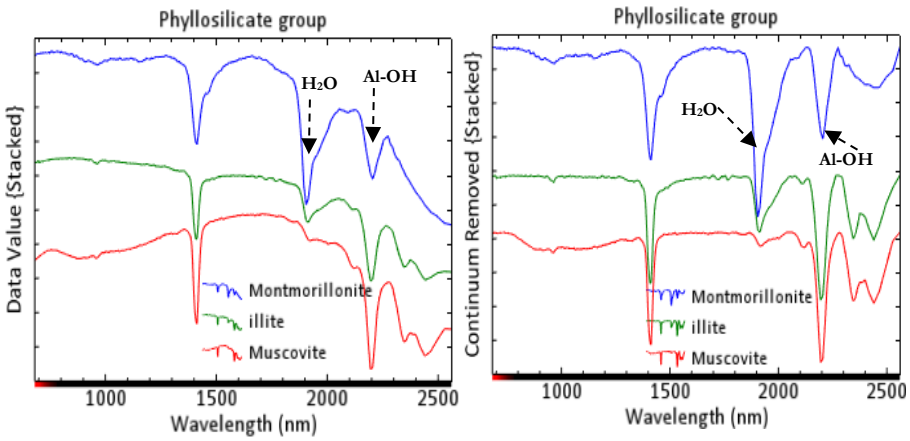

Figure 2-5: Normal and continuum removed spectra of Muscovite, Illite and Montmorillonite from USGS spectra library (Kokaly, 2018) showing characteristic spectral of illite, muscovite and montmorillonite.

2.4.2. Fe-Mg phyllosilicates group

Chlorite is most common hydrothermal mineral belonging to the Fe-Mg phyllosilicate group of minerals (Caritat et al., 1993). It is formed as retrograde minerals in igneous and metamorphic rocks that have been weathered. Typically, in a hydrothermal environment, it forms through replacement of ferromagnesian minerals and volcanic glass or via precipitation in open cavities e.g. veins, vugs (Rae et al.; 2011). Spectrally, chlorite is identified using Fe-OH and Mg-OH features which mainly depends on the ratio of Fe/(Fe+Mg)(Yang et al.; 2000). Pontual et al. (1997 study showed the occurrence of two diagnostic feature between 2235-2259 nm and 2320-2360 nm associated with Fe-OH and Mg-OH features respectively. Wavelength position of these two features varies with composition with shorter wavelength indicating magnesium rich chlorites and longer wavelength iron-rich chlorites.

2.4.3. Sorosilicate group

Epidote is the most common mineral in this group consisting of Ca-Al-Fe^{3+}. It is formed as a function of the physical and chemical processes that characterize magma-hydrothermal systems (Spider, 2004). Studies by Abweny et al. (2016) indicates their formation as a result of hydrothermal and metamorphic processes of the prevailing geothermal environment. Composition difference in respect to Fe^{3+}-Al ratio depends on the bulk rock composition and the pressure-temperature-fluid-redox conditions which consequently results in different minerals of the epidote group in veins and cavities (Spider, 2004). Spectral identification is by use of Fe-OH characteristic feature at 2256 nm and Mg-OH feature between 2335-2342 nm wavelength range(Pontual et al., 1997) It also has a diagnostic OH feature near 1540 nm and 1835 nm which discriminate it from chlorite.

2.4.4. Inosilicates group

The most common mineral in this group includes amphiboles(actinolite, riebeckite, hornblende tremolite) and pyroxene. In a geothermal system, the most commonly formed minerals in this group are actinolite and hornblende. Actinolite is an intermediate variety between magnesium-rich and iron-rich ferro-actinolite (Abweny et al., 2016). Equally, hornblende is a calcium-rich end member of the amphibole group while riebeckite is a sodium solid series of amphibole minerals (Bird, 2000). Spectral identification is by use of main Mg-OH diagnostic feature which varies from 2314-2324 nm, 2324-2350 nm and 2330-2350 nm for actinolite, hornblende and riebeckite respectively.

2.4.5. Carbonates

Study by Stefan (1989) indicated calcite as the most common carbonate mineral formed in a geothermal system. In hydrothermal system, it is widely distributed and is common in a wide range of temperature (Calvin & Pace, 2016). Other carbonate mineral present in active geothermal systems besides calcite includes ankerite, siderite and rhodochrosite. Spectrally, carbonates are identified by their main diagnostic absorption features occurring between 2340-2345 nm for calcite, 2330-2340 for ankerite and 2320-2350 for siderite (Pontual et al., 2008). However, identification of carbonate absorption features can also be problematic due to overlap with the main chlorite Mg-OH feature.

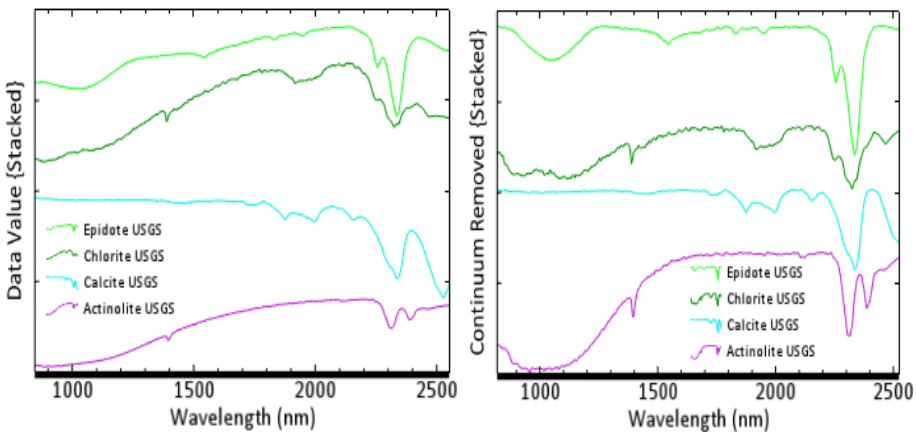

Figure 2-6: Normal and continuum removed spectra of epidote, chlorite, calcite and actinolite from USGS spectral library (Kokaly, 2018).

2.4.6. Zeolites

Zeolites are hydrous aluminosilicates minerals with cations of potassium, sodium, calcium and magnesium. They are the main components of altered volcaniclastic rocks ranging in age and composition (Christidis, 2012). They are formed by alteration of volcanic glass in various geological environments under variable geochemical and temperature conditions. According to Browne (1978), the most common zeolites minerals formed in geothermal systems are mordenite and wairakite. Spectrally, zeolite is identified by intense water absorption feature near 1400 nm and 1900 nm (Yang et al., 2000). It is distinguished from montmorillonite by lack of absorption feature near 2200 nm. Nonetheless, Yang et al. (2001) pointed out difficulties in distinguishing different zeolites species(e.g. mordenite and wairakite) spectrally due to the similarity in their major spectral absorption features. Figure 2-7 shows spectral features of mordenite form USGS library.

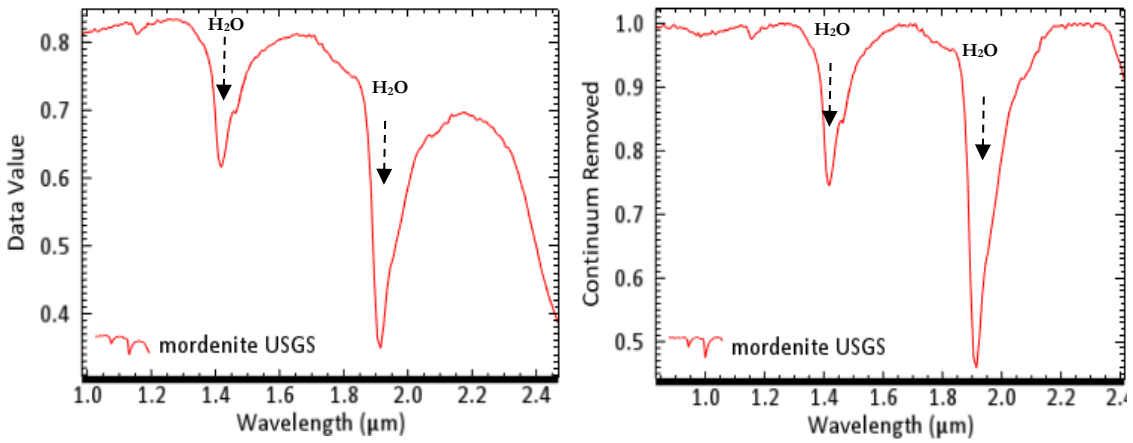

Figure 2-7: Normal and continuum removed spectra of mordenite from USGS spectral library (Kokaly, 2018).

2.4.7. Opal

It is a hydrated amorphous form of silica and is the main component of siliceous sinters in many terrestrial hydrothermal systems (Goryniuk et al.; 2004). It is identified by the presence of shallow and broad absorption features at 2200 nm(Figure 2-8) in SWIR wavelength range (Littlefield & Calvin, 2014).

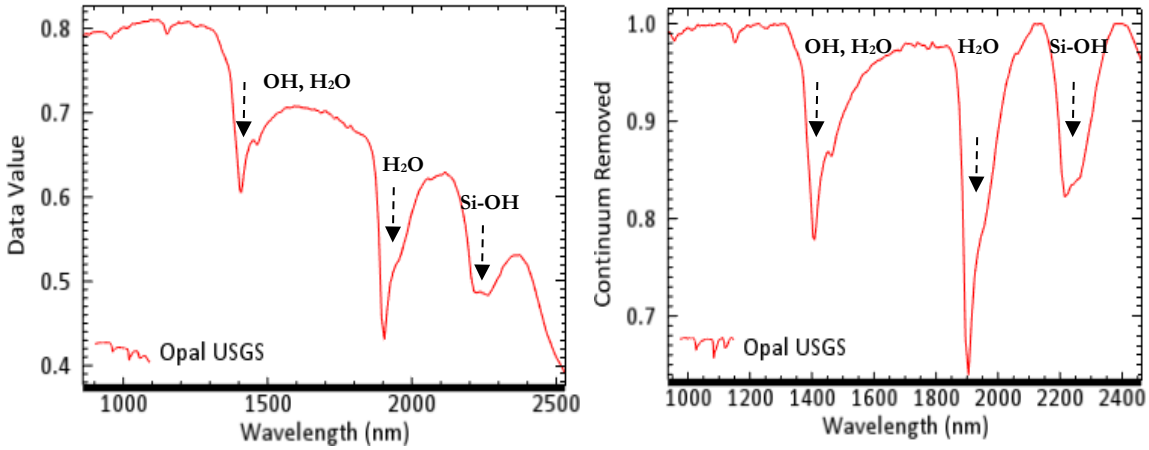

Figure 2-8: Normal and continuum removed spectra for Opal from USGS spectral library (Kokaly, 2018)

3. DATASET AND METHODOLOGY

The chapter describes the datasets and methodological techniques used in this research. It describes data collection strategy and analytical techniques used to answer research questions for the proposed objectives.

3.1. Materials and dataset

Materials and dataset used for this study were collected on a three weeks field visit to Kengen, Olkaria geothermal project. It involved the following steps:

3.1.1. Defining geothermal wells to study.

Based on the existing data, previous studies and the expertise knowledge from well siting committee, three wells were selected. Well OW-205, located in Olkaria central sub-field was selected to represent cold in-flux zone while well OW-916 and well OW-917 both of which are located at Olkaria domes were selected to represent up-flow and out-flow zone respectively(Figure 3-1).

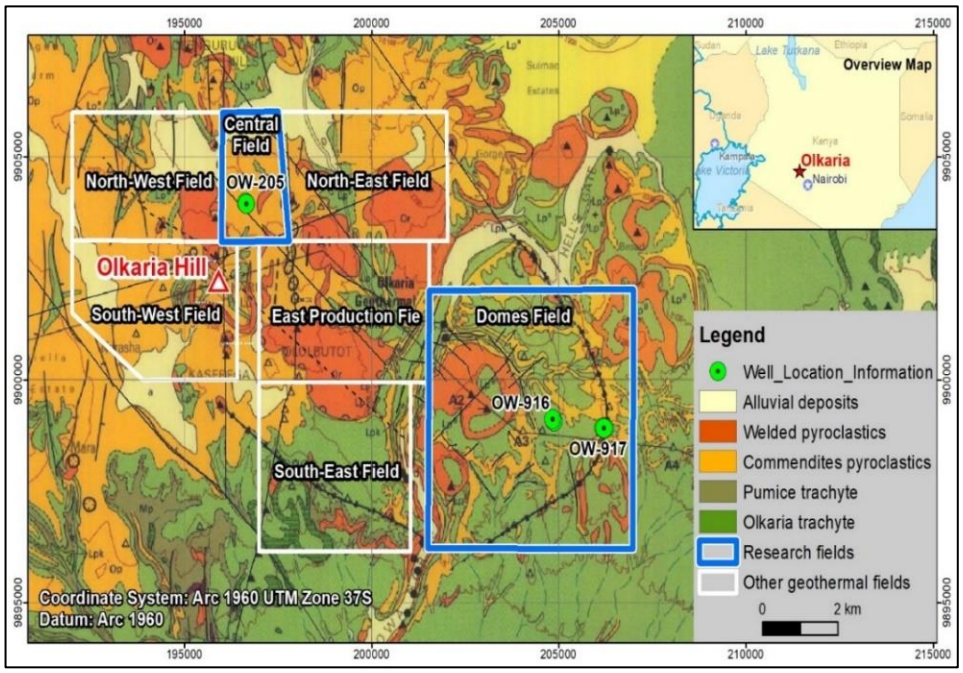

Figure 3-1: Location of OW-205, OW-916 and OW-917 boreholes.

3.1.2. Sample selection at the Coreshed.

The first step involved desktop study where for each borehole, depth to study was determined. This involved, use of previously collected lithological data mainly rock types (trachyte, rhyolite, tuffs, basalt) at the rig site. Usually, these lithological data are collected using a binocular microscope during the drilling process. In addition, sample selection was such that both weakly and highly altered samples in a certain rock type were equally represented. Lastly, samples selected were physically picked from sample shelves at the geology section coreshed. Approximately 10 grams of each sample was packed in polythene bags, labeled and sealed. A total of 135 samples were collected: 41 samples for OW-916, 52 for OW-917 and 42 for OW-205. Grain size varied from fine-grained, medium grained and coarse-grained depending on the size of the drill chip(Figure 3-2).

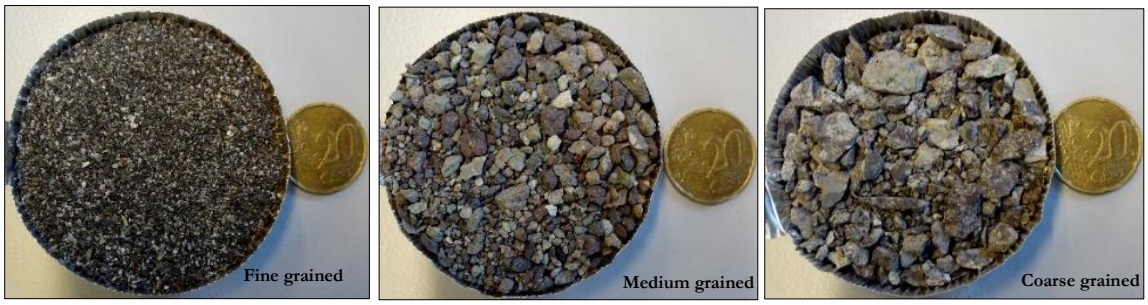

Figure 3-2: Images of various grain sizes of drill cuttings from OW-917.

3.1.1. Auxiliary data collection

This involved collection of measured temperature data from reservoir section, lithological data and XRD data from geology section, shapefiles required for this research from GIS section and additional literature necessary for this research from Olkaria library.

3.2. Laboratory Imaging Spectroscopy

3.2.1. Instrument.

Imaging was done using SWIR camera (Specim ltd; Finland) located in the Geo-Science Laboratory in the University of Twente, ITC Enschede, Netherlands. Table 3-1 below shows technical specifications of SWIR camera used for this study.

Table 3-1: Technical Specifications of SWIR camera.

Type of the stage	Lab stage
Spectral range (nm)	1000-2500
Distance of the sensor to sample (cm)	30
Pixel size(μm)	260
Image swath(mm)	98
Number of bands	288
Lens focal length(mm)	OLES30 (30 mm)
Spectral Sampling	5.6 nm
Spectral resolution FWHM	12nm

3.2.2. Hyperspectral Image acquisition.

Samples were first placed on aluminum container of an approximate height of 40 mm and a diameter of 60 mm ensuring a flat surface and then placed on a box containing silver sand. Images of samples were made by passing box containing samples(Figure 3-3)on a translation stage which was then passed underneath the camera. Image cubes were constructed using the camera in a push-broom style where x-axis was the across track direction and the z-axis as the spectral direction. A white reference standard plate considered as a perfect reflecting surface (99%) of the incident light and a dark reference surface measurement were taken before the measurements were done and were used later for image calibration. Imaging was done per well where samples from each well were arranged in batches of 7 samples each. A total of 21 scans were made from the three wells with each scan having 7 samples each. However, one scan in each OW-916 and OW-917 had 6 and 3 samples respectively. After all the measurement were done, Specim data was retrieved from the ITC server and then converted to reflectance using the white reference and the dark current measurement using ITC standard processing procedure.

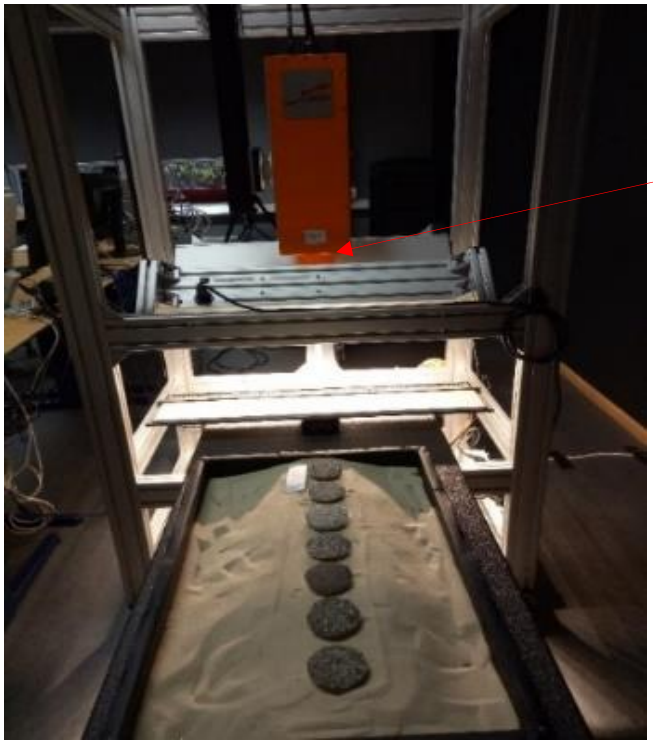

Figure 3-3: Image acquisition using lab stage SWIR camera.

3.2.3. Image pre-processing

The main objective of image pre-processing was to prepare data for further processing techniques by removing or minimizing the influence of unnecessary artifacts such as bad/dead pixels or unwanted part of the image not covered by the sample that might affect spectral measurements. For this study, the following pre-processing techniques were applied:

- Conversion of raw DN values into reflectance image using a dark and white reference image by loading Specim 'manifest.xml' file in dark and white reference tool in HypP3 software (Bakker, 2014).

- Correction of bad columns in the data from the SWIR camera by replacing them with the data from the neighboring cells using Fix SWIR 8th pixel problem algorithm in HypP3 software.

- Spatial subset using an ellipse selection tool in ENVI. This was used to mask out areas of the samples approximately 5 mm from the edges of the aluminum containers to minimize reflection effects that could be emanating from the containers.

- Spectral subset of unwanted bands in this case band 1-16 (894.51nm-980.15nm) and band 288 (2511.101nm) which had bad images. This was done to improve the overall quality of the spectra.

- De-striping filter in HypPy3 was used to remove artifacts associated with dead or bad pixels. This was done using two steps. First step involved running de-stripping using large threshold values of 10 leaving the apply offsets and replace bad pixels box unchecked. Using the offset image, threshold values were determined using **x** and **y** profiles of offset image displayed in ENVI. Second step involved running de-stripping again using mean difference of 1.0 and standard deviation of 0.05 determined from the first step as the threshold values and checking the apply offset and replace bad pixels boxes.

- During image inspection, some pixels had negative reflectance and very low reflectance value. To correct this, a Fix No data tool in HypPy3 was used to convert pixels with reflectance value below 0.05 to not a number(NaN) in all bands having this problem.

- Spatial-Spectral smoothing was done using a mean 7(1+5+1; central pixel and 4 direct neighbors in space and 2 direct neighbors in spectral domain) filter in HypPy3 software. This was done to smoothen the spectra by removing noise for the purpose of spectral identification and SAM classification technique.

3.3. Image processing

3.3.1. Spectral identification

For this research spectral identification was done following a structured approach as stipulated by Pontual et al., 2008). The following guidelines were put into consideration;

- That most SWIR active minerals have a characteristic spectrum between 1300-2500nm.

- That by identifying the absorption feature and noting its wavelength position, mineral can be classified into spectral groups.

- That identification should take into account the shapes and wavelengths of other absorption features in the spectrum.

- That in addition to displaying absorptions features, reflectance spectra can be influenced by other absorption features which are out of range e.g. ferrous iron absorption which affects the overall background shape of the spectrum by causing a sharp drop towards the 1000nm region.

- In case of mineral mixing, addition absorption features, additional shoulder or inflections on the dominant minerals, increase in depth of absorptions features relative to normal depth, features broadening, and wavelength shifts of the absorption features should be used for mineral identification

Spectral identified minerals using the method above were then checked and compared against USGS spectral library using in ENVI and The Spectral Geologist(TSG) software. Characteristics diagnostic features such as OH, H_2O, Al-OH, Fe-OH, Mg-OH, CO_3 identified from most of the mineral spectra analyzed occurred at the same wavelength or approximately the same with those from USGS library.

3.3.2. Wavelength Mapping

Wavelength mapping is a semi-automatic approach estimating the wavelength position and the depths of the absorption features of minerals in a wavelength map (Ruitenbeek et al., 2014). The method is based on the calculation of the wavelength position and depth of the absorption features in an image spectrum within a specific wavelength range. To process the image, the user is required to set wavelength range of interest for which the convex hull is calculated and removed to obtain a continuum removed spectra. The resulting product is an image product in RGB transformation where the hue represents the wavelength position and intensity the depth of the absorption feature (van der Meer et al., 2018). The resulting image maps can give an assessment of dominant groups of minerals and their spatial distribution (Ruitenbeek et al., 2014).

The main aim of creating wavelength maps in this study was to help in the selection of endmembers for mineral quantification. In addition, it was also used for a general overview of spatial change of hydrothermal minerals alteration relative to borehole depth. The first step involved wavelength stretch between 1350-2400 nm with an aim of distinguishing minerals with the deepest absorption features across the whole SWIR

range. This was followed by wavelength stretch narrowed between 1850-1950 nm with an aim of distinguishing zeolites and smectite from other minerals by using the deepest water absorption feature near 1900 nm. The third step involved a stretch between 2160-2228 nm wavelength stretch to establish the compositional difference between various Al-OH minerals. It was followed by a stretch between 2300-2370 nm wavelength range aimed at distinguishing minerals such as chlorites, epidotes, actinolite and calcite having diagnostic absorption feature within this region. Lastly, a stretch of 2100-2400 nm wavelength range targeting all the main SWIR minerals commonly found in a geothermal system. The aim of this stretch was to have a general overview of the available hydrothermal minerals and how they change relative to depth.

3.3.3. Endmember selection

From the wavelength maps, hydrothermal alteration minerals active in the SWIR region were represented by different colour and brightness intensity with brightest pixels representing minerals with the deepest absorption features. Endmember library was created by collecting mean spectra form the stretched image using ENVI Region of Interest (ROI) tool. The size of ROI created was approximately the size of the grain with the same hue and intensity and varied within a sample and also from one depth to another. Thereafter, the mean spectra collected was analyzed and identified using visual interpretation as proposed in *section 3.3.1* above and comparison with USGS spectral library. For minerals occurring as a mixture, e.g. illite-chlorite, epidote-chlorite and calcite-chlorite, representative spectral were selected to be part of the endmember library. A total of 14 endmembers were selected from all the three boreholes.

3.3.4. Spectral Angle Mapper(SAM)

This is a hard classification method based on the calculation of the angular similarity between image spectra and the reference spectra in feature space. It allows rapid mapping of mineral spectra by determining the spectral similarity between two spectra by calculating the angle between them(Figure 3-4)and treating them as vectors in a space with dimensionality equal to the number of bands (Kruse et al., 1993). The reference spectra can either be a laboratory, field spectra or an image extracted spectra reduced to apparent reflectance. The smaller the angle between the test spectrum and the reference spectrum, the closer the match. Pixel with the closet match are assigned to the class that exhibits the smallest spectral angle (Rashmi et al., 2014). Nevertheless, SAM success highly depends on the wavelength range and the threshold angles selected (Shahriari et al; 2014).

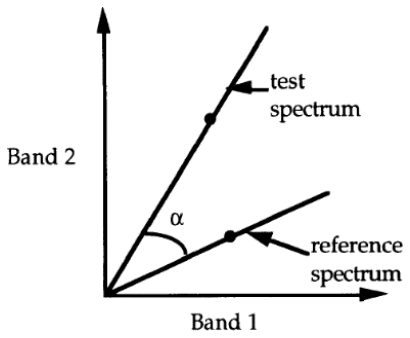

Figure 3-4: Illustration of SAM concept in two dimensions.

For this study, spectra derived from images were used as reference spectra. To classify the images, first a spectral subset of between 2100-2450 nm was done on all images and the resultant image was then used as input file in SAM classification algorithm in ENVI. A fixed threshold angle of 0.10 radians was maintained for all classifications. However, for the purpose of illite crystallinity and composition variation determination for illite and chlorite, a tighter threshold of 0.05 radians was used to classify only the purest illite pixels and chlorite pixels. To confirm how successful classification was, pixels from the classified image were chosen randomly by inspecting the spectra derived from classified image against those from the spectral libraries.

If unsuccessful, endmember selection step was repeated until the most representative endmember spectra was achieved. Finally, mineral abundances of each class were derived by overlaying classified image on the original image using ENVI in order to get pixel distribution per spectral class.

3.4. Illite crystallinity

This was determined by finding the ration of Al-OH feature to that of H_2O feature in illite classified pixels.

$$\text{Illite Crystallinity} = \frac{\text{Depth of Al-OH absorption feature}}{\text{Depth of } H_2O \text{ absorption feature}}$$

Using SAM classified images, illite pixels were masked leaving all the other mineral out of the mask. The mask was then applied on wavelength map. Using a band ratio algorithm in ENVI, the ratio of interpolated depth for Al-OH feature and that of interpolated depth of H_2O feature was used to generate crystallinity image. For further analysis, crystallinity values were first converted into ASCI files by using Band Threshold to ROI tool in ENVI. Typically, it involved generation of basic statistics(i.e. minimum, maximum, mean and standard deviation) of crystallinity in an image using Quick stat tool. Minimum and Maximum statistics values generated by the tool were then used as input in Band Threshold to ROI tool algorithm as minimum threshold values and maximum threshold values respectively. The output was highlighted pixels of the number of pixels occurring within the set threshold values. The number of pixels highlighted were then exported as ASCI using Output ROI to ASCI algorithm in ENVI for further analysis.

3.5. Composition variation of chlorite and illite hydrothermal minerals

To determine this, a mask was created on SAM classified images to exclude all the other mineral classes except illite and chlorite spectral class. For better results, each mineral was masked and processed independently. Visual inspection of spectra from the masked image was done to confirm purity of the pixels. Thereafter, ROI interest was created on illite and chlorite masked pixels and then overlayed on interpolated wavelength minimum image from previous wavelength stretch determined from *section 3.3.2*. Basic statistics using ROI on interpolated wavelength minimum image was used to generate statistical value for that particular ROI. The resultant mean values for both illite(Al-OH) and chlorite(Fe-OH) diagnostic absorption features were then considered as the minimum wavelength position for that particular sample. In a situation where several ROI were created on one sample and the variance was ±1nm, average of the mean values from ROI was used as the minimum wavelength position of the diagnostic feature. Else, it was treated independently. Final values for both Al-OH and Fe-OH were plotted against depth, lithology and temperature to observe their relationship in respect to wavelength shift variation(Figure 4-27-29).

3.6. X-ray Diffractometer (XRD) measurements

To validate spectral measurement, XRD measurements were performed using Bruker D2 Phaser diffractometer located at the Geoscience Laboratory of ITC, University of Twente. Representative rock samples from all the boreholes were selected from different depths. Sample selection was based on SWIR measurement results as follow: Sample which tested positive for illite, chlorite, calcite, epidote and hornblende were selected. Sample preparation involved milling the drill cuttings into powder using Retsech PM 200 milling machine to achieve grain size of approximately < 250 μm. A fraction of the milled sample was poured into the sample holder, filled and packed properly to avoid sample displacement during measurement which causes peak shifts.

X-ray data were obtained by operating the instrument at a voltage of 30 Kv and 10mA to generate CuKα radiation. A Lynexe silicon strip detector was used. Each scan ranged from 6-80 2Φ range using a 0.005 step size. A scan duration of minimum of 1 hour was used in order to improve peak intensity and to enable detection of minerals in trace amounts. The output was diffractograms consisting of a sequence of peaks of

varying count intensity and d-spacing as given by the Brags law($n\lambda=2d\sin\Phi$) where **λ** is wavelength of the incident beam, **d** is spacing between crystal planes and **Φ** is the angle between the crystal plane and the diffracted beam, **n** is an integer of the reflected waves from different layers. Mineral identification was done by using an automatic search and scan or manually searching by mineral name in DIFFRAC. EVA version 3.1 software against an inbuilt reference mineral database. Several best match peaks were generated by the software, but the ultimate likely mineral was selected by the user. Besides mineral identification, DIFFRAC. EVA software was used for semi-quantification of mineral percentages in the whole rock powder scans.

4. RESULTS

This chapter presents the results of all the methodological steps used to develop this research. It starts from image pre-processing, wavelength mapping, Mineral identification, endmember selection, mineral classification, illite crystallinity and composition variation of illite and chlorite.

4.1. Image pre-processing

This was done to prepare the data for processing techniques. It involved the conversion of data to reflectance, removal of 8th column stripping, spatial subset, spectral subset, de-stripping and spectral smoothening.

Figure 4-1 is an illustration of drill cuttings sample before and after pre-processing.

Figure 4-1: Sample number OW-205 (1122-1124 m) (A)before pre-processing and (B)after pre-processing.

4.1.1. Identified minerals and their diagnostic absorption features in SWIR wavelength range

This section describes different minerals and mineral groups identified from the study area after spectral interpretation with GMEX spectral analysis guides, TSG and USGS spectral library.

- **Smectite group**

Montmorillonite and nontronite are the main smectite group of minerals identified in this study occurring in the upper alteration sequence. They were identified based on the following criteria:

- **Montmorillonite**

Montmorillonite identified in the study area is characterized by an intense and sharp water feature between 1911-1917 nm and major but broad Al-OH band between 2214-2225 nm with no major feature in the longer wavelength region(Figure 4-2) . It was only identified in OW-916, appearing in the first sample analyzed (28-30 m) up to 450 m depth.

- **Nontronite**

Nontronite is a dioctahedral smectite where the Fe^{2+} mineral is the dominant species. Compositionally, it consists of more than 30% Fe_2O_3 (Pontual et al., 2008). Analogous to montmorillonite, it was identified by the presence of deep H_2O absorption between 1911-1917 nm with iron diagnostic absorption feature occurring at between 2296-2298nm(Figure 4-3). For this study, nontronite occurred both in OW-916 and OW-917. In OW-916, its appearance was on the first sample analysed (28-30m) up to 980 m depth while in OW-917, it appeared on (50-52 m) depth sample up to approximately 840 m depth.

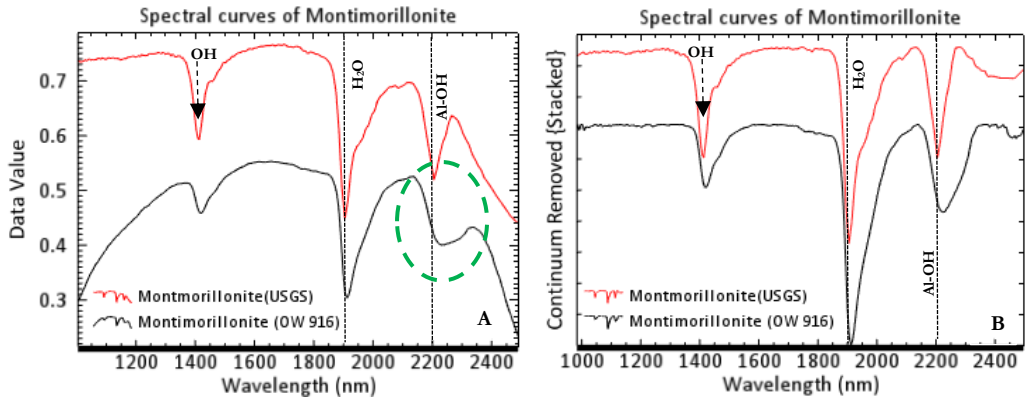

Figure 4-2: Spectral profiles (A) normal reflectance (B) continuum removed spectra of montmorillonite from OW-916 and USGS spectral library. Note the broad feature(circled) associated with montmorillonite spectra from the sample

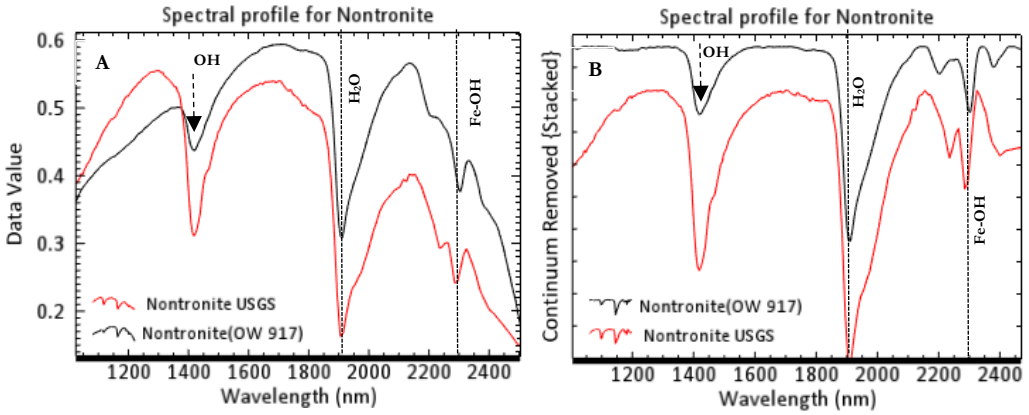

app

Figure 4-3: Spectral profiles (A) normal reflectance (B) Continuum removed spectra of Nontronite from OW-917 and USGS spectral library.

- **Zeolites**

In this study, mordenite is the most commonly identified zeolite based on spectral results from the three wells. It was identified using intense water absorption features near 1416 nm and 1911 nm. It was distinguished from smectite due to lack of characteristic feature near 2200 nm(Figure 4-4). In OW-916, it first appeared on the first sample(20-30 m) to approximately 1000m. However, it was more intense and abundant between 30-450 m with a temperature of below 100^{0}C. In OW-917, mordenite appeared between the first sample(50-52 m) up to approximately 300 m. In OW-205, it first appeared from the first sample analyzed (512-514 m) up to approximately 1000 m with a measured formation temperature of > 200^{0}C.

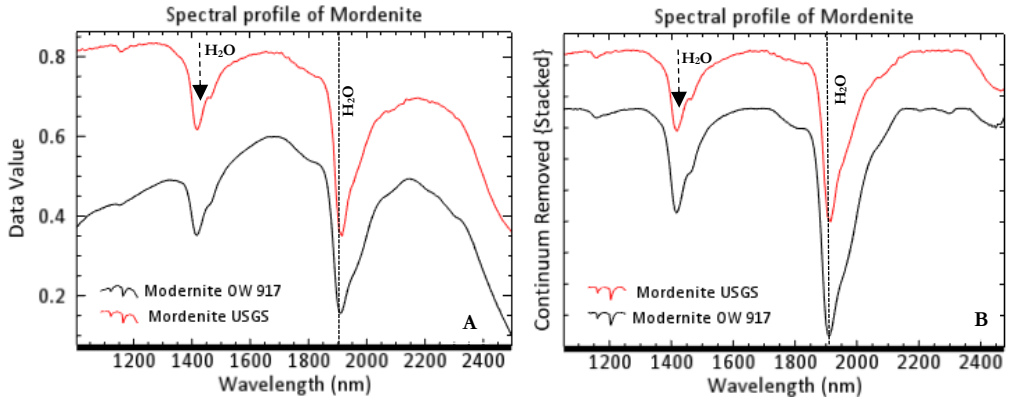

Figure 4-4: Spectral profile of (A) normal reflectance (B) continuum removed spectra of mordenite from OW-917 sample and USGS spectral library.

- **Illite**

It is a common hydrothermal mineral in the study area sometimes occurring in mixture with mixed layered illite-smectite and chlorite. Spectrally, it was identified by the use of Al-OH absorption feature between 2197-2225 nm wavelength range(Figure 4-5). It was distinguished from illite-smectite by deeper H_2O absorption feature of illite-smectite compared to that of illite(Figure 4-6). In OW-205, illite was identified in almost every sample analyzed cutting across all lithological units. Wavelength position of the absorption feature varied between 2199-2224 nm. In OW-916, illite first appeared at approximately 500 m depth then appeared sporadically up to the bottom of the hole. Spectral characteristic features varied between 2198-2224 nm wavelength range. In OW-917, it first appeared at 1800 m depth and persisted downhole. Spectral features varied between 2213-2224 nm wavelength range.

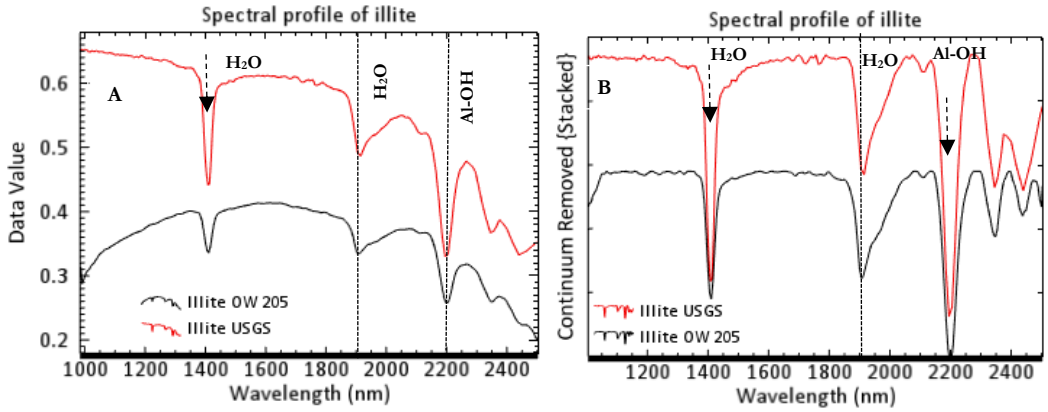

Figure 4-5: Spectral profile of (A) normal reflectance of illite(B) Continuum removed of spectra from USGS spectral library and OW-205

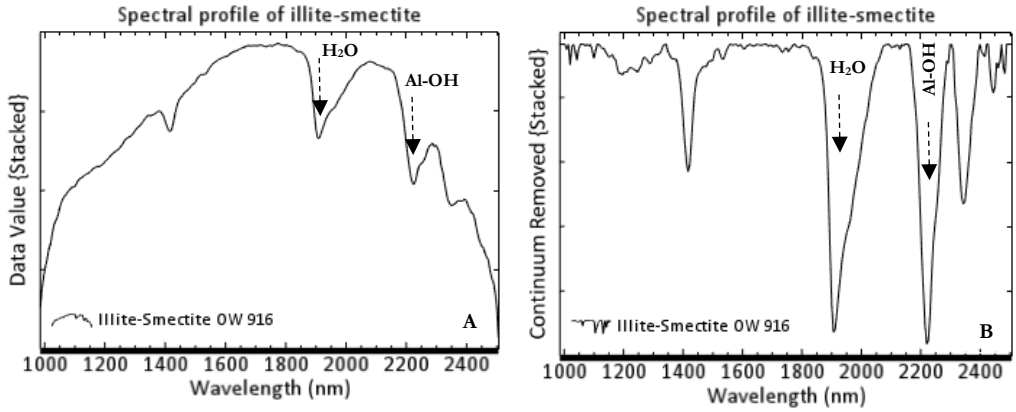

Figure 4-6: Spectral profile of (A) normal reflectance of illite-smectite(B)Continuum removed of spectra of illite from OW-916. Observed is a deeper water absorption feature equally the same depth as Al-OH feature.

- **Chlorite**

It was spectrally identified by the use of Fe-OH feature occurring between 2245-2262 nm wavelength range(Figure 4-7). It commonly occurred in mixture with illite where Fe-OH feature was largely obscured by spectrally dominant Al-OH feature. In OW-205, it was generally present at all depths starting from(512-514 m) to 3000 m depth with wavelength position of the diagnostic feature varying between (2248-2263 nm) wavelength range. Between 700-1200 m, high presence of chlorite was observed mainly on basaltic and tuffaceous material with a measured temperature of > 200^{0}C. In OW-916, chlorite first appeared at approximately 400 m depth with irregular appearance observed with increase in depth. Wavelength position of the characteristic feature occurred between 2256-2262 nm wavelength range. Finally, in OW-917, chlorite first appeared in trace amount near 500 m depth and only re-appeared again below 1500 m depth. Wavelength position of the characteristic feature varied between 2255-2363 nm.

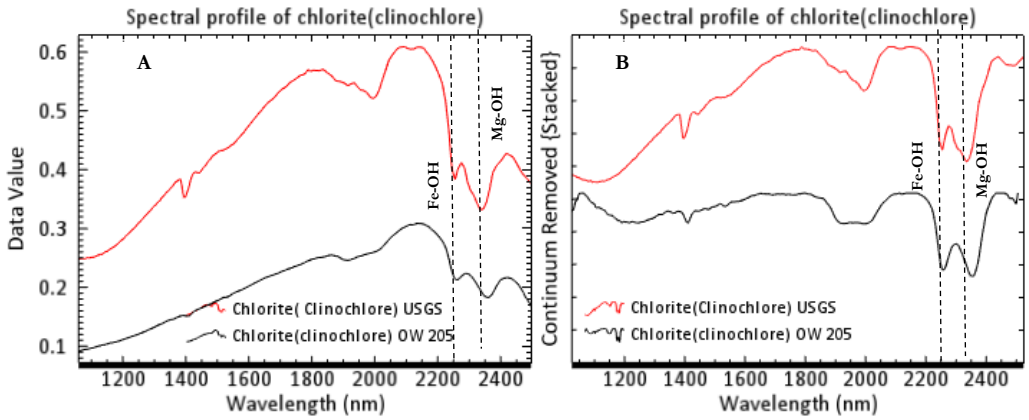

Figure 4-7: Spectral profile of (A) normal reflectance (B)Continuum removed spectra of chlorite from OW-205 and USGS spectral library.

- **Epidote**

It is a common hydrothermal mineral identified in the study area. Spectrally, it was identified by the use of absorption feature near 1540 nm, Fe-OH diagnostic feature located near 2256 n and Mg-OH feature between 2335-2342 nm wavelength range(Figure 4-8). Epidote identified in this study occurred mainly in mixture with chlorite, carbonates and amphiboles where their spectral feature overlapped above 2300 nm wavelength range. It was distinguished from other minerals by its unique feature occurring near 1540 nm wavelength range. It mainly occurred together with amphibole and trace amount of illite and chlorite. In OW-205, epidote first appeared near 1050 m and persisted downhole. It occurred together with illite, chlorite, calcite and amphiboles in almost all the depth it was recognized. In OW-916, it was first appeared spectrally at 1300 m and then appeared sporadically to the bottom of the hole. In OW-917, epidote appeared in trace amount starting from 1850 m. It occurred in association with illite, chlorite calcite and amphibole.

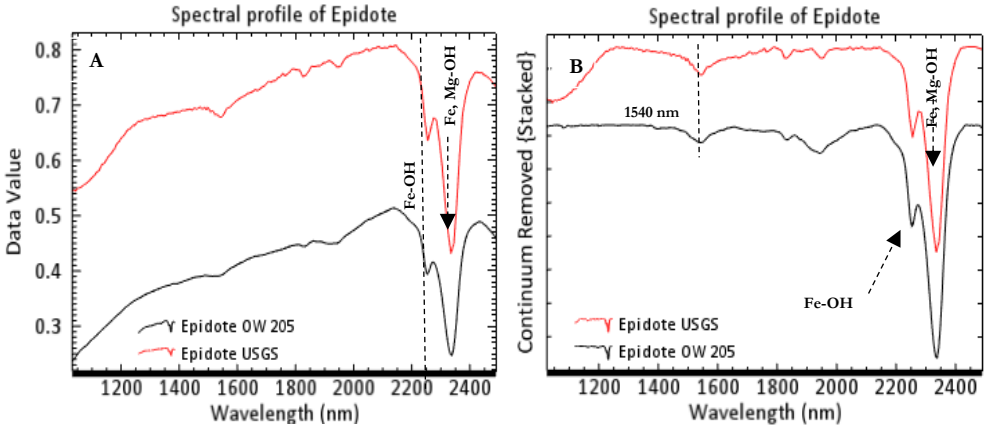

Figure 4-8: Spectral profile of (A) normal reflectance (B)Continuum removed spectra of epidote from OW-205 and USGS spectral library.

- **Amphiboles**

It is a common hydrothermal mineral identified in the study area. Spectrally, two amphibole minerals identified in the study area are actinolite and hornblende. Spectrally, they were identified by the use of Mg-OH characteristic feature which varied between 2314-2324 nm and 2326-2350 nm for actinolite and hornblende respectively(Figure 4-9). Spectral feature of amphibole overlaps with those of chlorites, epidotes and carbonates. However, it is distinguished from other minerals by use of its unique and distinct spectrum. In OW-205, the first appearance of amphibole was at 900 m depth and its presence persisted downhole. It occurred in association with illite, chlorite, calcite and epidote. In OW-916, 1300 m depth marked first appearance amphibole mainly in assemblage with illite, chlorite and epidote. It continuously appeared with

increase in depth with its abundance increasing with depth. Most conspicuous, is the appearance of amphibole at shallow depth(600 m) in OW-917. However, its presence in this well disappeared with an increase in depth.

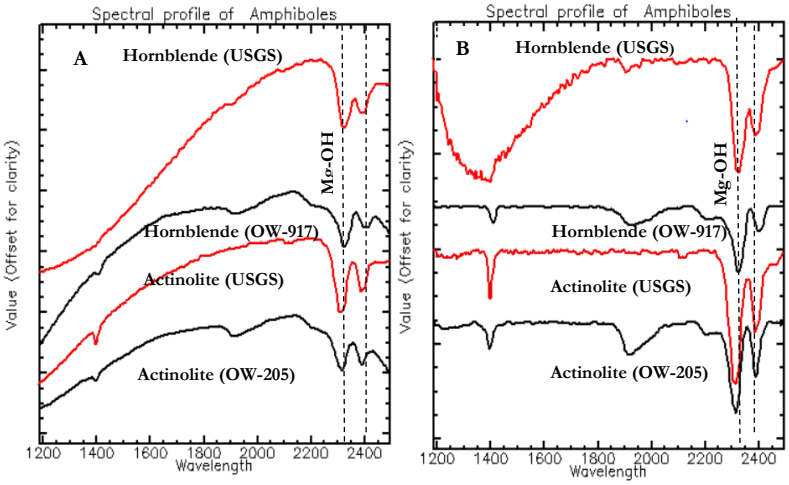

Figure 4-9: Spectral profile actinolite and hornblende minerals from USGS library and OW-205 & OW-917 (A) Normal reflectance (B) continuum removed spectra. Arrows shows shift in Mg-OH from shorter wavelength to longer wavelength from actinolite to hornblende.

- **Carbonate**

Calcite is the common identified carbonate mineral in the study area. Spectrally, it was identified by use of CO_3 characteristic feature occurring between 2340-2345 nm wavelength range(Figure 4-10). In this study, its spectral feature overlaps with those of chlorite, epidote and amphibole. Nevertheless, use of unique features in other minerals e.g. 1540 nm feature of epidote was used to distinguish them. In OW-205, calcite occur from 700 m downhole in association with chlorite, epidote and amphibole. Conversely, in OW-916, it appears in a localised zone between 500-1400 m depth where it is in association with illite, chlorite and epidote and in some cases amphibole. In OW-917, it occurred from 500 m down hole appearing in trace amount below 2600 m depth.

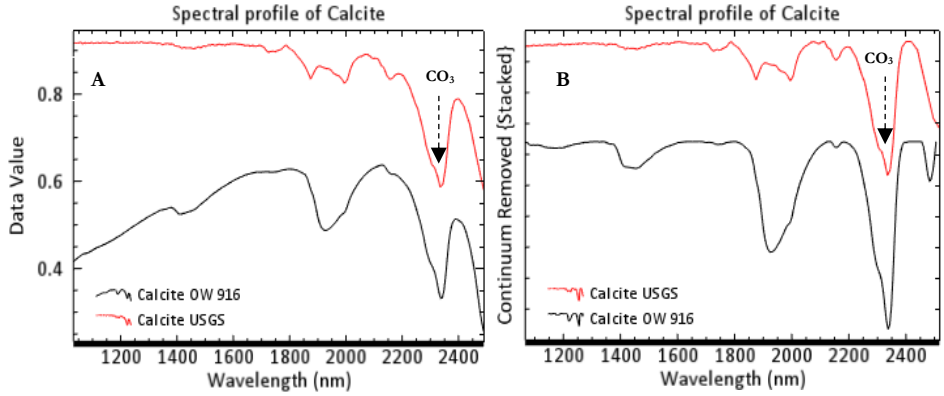

Figure 4-10: Spectral profile of (A) normal reflectance (B)Continuum removed spectra of calcite from OW-916 and USGS spectral library.

- **Spectral mixtures**

Despite having pure pixels from commonly mapped hydrothermal minerals in the study area, spectral mixing posed problems for manual interpretation of the spectra especially for overlapping features. Commonly identified spectral mixture in this study in are illite-chlorite, chlorite-epidote and chlorite-calcite mineral mixtures. Illite-chlorite spectral mixture was indicated by a weak inflection on Al-OH feature by Fe-OH feature near 2240 nm wavelength range(Figure4-11)while chlorite-epidote and chlorite -calcite mixture were identified using by resulting relative deeper characteristic feature(Figure 4-11 C).

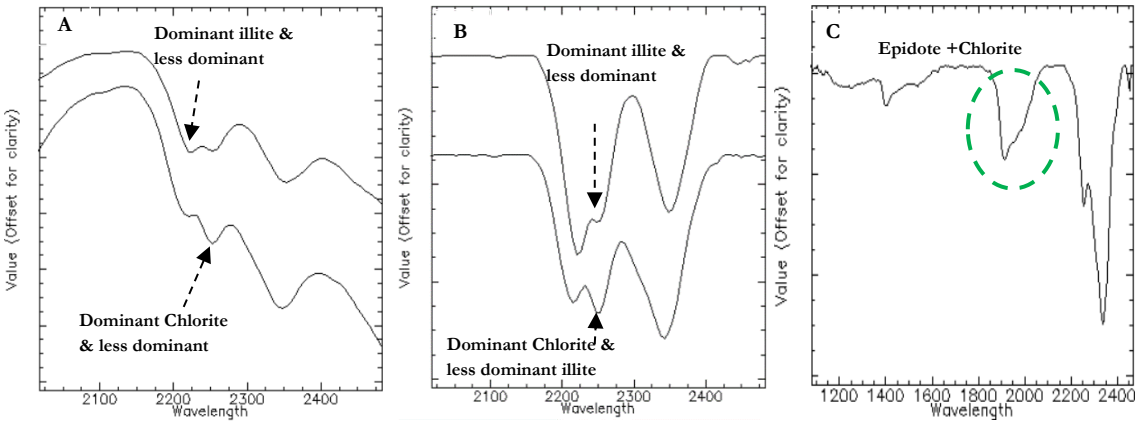

Figure 4-11:Spectral profiled of mixed spectra of dominant illite& less dominant chlorite and dominant chlorite & less dominant illite (A) Normal reflectance (B) continuum removed (C)Spectra mixture of epidote +Chlorite. Note the broad feature(circled) associated with epidote+chlorite mixture.

4.2. Wavelength mapping

Wavelength map results are shown by various wavelength stretches applied on the image in order to distinguish different group of minerals. In this case, the wavelength position of the absorption feature is represented by hue while the depth of the absorption features is represented by the brightness where the brighter the colour the deeper the absorption feature.

4.2.1. Stretch for distinguishing deepest absorption feature

As an illustration, wavelength stretch between 1350-2400 nm wavelength on sample OW-205 (512-514 m) is shown in(Figure 4-12). Light green colour occurring near 1900 nm represent pixels with deepest absorption features.

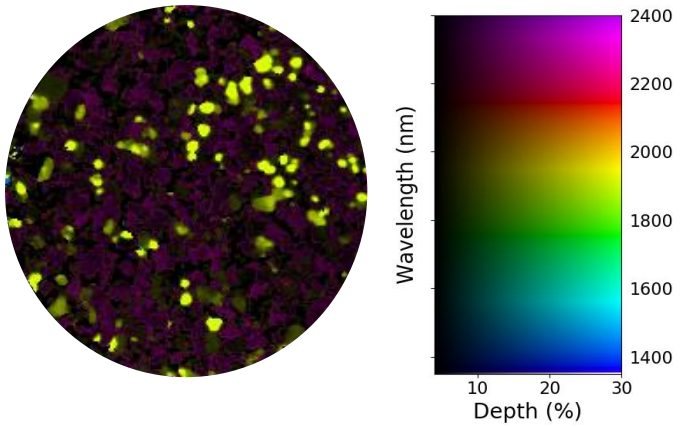

Figure 4-12: Wavelength map for the wavelength stretch between (1350-2400 nm) aimed at identifying the wavelength position of the deepest absorption feature

4.2.2. Zeolite and Smectite group of minerals.

Results for the second stretch range(1850-1950 nm) is as illustrated on sample OW-205 (512-514 m). It shows occurrence of deepest absorption feature near 1900 nm(Figure 4-13). Yellowish colour pixels(1911 nm) correspond to zeolite minerals in this sample as shown in the spectra. However, in the case where the wavelength map highlight both zeolite and smectite using the same hue, visual inspection of the spectra was used to distinguish the them.

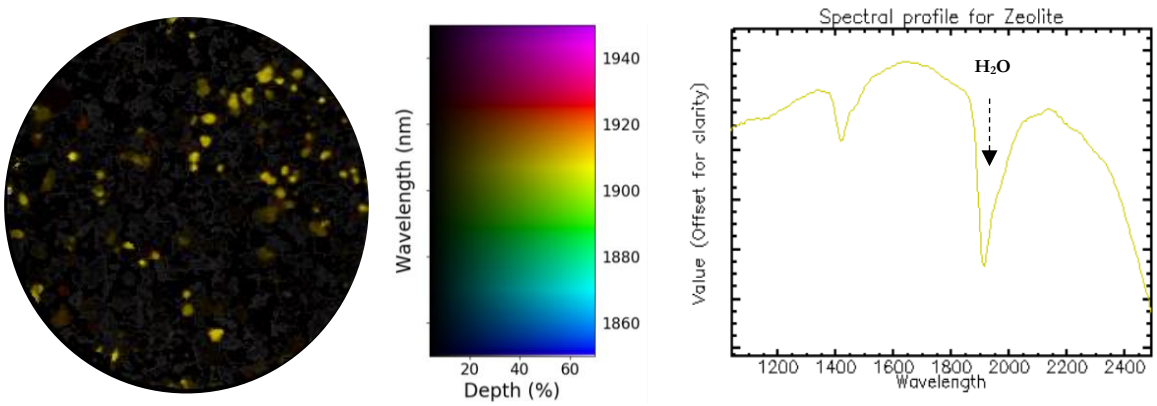

Figure 4-13: Wavelength map for the range between 1850-1950 nm for zeolite mineral OW-205 (512-514 m) and zeolite spectra derived from the image.

4.2.3. Al-OH group of minerals

Results for the second wavelength stretch(2160-2228 nm) is as illustrated on sample OW-916 (478-480 m) (Figure 4-14). The stretch compositionally differentiates various Al-OH minerals found in the sample. For this sample, reddish pixels show minerals shows a mixture of Al-OH and chlorite minerals. This is shown by an inflection on the illite spectra at 2214 nm for the Al-OH -chlorite mixture spectrum. On the other hand, yellowish pixels(2200-2205 shows illite with well-developed absorption features.

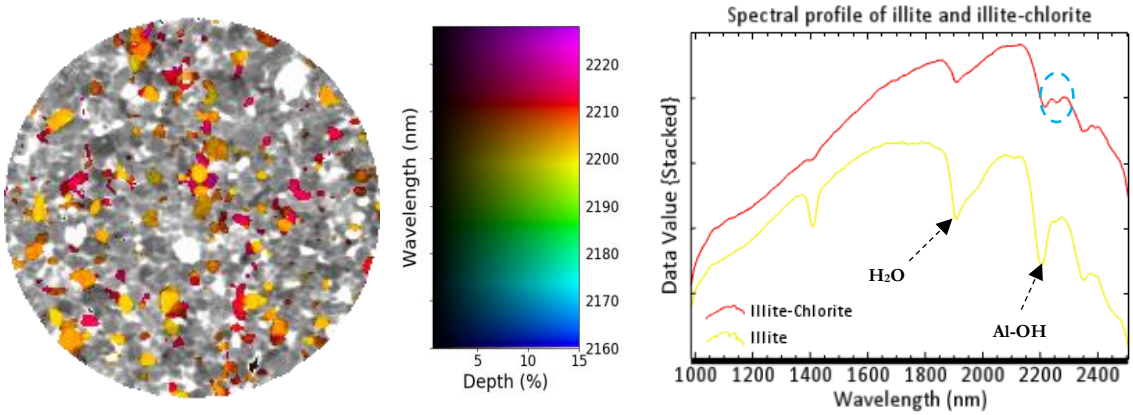

Figure 4-14: Wavelength map for the wavelength range between 2160-2228 nm for sample number OW-916(478-480m) and the spectra derived from the image. Circled part indicates illite-chlorite mixture spectra.

4.2.4. Mg-OH group of minerals

Results for the third stretch(2300-2370 nm) is illustrated on sample OW-205 (2066-2070m)(Figure 4-15). Dominant yellow pixels(2337-2342 nm) corresponds to epidote minerals which is the dominant mineral in this sample. Cyan colour pixels(2314-2320 nm) correspond to actinolite minerals while reddish pixels(2354 nm)corresponds to Mg-OH feature of chlorite mineral.

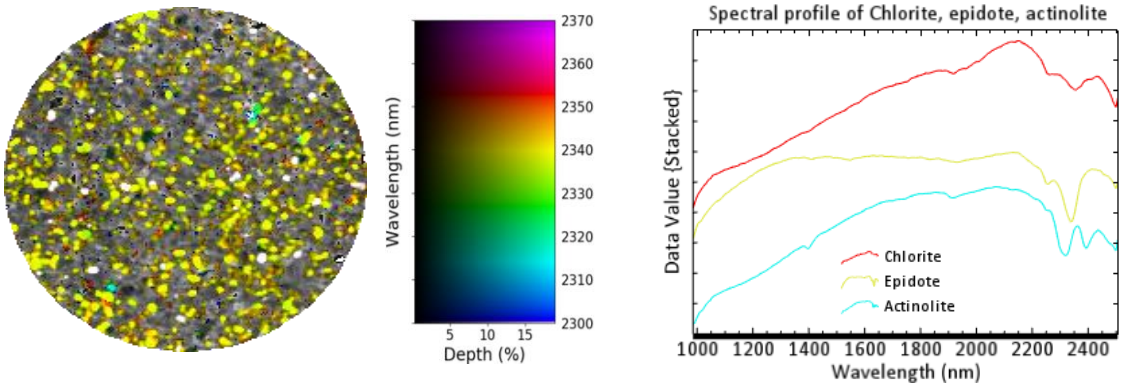

Figure 4-15: Wavelength map for the wavelength stretch(2300-2370 nm) for Mg-OH group of minerals corresponding to chlorite, epidote and actinolite as per the colour code.

4.2.5. Overview of the spatial relationship of Hydrothermal alteration minerals downhole

Results for the fourth wavelength stretch(2100-2400 nm) are as illustrated in scan 4 and 5 from OW-205 (Figure 4-16). The purpose of this scan was to show a general overview of hydrothermal alteration mineralogical changes relative to depth. Greenish pixels(2200-2240 nm) corresponds to minerals containing Al-OH and/or Fe-OH as their characteristic feature. Reddish pixels(2310-2345 nm) corresponds to minerals containing Mg-OH feature whereas yellowish pixels(2270-2290 nm) shows pixels associated with unknown spectra in the SWIR region.

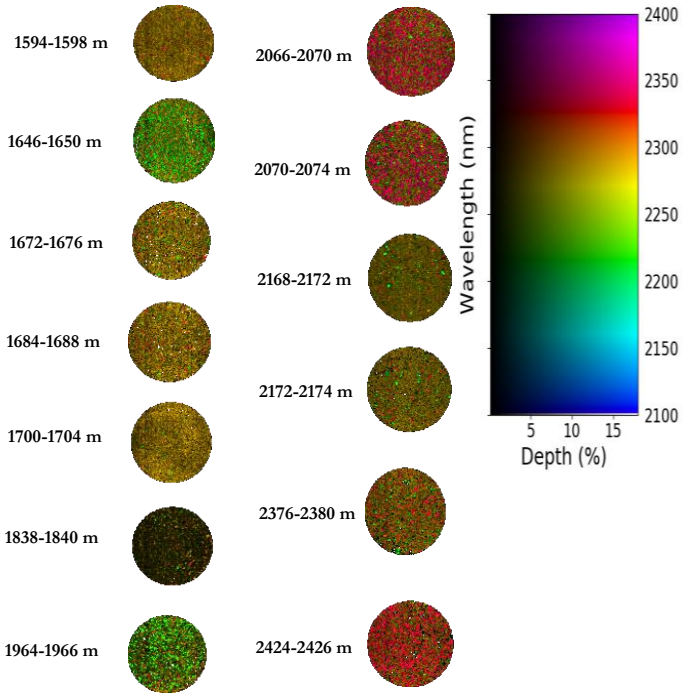

Figure 4-16:Illustration of general overview of variation in hydrothermal alteration with depth. As is observed from wavelength map image. There is compositional change in alteration mineralogy from sample number 1594-1598 m to 2424-2426 m

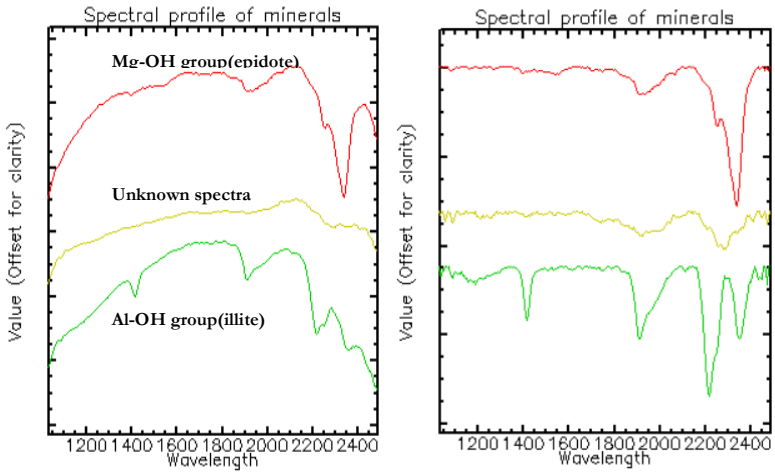

Figure 4-17: Normal and continuum removed spectra of the pixel having deepest absorption feature corresponding to Mg-OH group mineral(reddish colour) , Al-OH/Fe-OH group (greenish colour)mineral and unknown mineral(yellowish colour) spectra derived from 2100-2400 nm stretch.

4.3. Endmember collection

14 endmember spectra were selected to represent various mineral groups identified in the study area. Illustration of the spectral profile of selected endmembers are shown in (Figure 4-18). Besides hydrothermal minerals endmembers, an unknown spectra and quartz sand spectrum were also included in the list to improve classification by minimizing misclassification.

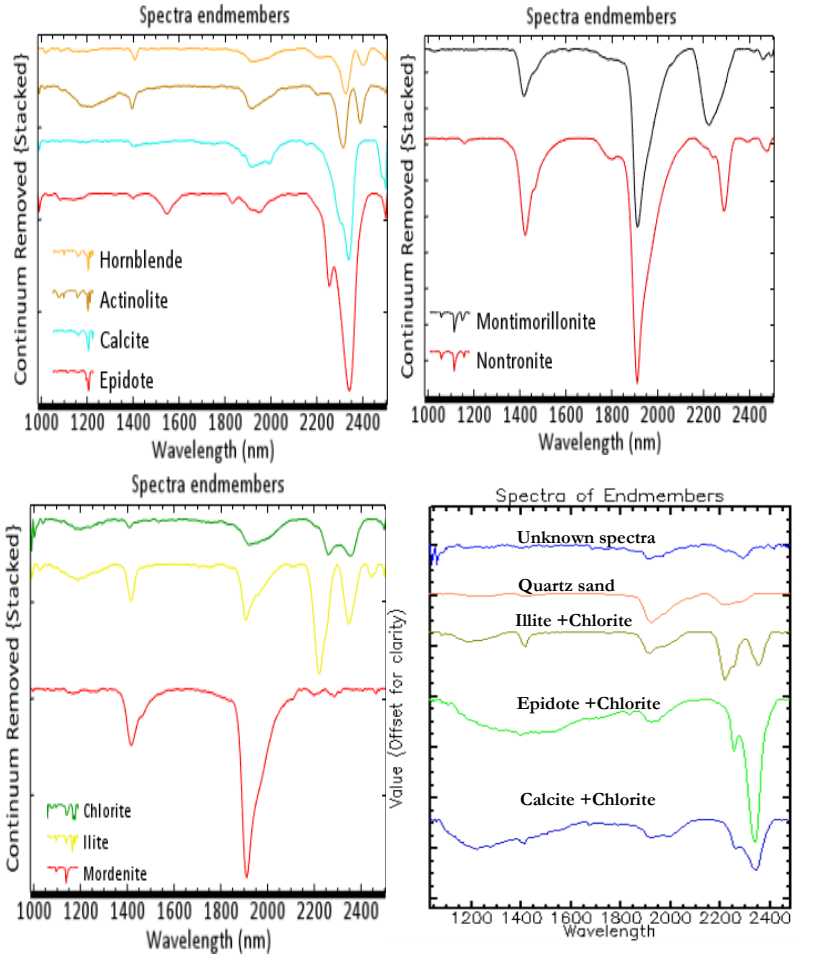

Figure 4-18: Continuum removed endmember spectra.

4.4. Spectral angle mapper(SAM)

The mineral maps resulting from SAM classification allows fast identification of the major spectrally active hydrothermal alteration minerals. Classification results are based on the most dominant mineral species in each pixel where each pixel represent one mineral species. SAM classification was performed for all images with a spectra subset 2100-2400 nm using image-derived endmembers and 0.1 thresholds (*section 4.3*). Use of quartz sand and unknown spectra as part of the endmembers in the classification algorithm was to provide quality control by minimizing misclassification of hydrothermal mineral with seemingly similar spectrum. Relative abundances of minerals in each sample are shown in Appendix III-V. The most commonly hydrothermal mineral classified by this algorithm includes zeolite, smectite, illite, chlorite, calcite, epidote and amphiboles. Mineral mixtures were classified in separate classes to distinguish them from pure endmembers minerals. However, relative abundances(%) of the hydrothermal mineral is low in many of the samples. Unclassified pixels were most abundant in many samples. Unclassified pixels represented minerals with no particular signature in the SWIR region(e.g. quartz, feldspars, albite) or pixels with very noisy pixels to be identified. Relative abundance varied from one depth to another in the three well studied with no link to lithology or temperature change.

OW-205

Hydrothermal alteration minerals classified in this borehole show, chlorite and illite as the major alteration products. They occur as either individual class or as a mixture of either illite-chlorite, chlorite-calcite or chlorite-epidote. Zeolite is the most dominant minerals in the upper alteration sequence in this borehole. Below 800 m depth, chlorite, calcite, illite, epidote and amphibole are the most abundant in that order. However, in most of the samples, unclassified pixels were over 50%. As an illustration, Figure 4-19 show classified image of sample OW-205 (2066-2070 m).

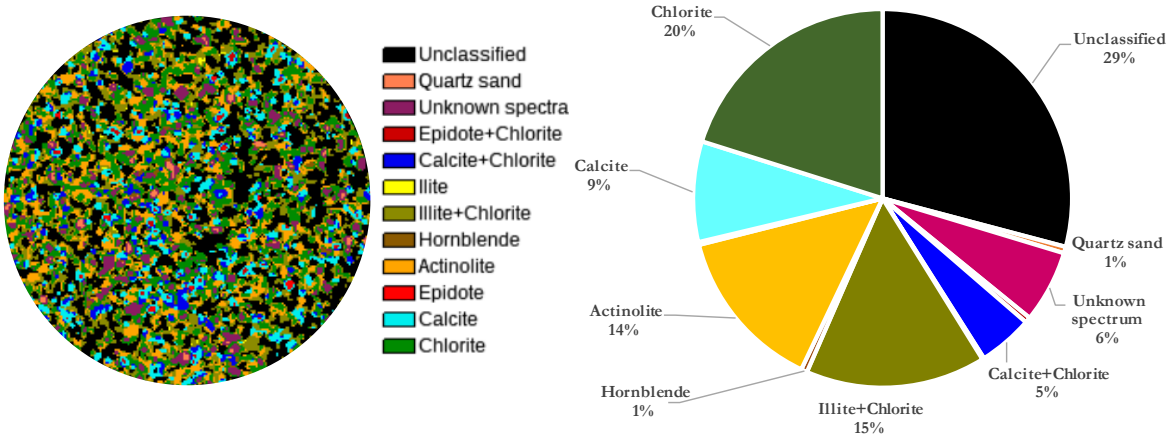

Figure 4-19: Classified image of sample OW-205(2066-2070 m) using Spectral Angle Mapper and relative abundance of dominant minerals.

OW-916

Classification results from this borehole present various degree of alteration. SWIR active mineral in this well are zeolite, illite, chlorite, nontronite, montmorillonite, epidote, calcite, and amphiboles. The average percentage of unclassified pixels increased significantly to over >60%. Correspondingly, the proportion of SWIR active hydrothermal minerals decreased proportionally, especially at a deeper level. At upper alteration sequence, smectite was the most abundant mineral followed by zeolite. Below 1200 m, chlorite, amphibole, calcite, illite and epidote were most abundant following that order. Illite-chlorite and calcite-chlorite mixture were also abundant in this borehole. For illustration, Figure 4-20 show classification results of an upper alteration sequence of sample OW-916 (498-500 m). Chlorite and illite-chlorite mixture are the most predominant minerals in this sample.

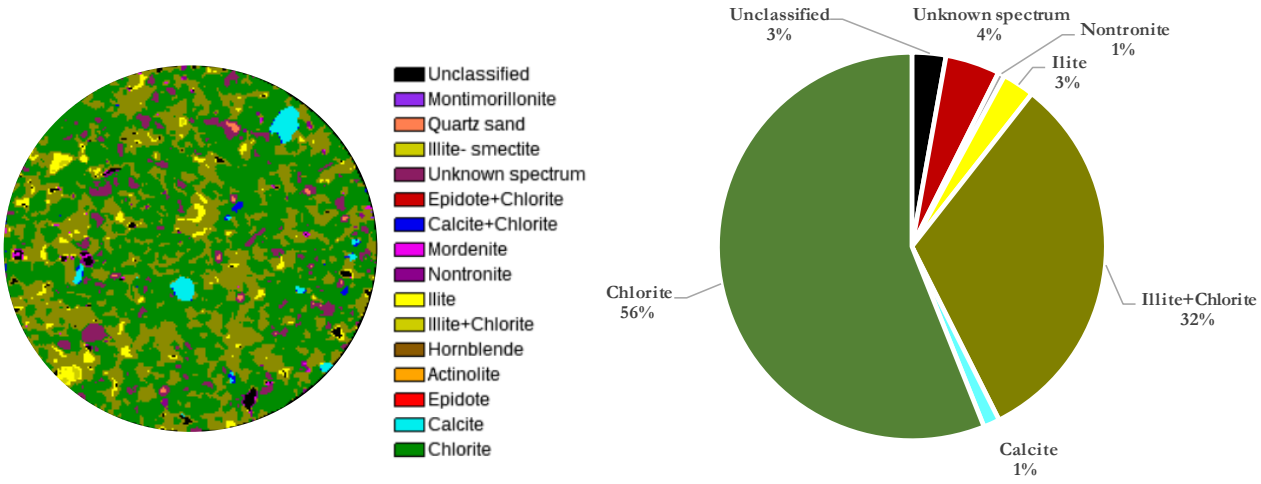

Figure 4-20: Classified image of sample OW-916 (498-500 m) using Spectral Angle Mapper and relative abundance of dominant minerals

OW-917

Classification output highlight zeolite, nontronite, chlorite, illite, calcite, epidote and amphiboles. Analogous to OW-916, there is a significant increase in the percentage of unclassified pixels in this borehole with an average of > 80% being observed. Equally, there is a decrease in in relative abundance of SWIR active hydrothermal minerals. Zeolite and smectite were most abundant at upper alteration sequence(<400 m) depth while chlorite, amphibole, illite and calcite were the most abundant at a deeper level. Relative proportion varied from one depth to another with no systematic sequence observed between relative abundance and depth. For illustration, Figure 4-21 show classifications result for sample OW-917(1956-1960 m).

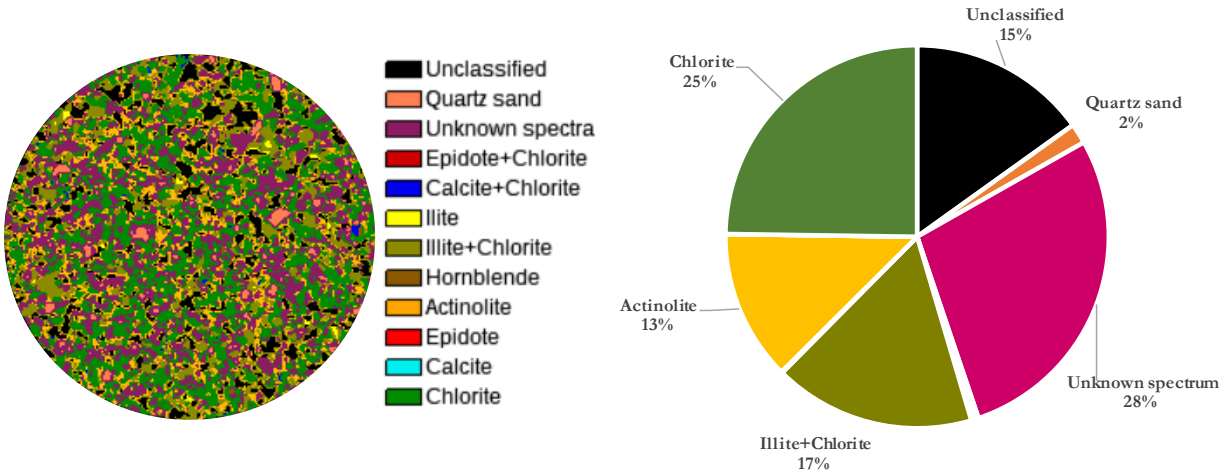

Figure 4-21: The classified image of sample OW-917 (1956-1960 m) using Spectral Angle Mapper and relative abundance of dominant minerals.

4.5. Illite Crystallinity index

Comprehensive crystallinity was determined in OW-205. In OW-916 and OW-917, detailed comparison between crystallinity and temperature was not achieved due to limited number of samples with pure illite pixels. Figure 4-22***A*** are whisker plots showing illite crystallinity distribution per sample in OW-205 while Figure 4-22***B*** show a composite plot of average crystallinity values and measured formation temperature against depth. Colour variation observed in the figure does not represent changes in crystallinity but are for visualisation purpose. Number of pixels used for each class are as indicated in Appendix VIII

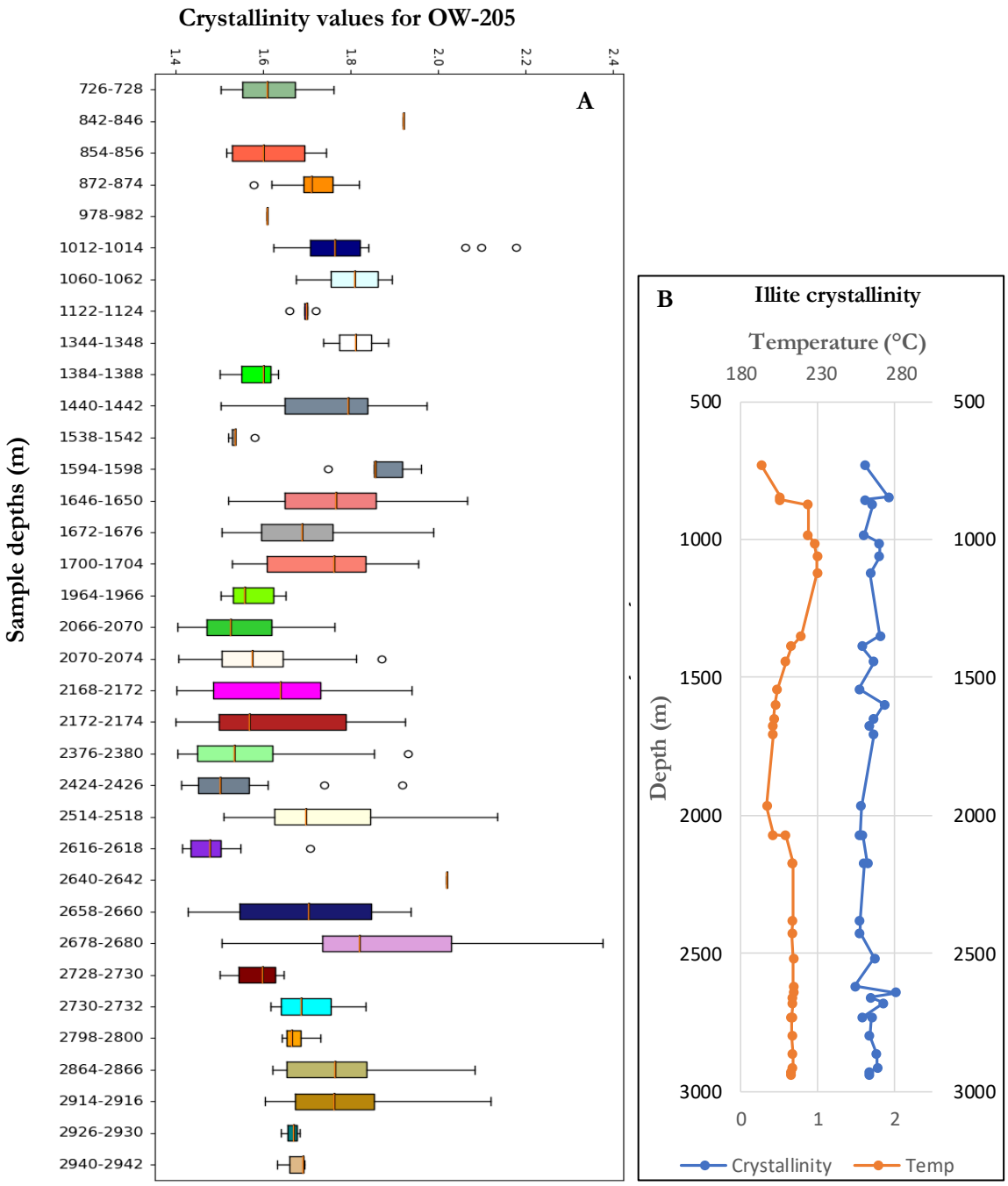

Figure 4-22: Crystallinity index value of samples from OW-205(A) Whisker plots showing variation of crystallinity in a sample (B) A composite plot of average crystallinity values and measured formation temperature.

From the results, the interquartile range rises steadily with the increase in depth from 720 m to 1350 m depth. Below this depth, erratic pattern of interquartile ranges is observed. However, there is a steady rise of the interquartile range observed below 2700 m depth. Sample 1012-1014 m, 2070-2074 m, 2376-2378 m and 2424-2426 m show high variation in crystallinity values. This is despite the fact that they all come from the same lithological unit(trachyte) with exception of sample 1012-1014 m which is a rhyolite. In Figure 4-22***B,*** there is a positive correlation between temperature and crystallinity values with depth from 720 m to approximately 1150 m depth. Below this depth, average crystallinity values remain high despite decrease in measured formation temperature.

4.6. Hyperspectral data validation using XRD measurement.

To validate SWIR identified minerals, a total of 15 samples (5 from each well) were analyzed using Bruker D2 Phaser XRD. From the results, hydrothermal minerals identified in SWIR highly matched with those identified by XRD. From the result, chlorite, calcite, illite, nontronite, epidote, and amphibole previously recognized by SWIR were identified by XRD. Most notably is identification of high proportion of quartz and feldspars which are inactive in SWIR spectroscopy. Table 4-1 shows relative abundance of mineral identified by XRD. High proportion of quartz and feldspars from XRD could be matched with the unclassified pixels derived from the SAM classification algorithm in SWIR hyperspectral imaging. To illustrate, Figure 4-23 shows a diffractogram for sample OW-916(498-500 m) showing mineral peaks for minerals identified by XRD technique.

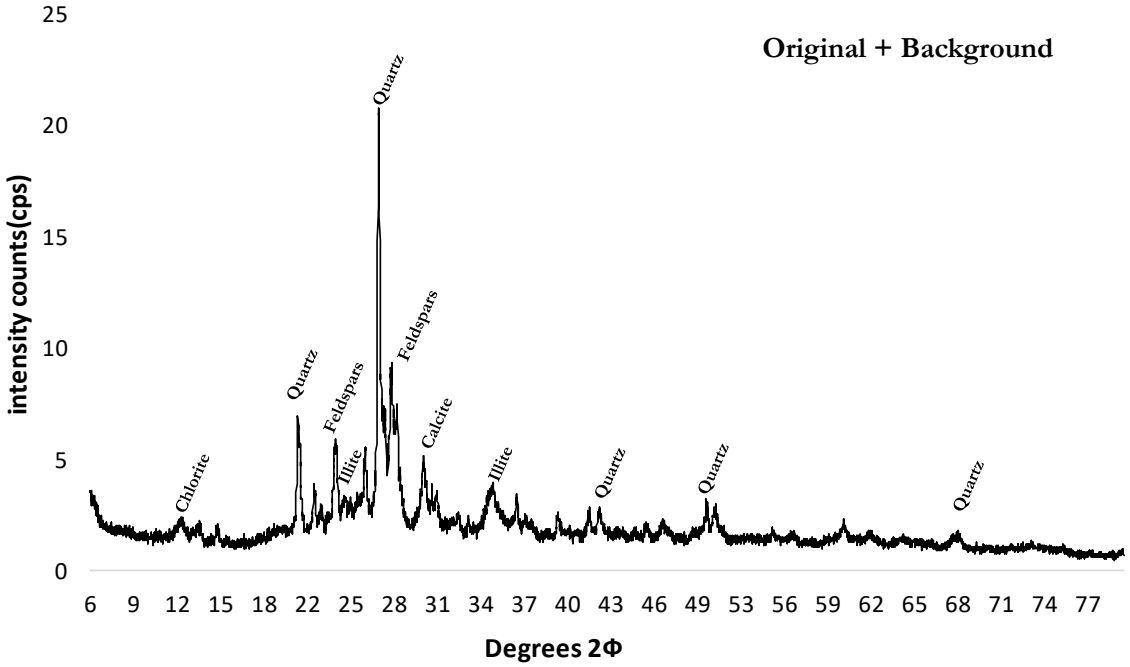

Figure 4-23: Representative XRD pattern of sample OW-916(498-500 m) showing peaks of illite, chlorite, quartz, illite and feldspars. Illite and chlorite hydrothermal minerals were earlier identified in SWIR as shown in Figure 4-20.

Table 4-1: Proportion of minerals in % obtained from XRD measurement

Borehole	Sample number(m)	Feldspars	Quartz	Calcite	Chlorite	Illite	Nontronite	Epidote	Amphibole
OW-205	728-730	44.17	29.81	2.97	5.97	14.83	2.24	0	0
	1594-1596	66.48	11.67	3.47	6.89	11.5	2.13	0	0
	1700-1704	50.87	26.03	2.56	5.58	12.83	0	0	0
	2066-2070	50.93	7.63	2.43	3.83	8.59	0	10.85	16.29
OW-916	498-500	46.73	26.57	4.07	7.52	15.11	0	0	0
	1288-1290	53.24	3.7	4.17	5.22	12.4	0	10.68	10.58
	1888-1890	38.85	20.36	3.69	5.82	11.02	0	8.18	12.09
	2668-2670	37.69	32.01	0	7.68	15.94	0	6.69	0
OW-917	930-934	54	26	3.75	1.5	2.7	0	0	0
	1956-1960	41.85	32.56	2.61	7.51	15.33	0	0	0
	2480-2482	38.46	35.26	1.95	7.3	17.69	0	0	0
	2938-2940	66.67	7.83	2.5	6	11	0	0	3.79

4.7. Comparison between SWIR and XRD mineral relative proportions

Relative abundances of hydrothermal minerals quantified by XRD were compared with those derived from SAM classified images. During relative abundance determination, unclassified pixels in SWIR and highly abundant quartz and feldspar minerals in XRD were considered. For unbiased comparison, both quartz and feldspars identified in XRD and unclassified pixels in SWIR were not considered. Therefore, comparison of relative abundance from the two techniques considered the most common hydrothermal minerals such as calcite, chlorite, illite, epidote and amphibole. For SAM classified images, relative abundances derived from mixed spectral class such as illite-chlorite, calcite-chlorite or epidote-chlorite were divided equally into two and distributed to pure spectral class of each mineral in the mixture. This was based on the hypothesis that the mixture has equal proportion of each mineral in a class. Relative abundance of actinolite and hornblende were gathered into one class of amphibole. Figure 4-24 to 26 are scatter plots showing a comparison between mineral proportion derived from SWIR and XRD techniques for some selected samples.

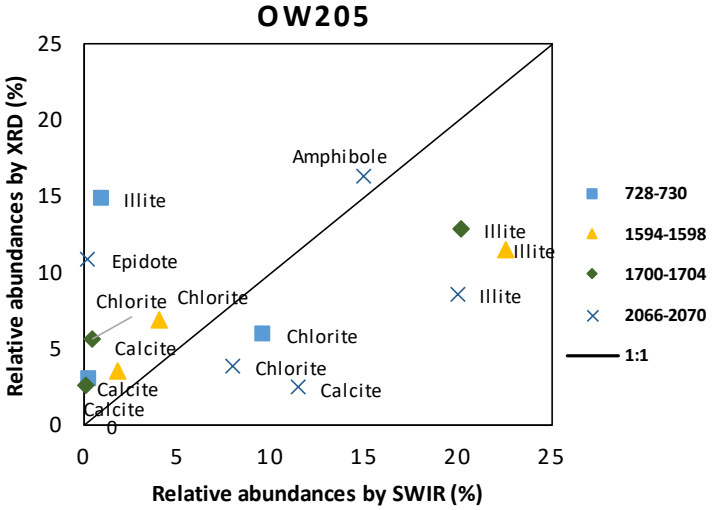

Figure 4-24: Comparison of relative abundances of hydrothermal minerals derived from SWIR and XRD techniques in OW-205

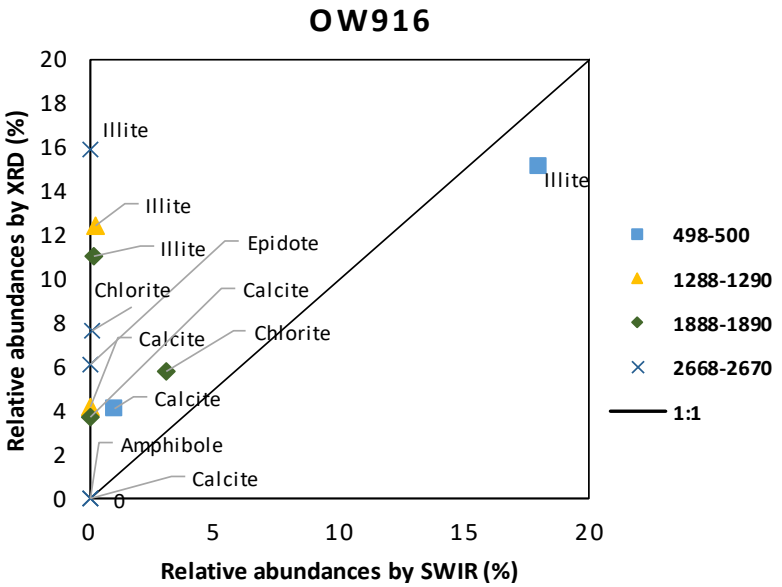

Figure 4-25: Comparison of relative abundances of hydrothermal minerals derived from SWIR and XRD technique in OW-916.

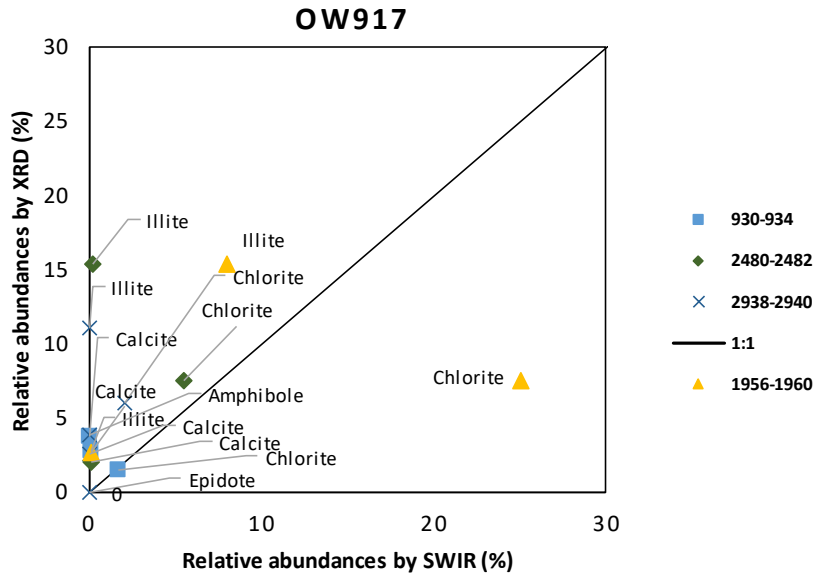

Figure 4-26: Comparison of relative abundances of hydrothermal minerals derived from SWIR and XRD technique in OW-917.

From the plots, its is observed that illite and calcite are overestimated in XRD while chlorite is overestimated in SWIR in many of the samples analyzed. However, in sample OW-205 (2066-2070 m), the relative abundance of amphibole is highly correlated. Generally, mineral abundances derived from the two techniques are highly uncorrelated in all the samples from the three geothermal wells. These could be attributed to sample characteristics (e.g. amorphous samples), variable degrees of structural order, sample particle size(powder, drill cuttings) and sample preparation procedures and analysis.

4.8. Data Integration

A comparison of lithology, temperature, alteration mineralogy, spectral parameters of illite and chlorite mineral, relative mineral abundance derived from SAM classification and the alteration zones were plotted together on each well as shown in (Figure 4-27 to 29). In OW-205(cold in-flux well), trachyte, tuff and basalts are the main lithological unit intersected at shallow depth. Below 1000 m depth, trachyte predominates with basaltic intercalation being observed near 2500 m depth. There is a correlation between measured formation temperature and temperature stability range of hydrothermal minerals formed between 700-1350 m depth. However, below 1350 m depth, a decrease in measured formation temperature(<200^{0}C) don't correspond with temperature stability range of hydrothermal alteration minerals observed at this depth.

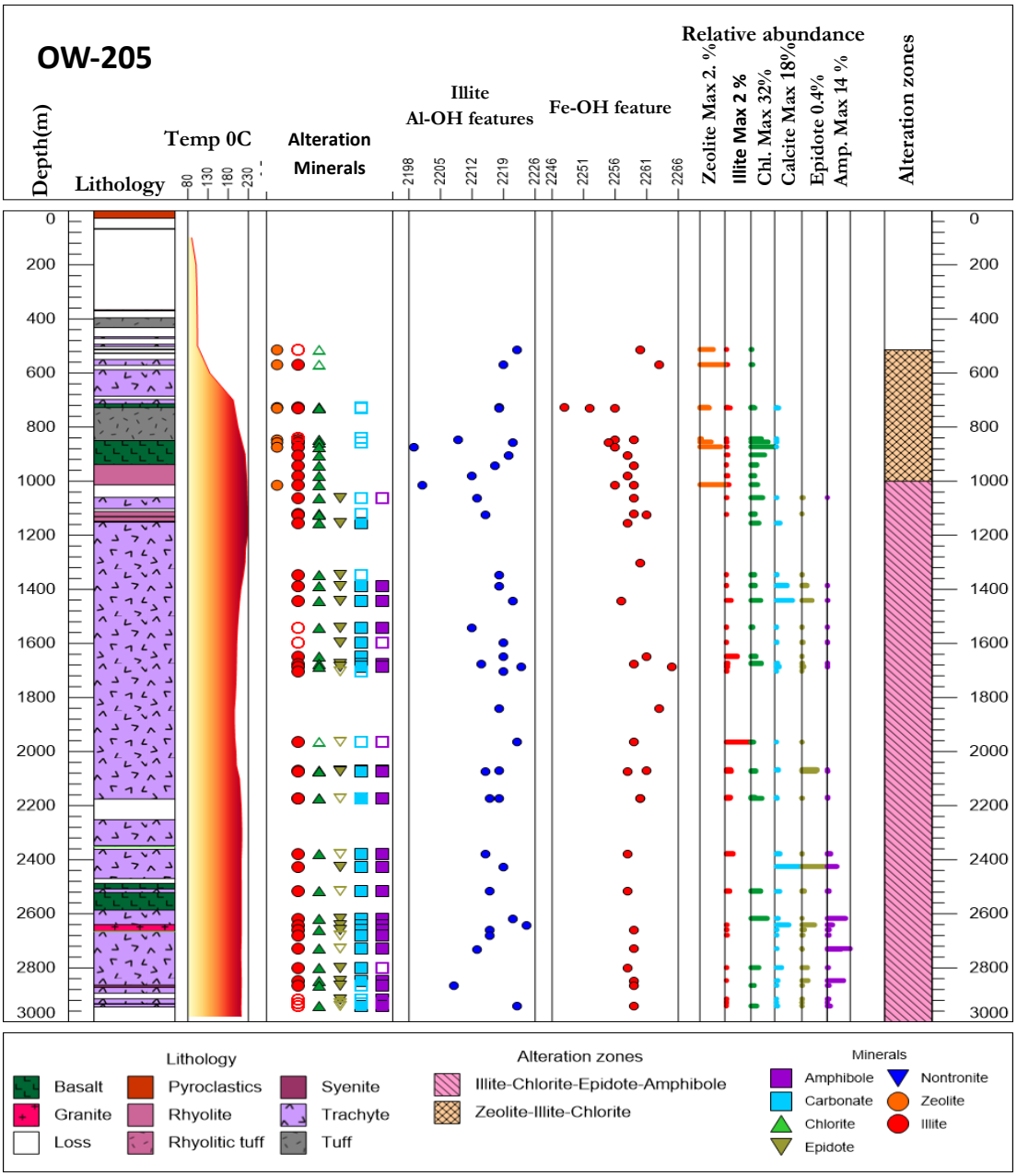

Figure 4-27: SWIR identified hydrothermal minerals and spectral parameters plots for illite and chlorite compared against lithology, measured well temperature, relative abundances and the alteration zone for OW-205. The filled mineral symbols represent minerals that were abundantly identified while the open one represents trace amount. The maximum relative abundance obtained for each mineral is indicated alongside mineral in the mineral column. Temperature and stratigraphic data used for this well was supplied by KENGEN.

In OW-916, trachyte, rhyolites and basaltic intrusion as the main rock units intersected in this borehole. The hydrothermal mineral distribution shows a prograde type of alteration where low-temperature minerals such as zeolites, smectites(e.g. nontronite, montmorillonite) appear at shallow depth while high-temperature indicator minerals(e.g. amphiboles, epidotes) being formed at deeper depth(Figure 4-28). There is a systematic relationship of mineral assemblages formed with measured formation temperature in respect to depth. However, there is a general decrease in the occurrence of SWIR active minerals in this borehole.

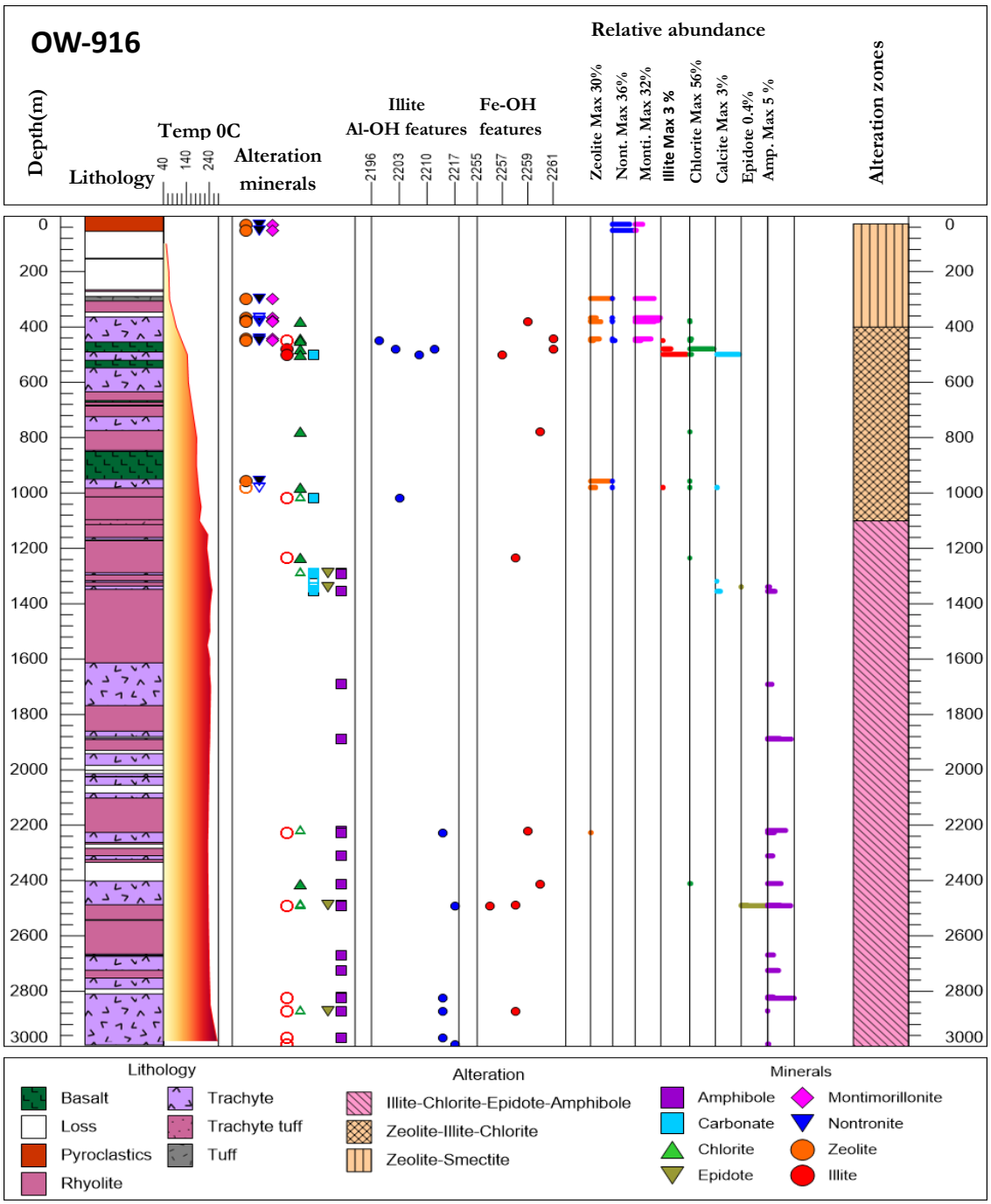

Figure 4-28: SWIR identified hydrothermal minerals and spectral parameters plots for illite and chlorite compared against lithology, measured well temperature, relative abundances and the alteration zone for OW-916 an up-flow well. The filled mineral symbols represent minerals that was abundantly identified while the open one represents trace amount. Temperature and stratigraphic data used for this well supplied by KENGEN.

In OW-917, stratigraphy of this well mainly comprises trachyte, rhyolite and basalt. Downhole, there is a decrease in the occurrence of SWIR active minerals in this borehole. Low-temperature indicator minerals namely zeolite and smectite are formed at <400 m depth. Amphibole typically a high-temperature indicator mineral extends towards shallower levels near 600 m(Figure 4-29). Illite and chlorite appear abundantly below 1700 m depth in association with calcite and epidote.

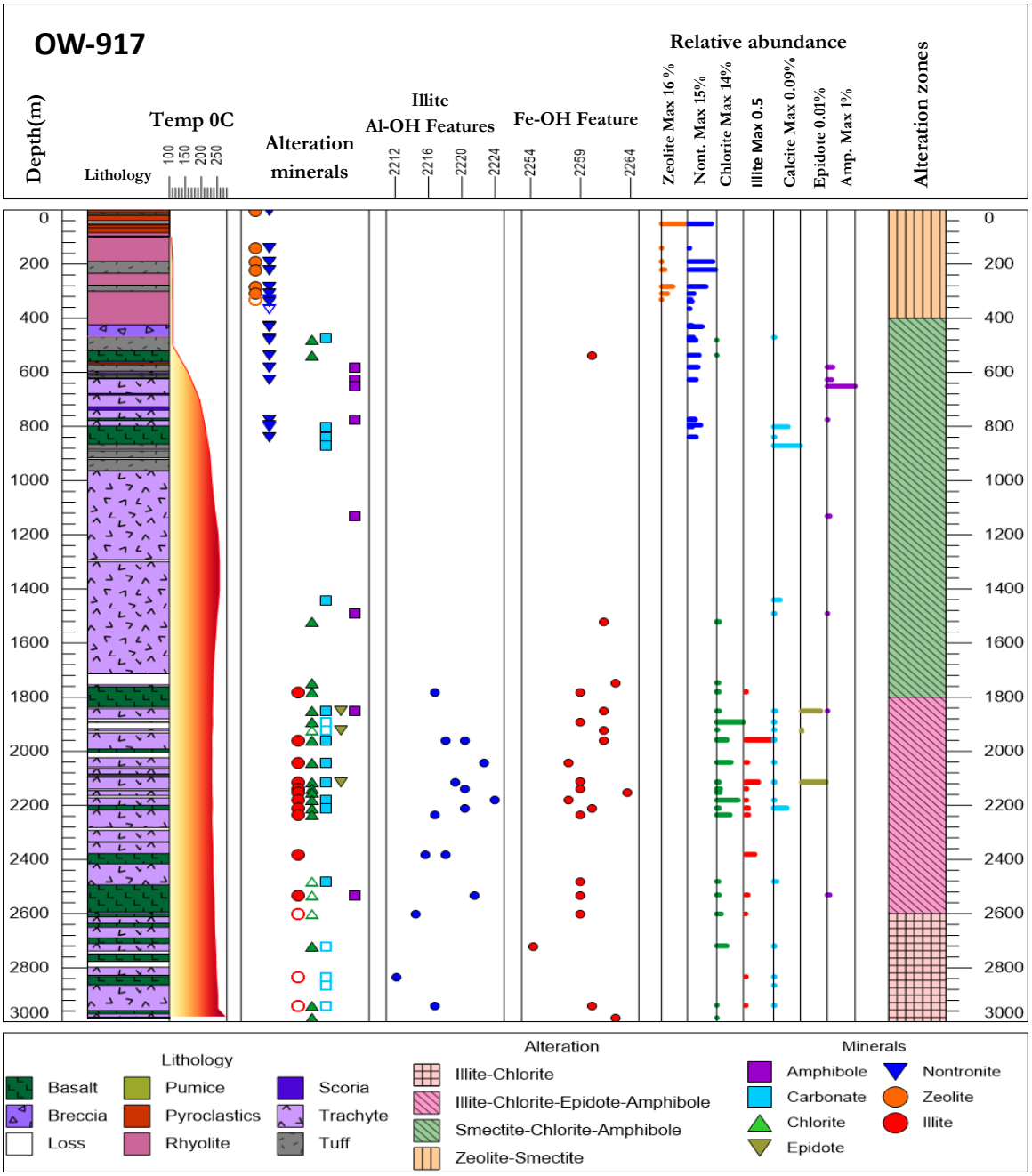

Figure 4-29: SWIR identified hydrothermal minerals and spectral parameters plots for illite and chlorite compared against lithology, measured well temperature, relative abundances and the alteration zone for OW-917 an up-flow well. The filled mineral symbols represent minerals that was abundantly identified while the open one represents trace amount. Temperature and stratigraphic data used for this well was supplied by KENGEN

4.9. Hydrothermal alteration zones

Spectral identification of drill cuttings from the studied borehole reveals different alteration zones. Each zone represents particular mineral assemblages depending on temperature stability range. In this study, alteration zoning was defined based on spectral data acquired from drill cuttings starting from the shallowest depth to the hole bottom. In line with this, alteration zoning of OW-205 start from 512 m depth while for OW-916 and OW-917 start from 30 and 50 m depth respectively. The following section discusses mineral assemblages identified for each borehole:

OW-205

Zeolite-Illite-Chlorite zone

This is the first zone identified in this borehole ranging between 500-900 m depth. Predominant rock unit in this zone are tuff, trachyte and basaltic intercalations. Measured formation temperature is <200^{0}C. The lower end of this zone is marked by the disappearance of zeolite(mordenite) and the appearance of epidote and amphibole at a temperature of >200^{0}C.

Illite-chlorite-epidote-Amphibole zone

It is recognized below 1000 m depth with the formation of temperature >200^{0}C. The main lithological unit in this zone is trachyte with minor basaltic intercalation appearing at deeper depth(> 2400 m). This mineral assemblage persists up to the bottom of the hole. The appearance of epidote at this zone is accompanied by the presence of zeolite(wairakite). Measured formation temperature observed between 1350-2200 m depth in this zone are lower than the mineralogical temperature. This suggests a cooling geothermal reservoir.

OW-916

Zeolite-Smectite zone

It occurs below 500 m depth with a formation temperature of <140^{0}C. The main rock unit in this zone are rhyolite, trachyte and pyroclastic materials. It is defined by the presence of mordenite and smectite which are low-temperature indicator minerals. Smectite is highly abundant in this zone. The lower transition boundary is marked by the appearance of both illite and chlorite.

Zeolite-illite-chlorite zone

This zone occurs between 500-1000 m depth with a measured formation temperature of below (<180^{0}C. Rhyolite, trachyte and minor basaltic rocks are the main lithological unit recognized in this zone. The lower boundary of this zone is marked by the appearance epidote at approximately 1200 m depth.

Illite-chlorite-epidote-amphibole zone

This occurs from 1200 m depth up to the bottom of the borehole. Rhyolites and trachyte are the main lithological units recognized in this zone. It is the final alteration zone encountered in this borehole with amphibole persisting downhole through this zone. Epidote occurs sporadically in this zone. Measured formation temperature is >220^{0}C in this zone.

OW-917

Zeolite-smectite zone

It occurs between 50-400 m depth. The main lithological units within this zone are rhyolitic and tuffaceous materials. It is characterized by the occurrence of zeolite and smectite. Measured formation temperature of <100^{0}C is observed. The lower boundary is marked by the appearance of chlorite.

Smectite-chlorite-amphibole zone

It occurs between 400-1800 m depth with a measured formation temperature of>200^{0}C. Trachyte, basalts and tuffaceous intercalations are the main lithological units recognized in this zone. The zone is characterized by the appearance of amphibole at a shallower depth(600m) in association with chlorite and nontronite. Amphibole appearance is sporadic. Lower boundary which is characterized by the appearance of illite and epidote minerals.

Illite-chlorite-epidote-amphibole zone

It occurs between 1800-2600 m depth with measured formation temperature of <220^{0}C. Trachytic rocks and minor basaltic intercalations are the main lithological unit recognized in this zone. It is characterized by first appearance of epidote(trace amount).Lower boundary in this zone is marked by the disappearance of amphibole near 2600 m depth.

Illite-Chlorite Zone

This is the final alteration zone encountered in this borehole occurring between 2600-3000 m depth. Main lithological unit intersected in this zone are trachyte and basalts. It is defined by the disappearance of both epidote and amphibole minerals both of which are high-temperature indicator mineral. Measured formation temperature within the zone is <220^{0}C.

5. DISCUSSION

Results from this study confirm the effectiveness of SWIR Hyperspectral imaging spectroscopy in determining hydrothermal alteration minerals from drill cuttings sampled from a geothermal system. Hydrothermal minerals identified from Olkaria geothermal system using SWIR hyperspectral technique corroborate with the documented alteration minerals from previous studies using conventional methods(e.g. Lagat ,2007; Ronoh, 2015; Musonye, 2015; Mwangi, 2016; Otieno, 2016). Hydrothermal mineral assemblages identified from the three wells in different hydrologic zones correspond to the hypothesized up-flow, out-flow and cold-influx zone in a geothermal system. However, the method is limited to minerals active in the SWIR region. Thus, minerals such as quartz, adularia and albite which are important hydrothermal constituents in a geothermal system but active in Long Wave Infrared(LWIR) and goethite/hematite which are possible indicators of in-flux of cooler fluids but active in VNIR region were not studied.

Hydrothermal minerals and mineral assemblages

Variation in hydrothermal minerals and mineral assemblages has previously been used as an effective way to infer temperature, a guide to field hydrology which is critical in determining production casing depth, deducing permeability and estimating fluid pH and composition (Reyes, 1990). For instance, Browne (1978) indicated stability range of epidote as a temperature above 220 ^{0}C. On the other hand, Reyes (1988), indicated the occurrence of high-temperature indicator minerals(e.g. epidote, actinolite) in a production zone with a temperature lower by 20 ^{0}C their mineralogical temperature as indicating a cooling reservoir hence such minerals are considered relict. Correspondingly, the occurrence of hydrothermal minerals in a measured formation temperature 20 ^{0}C higher than their mineralogical temperature indicates a heating reservoir. In this study, hydrothermal mineral alteration patterns are reflected downhole with minerals occurring in association with each other depending on their temperature stability ranges. For instance, epidote and actinolite occur in association at temperatures above 220 ^{0}C whereas the assemblage of zeolite and smectite depict low temperatures (<180 ^{0}C) and shallow depth confirming to previous studies by Bish (2013) which indicated them as low-temperature indicator minerals(Figure 4-27 to 29).

In well OW-205, which is considered to be experiencing incursion of cooler fluids, the occurrence of zeolites up to a relatively deeper depths i.e. 700 m depth(Figure 4-27) is attributed to low temperature in this zone. The apparent occurrence of zeolite at 1000 m with a measured formation temperature of above 230 ^{0}C is interpreted as wairakite a calcium-rich zeolite formed in an active hydrothermal system with stability temperature above 200 ^{0}C (Browne, 1978). In this case, differences in stability temperature of mordenite and wairakite was applied to distinguish the two minerals. As pointed by Yang et al. (2001), mordenite and wairakite have similar spectral characteristics making it difficult to distinguish them spectrally. The results show a concomitant occurrence of illite and chlorite from 500 m downhole. Occurrence of illite at this measured formation temperature conifirms earlier studies by Browne (2000) which indicated stability range of illlite bieng above 180 ^{0}C. The occurrence of chlorite across the whole depth confirm earlier study by Browne (1970) which indicated unsuitability of chlorite as a geothermometer due to its stability over a wide range of temperature. Consequently, chlorite was not used to infer temperature in this well.

Presence of epidote and amphibole mineral between 1500-2200 m depth with measured formation temperature <200 ^{0}C, is perhaps the biggest temperature anomaly encountered in this study. With stability range of epidote and amphibole being >220 ^{0}C, their presence at this depth could be interpreted as being relict and does not reflect the prevailing thermal conditions. Therefore, these minerals were formed when the temperature was higher and hence the system could be experiencing temperature reversals due to the cooling effect from cold water incursion. In OW-205, calcite occurs together with other alteration minerals such as illite and chlorite showing a general trend of persistence with depth. The occurrence of calcite in

such pattern has been recognized by previous studies(e.g Simmons & Christenson, 1993) and is attributed to the formation of calcite by replacement of rock-forming minerals through hydrolysis due to boiling liquid containing CO_2 gas. According to Simmons & Christenson (1994), presence of near vertical channels where boiling fluid rises, result to loss of CO_2 which causes reduction of pressure in a geothermal sytem. Consequently, this leads to the precipitation of platy calcite in open spaces(e.g vugs, fracture and vesicles) leading to the clogging fo the permeable patheway.

Convincingly, information derived from the relationship between measured formation temperature and mineral assemblages from this well may infer OW-205 as experiencing influx of cooler fluids. However, for complete interpretation using spectral data, VNIR data that can successfully identify goethite and hematite which according to Reyes (1998), are commonly formed in cooler zones is required. Nonetheless, information derived from mineral assemblages and measured formation temperature in this well can be used for decision making about the prevailing status of the well and any future geothermal development in its vicinity. For example, the decline in temperature between 1500-2200 m could be associated with high permeability due to high fault intensity observed in this area, thus allowing cooler fluids to enter the system along fault lines. Correspondingly, presence of high-temperature minerals(epidote, amphibole) within this section does not coincide with the prevailing temperature and is thus associated with cooling geothermal reservoir and may therefore not be appropriate area for siting of subsequent production wells.

Hydrothermal alteration and mineral assemblages observed in up-flow well (OW-916)(Figure 4-28)are largely in equilibrium with the measured formation temperature. In this case, minerals display a prograde pattern of alteration where low-temperature minerals(e.g. zeolite-smectite) form at shallow depth and high-temperature minerals(e.g. epidote, amphibole) form at deeper levels. High abundance of smectite derived from spectral data at a shallower depth(< 450 m) can be interpreted as the clay cap which is an impermeable layer formed by upwelling of geothermal fluids from depths. The appearance of epidote and amphibole at around 1350 m depth at measured formation temperature >200 ^{0}C corresponds to its lower stability limit (Bird, 1983). In contrast, occurrence of calcite in a localized zone(500-1400m) can be interpreted as being due to replacement where the hydrothermal fluids react with precursor rock material to produce carbonate. Occurrence of calcite between 1300-1400 m depth in association with epidote and actinolite confirm earlier finding by Simmons and Christenson (1993) which indicated that calcite formed by replacement method occurs in diversity of other alteration minerals and over a wide range of temperature (<125^{0}C to >290^{0}C. In accordance with the previous finding by Simmons & Christenson (1994), the formation of replacement calcite prevails in the up-flow zone of a geothermal system. This observation confirms previous studies by (e.g Lagat 2007; Musonye 2015; Mwangi 2016) which indicates OW-916 as being located in an up-flow zone.

With the hydrothermal alteration pattern in this well being recognized by spectral data, the information derived can not only be used for aiding future siting of geothermal well but also in deciding optimum depth for setting production casing. For instance, high-temperature minerals(epidote, amphibole) in this well occurs after 1250 m and therefore the best depth to install perforated casing to realize optimum production will be about 1300 m depth. Equally, abundance of smectite(swelling clays) identified and quantified using spectral data at shallow depth can be used to anticipate the possibility of a stuck pipe during drilling and therefore this information can offer immediate practical application by advicing drilling engineers about the sub-surface geology they are drilling through for correct remedial action.

In out-flow well (OW-917), the relationship between measured formation temperature and hydrothermal mineral assemblages shows a retrograde alteration pattern. As illustrated in (Figure 4-29) hydrothermal mineral assemblages formed shows temperature reversal where high-temperature minerals(amphibole) are formed at shallower depth. Sporadic appearance of amphibole with depth and its eventual disappearance from 2600 m depth is interpreted as due to decrease in temperature below their formation temperature. Appearance of illite at deeper depth(1700-2200 m) is interpreted as due to improved permeability associated

with close lithological boundaries of trachytic and basaltic rock intercalations observed in this region. Largely, spectral measurement in this borehole shows scarcity of alteration mineral active in SWIR region despite high measured formation temperature(>200 ^{0}C) experienced. This is interpreted as due to low permeability and lack of sub-surface faults and fracture which allows hydrothermal fluids flow.

Use of spectral data in this well has recognized mineral assemblages associated with the characteristics of an out-flow well. Past studies by Maribel (1988) indicated presence of alteration reversal as is the case of OW-917 as due to flow of cooler fluids along faults which is commonly formed in geothermal wells located at the margins of a geothermal resource and also the inhibition of fluid flow by impermeable horizon at depth. This corresponds with what is observed spectrally in OW-917 and hence confirm earlier study by Musonye (2015) which interpreted OW-917 as being located at the periphery of Olkaria geothermal system. Ultimately, hydrothermal minerals and mineral assemblages identified spectrally in this well can be used to identify and delineate the extent of a geothermal resource, recharge zones and best locations to site re-injection wells.

Formation and composition variation of illite

Illite is formed as a result of the alteration of original rock material by reacting with hydrothermal fluid at a given temperature (Tardy et al., 1987). Therefore, chemical composition of illite should reflect the bulk chemical composition of the original rock material, chemical composition of the solution and the temperature of the formation. Variation in wavelength position of Al-OH feature in illite has been used to effectively estimate the chemical composition of illite in a hydrothermal system (Yang et al., 2011). Massonne and Schreyer (1987), indicated composition variation of illite to be a function of physical and chemical conditions resulting from substitution featuring replacement of Al^{3+} with either Fe^{2+}, Fe^{3+}or Mg^{2+} in a hydrothermal system. Previously, several studies have used composition and occurrence of illite to understand the thermodynamic properties of water-rock interaction during the hydrothermal process. For instance, Vidal et al. (2018) indicated illite as a potential indicator of permeability both in the present and fossil geothermal system. Likewise, Yang et al. (2011) linked white mica composition to mineralization or intense hydrothermal alteration process. In this study, distribution and compositional characteristics of illite was used to infer temperature of the geothermal reservoir and to aid in interpretation of the hydrology of the system.

Compositional differences of illite in OW-205 are shown in Figure 4-27. It is evident that between 800-1000 m depth, there is a wide variation in wavelength shift (2198-2224 nm) of Al-OH feature which depicts a wide compositional change. Below 1000 m depth, wavelength position of the diagnostic feature shift to >2210 nm with no systematic variation with respect to measured temperature in the well. Compositional variation of illite is interpreted based on earlier studies by Yang et al. (2001) which indicated white mica with <2200 nm as muscovite and those > 2210 nm as phengite. Thus, illite formed in this well is predominantly phengite. In addition, changes in formation temperature observed doesn't have effect on composition variation. This is indicated by nearly constant wavelength positions below 1000 m irrespective of temperature changes.

In OW-916, presence of illite is sporadic and in trace amount. Spectral features occur between 2197-2218 nm as shown in Figure 4-28. At approximately 500 m depth, the wavelength shift between 2197-2214 nm is observed. This indicates difference in compositional change with illite formed at deeper level(> 2200 m) with wavelength shift of > 2210 nm. These variations can be attributed mainly to parental rock composition associated with these two depths i.e. trachyte and basalt at 500 m and trachyte and rhyolites below 2200 m. Compositionally, illite in this well is interpreted as muscovite-phengite mixture at shallow depth and phengite at deeper depth.

In contrast to wells OW-205 and OW-916, diagnostic spectral feature of well OW-917 only occurred above 2210 nm. Absence of illite from the surface to approximately 1700 m despite high temperature and thick

column of trachytic rock unit, could be associated to limited fluid flow in this region. Hence, occurrence of illite between 1700-3000 m is interpreted as due to fluid flow attributed to lithological boundaries of trachyte and basaltic intercalations within this zone(Figure 4-29). Illite formed in this well is interpreted as phengite and its composition could be associated to chemistry of the parental rock material and fluid composition.

Generally, the formation, distribution, composition variation and relative abundances observed in the three wells studied do not show systematic relationship with either measured formation temperature or depth. This study, therefore, cannot associate the observed patterns of illite abundance and composition to either up-flow, out-flow or cooler hydrologic zones to the wells studied. However, further studies in all the three wells is highly recommended to determine factors contributing to composition variation.

Crystallinity variation

This study attempted to investigate the variation of illite crystallinity relative to temperature and depth. Spectral data shows abundant illite in OW 205 occurring in at measured formation temperature of above >160 ^{0}C(Figure 4-27). Conversely, crystallinity value derived from OW-916 and OW-917 were only localized at particular depths and therefore could not be evaluated in relation to downhole depth and temperature. In OW-205, illite-crystallinity value ranges from 1.4-2.3. These values are calculated from the ratio of Al-OH/ H_2O diagnostic feature. For interpretation, interquartile ranges for each depth was used since it is less influenced by the extreme values. As show in in Figure 4-22 A, there is appreciable rise in interquartile ranges in response to measured formation temperature from approximately 700-1350 m depth. However, below this depth, interquartile ranges patterns become inconsistent showing significant increase in variance. This is suggested to be attributed to change in thermal equilibrium associated with cooling reservoir. Conversely, a plot of average crystallinity and temperature relative to depth (Figure 4-22 B) show high crystallinity values in regions associated with temperature reversals. This confirm earlier interpretation indicating hydrothermal minerals formed within this region as being relict. High variance of crystallinity values observed in certain depths could be associated to unstable nature of the well as the system tries to equilibrate.

Formation and composition variation of chlorite

In a geothermal system, chlorite is formed by replacement of the pre-existing ferromagnesian minerals or directly precipitating in cavities, veins or fractures (Raymundo.G.M & Dubois, 1998). It displays a wide range of composition depending on bulk rock and physico-chemical conditions prevalent during its formation (Inoue et al., 2010). Thus, determination of chlorite composition can be used to obtain physico-chemical condition of the geothermal system. Previously, spectral variation of Fe-OH feature in chlorite has been used as a tool to estimate chlorite composition. For instance, Pontual et al., (1997) demonstrated use of wavelength position of either or both Fe-OH and Mg-OH feature to estimate chlorite composition and that variation of the absorption feature is a function of Fe:Mg ratio. Most recently, Simpon and Rae (2018) used Fe-OH feature of chlorite to distinguish Fe-rich chlorite, Fe-Mg chlorite and Mg-rich chlorite. In this case, Mg-rich chlorite occurred between 2240-2249 nm, Fe-Mg chlorite between 2250-2256 nm and Fe-chlorite between 2257-2265 nm wavelength range. In this study, spectral data was used to estimate composition variation in the three geothermal wells studied with an aim to decipher the prevailing sub-surface conditions.

Figure 4-27 shows variations of wavelength position of the Fe-OH feature relative to depth in OW-205. At approximately 700 m depth, diagnostic absorption feature of chlorite occurs between 2246-2256 nm. With depth increase, wavelength shift to between 2256-2265 nm is observed. Therefore, based on wavelength position of the diagnostic feature, chlorite formed near 700 m is interpreted as Fe-Mg chlorite while the one formed below this depth as Fe-rich chlorite. Change in wavelength shift observed in this well shows no systematic pattern in respect to temperature change. In this regard, compositional variation of chlorite in this well is mainly attributed to parental rock materials.

In OW-916 (Figure 4-28), chlorite appears sporadically both in shallow and deeper level. Wavelength position of the diagnostic feature varies between 2255-2260 nm with variation being independent of measured formation temperature. In this well, chlorite is formed on basalts, trachyte and rhyolitic rock units. It is mainly formed in depths where there is close lithological contacts of these rock units. Compositionally, chlorite formed in this well is largely Fe-rich chlorite and its composition could be attributed to both chemistry of parental rock and fluid composition.

As shown in Figure 4-29, chlorite is almost undetectable at shallow depth in this well. Analogous to OW-916, it appears at deeper level in regions dominated by presence of close lithological boundaries associated with trachyte and basalts. Wavelength position of the diagnostic feature varies between 2254-2265 nm. Hence, it is interpreted as Fe-rich chlorite. Most notably, is the absence of chlorite between 800-1400 m depth. This is despite a thick column of trachytic rock and measured formation temperature of $>200^0$ C observed within this region. This phenomenon is attributed to lack of permeability thus hindering smooth flow of hydrothermal fluids within that region.

Generally, composition variation of chlorite resulting from the three wells appears to be controlled mainly by chemistry of the parental rock and fluid composition. Nevertheless, temperature contributions cannot be completely ignored. Largely, there is similarity in the compositional characteristic of chlorite from spectral data derived from the three wells. Therefore, the use of compositional variation of chlorite to interpret wells as either up-flow, out-flow or a cooling reservoir is quite challenging. However, further and detailed study of composition variation in chlorite from Olkaria geothermal system in order to understand the relationship between occurrence, distribution and chemical composition to the hydrology may be beneficial.

In summary, the distribution of hydrothermal minerals and mineral assemblages identified by SWIR hyperspectral imaging technique in this study can essentially be used to interpret up-flow, out-flow and cooling zones in a geothermal system. In addition, the technique was able to estimate relative abundances of common hydrothermal minerals identified and distinguish mineral species found in some mineral groups. Most importantly, is the minimal sample preparation required before analysis and its capability of acquiring a large date set within a short time thus making it ideal for providing a fast solution to drilling challenges. However, some limitations are worth noting. Important hydrothermal minerals such as quartz, plagioclase, adularia, albite, hematite and goethite are not sensitive in SWIR region of the electromagnetic spectrum and therefore were not identified.

6. CONCLUSIONS AND RECOMMENDATIONS

SWIR hyperspectral imaging has proved to be a powerful tool for identifying and characterizing hydrothermal alteration minerals formed in a geothermal system. Acquisition of high spectral resolution images using SWIR camera combined with spectral algorithms from ENVI, HypPy3 and TSG software allows quick identification of spectrally active minerals in SWIR region. Largely, zeolite, smectite, illite, calcite, chlorite, epidote and amphiboles were found to be the most common alteration mineral in the three wells studied. However, their associations in response to temperature and physico-chemical changes resulted in formation of different alteration zoning patterns. Generally, hydrothermal minerals derived from spectral data are in good agreement with those previously identified using conventional methods. No new hydrothermal alteration minerals identified using spectral data in this study. However, unlike in other methods, this technique successfully distinguished smectites(nontronite, montmorillonite) and amphiboles(actinolite, hornblende)occurring in Olkaria geothermal system.

Determination and identification of hydrothermal minerals using mineral maps from hyperspectral images(e.g. Figure 4-16) can be useful for inferring formation temperature and fluid composition during drilling process. Information derived can thus be used to address on-site drilling challenges. However, comprehensive interpretation of up-flow , out-flow and cooling zones can only be determined after well completion to allow comparison of the measured and inferred temperature from hydrothermal alteration minerals(Figure 4-27 to Figure 4-29). There is clear variation in alteration zones formed in each of the three wells with gradual change of low-temperature minerals(mordenite, smectite) to high temperature minerals(amphiboles) as best indicated in the up-flow well OW 916. These variations are mainly attributed to changes in temperature, permeability and chemistry of the parental rocks. Relative abundances calculated from SAM classified images vary from one depth to another and does not show any systematic relationship relative to depth or temperature changes. However, information derived from mineral abundances especially at shallow depths where abundant smectite was identified can practically be applied at drill site to avert the danger of stuck drill pipes.

Compositional variations observed for both illite and chlorite show no trend with respect to depth or temperature. However, small variations observed in both illite and chlorite formed in permeable zones associated with close lithological boundaries, can be used to interpret the main factor controlling hydrothermal mineral formation. In this study, parental rock material and fluid chemistry were interpreted as the main factor determining composition variations. Typically, illite formed in this well tend to have less Al in the dioctahedral structure and thus interpreted as phengite. On the other hand, wavelength position of Fe-OH feature predominantly shows a shift to longer wavelengths in all the three wells suggesting a Fe-rich chlorite. Observed patterns of illite crystallinity values in OW-205 show illite presence as being relict and does not reflect the prevailing temperature conditions.

Based on the results, the following are recommended:

- Future spectroscopy study should involve full range of electromagnetic spectrum in order to target minerals active in VNIR(e.g. goethite, hematite and jarosite), SWIR(e.g. sericite, pyrophyllite, chlorite, calcite, amphiboles) and LWIR(e.g. quartz, plagioclase, adularia, albite) regions of the electromagnetic spectrum.

- For comprehensive hydrothermal alteration zoning, complete scanning of all samples from shallow depths to deeper depth is recommended.

- Detailed study on mineralogical compositon variation and its application in understanding diffenent hdyrologic zone in a geothermal systems is highly recommended.

- Due to difficulties encountered in distinguishing mordenite and wairakite using SWIR spectroscopy, LWIR spectroscopy recommended to study their spectral behavior.

- To understand nature of the formation of hydrothermal minerals using SWIR hyperspectral imaging (e.g. as replacement of primary mineral, vesicles, vugs or fracture fillings) a much higher resolution imaging on selected samples based on alteration mineral distribution patterns is recommended.

LIST OF REFERENCES

Abweny, M. S., van Ruitenbeek, F. J. A., de Smeth, B., Woldai, T., van der Meer, F. D., Cudahy, T., … Thuss, B. (2016). Short-Wavelength Infrared (SWIR) spectroscopy of low-grade metamorphic volcanic rocks of the Pilbara Craton. *Journal of African Earth Sciences*, *117*, 124–134. https://doi.org/10.1016/j.jafrearsci.2016.01.024

Axelsson, G., Arnaldsson, A., Ármannsson, H., Árnason, K., & Einarsson, G. (2013). Updated conceptual model and capacity estimates for the Greater Olkaria Geothermal System, Kenya. In *Workshop on Geothermal Reservoir Engineering*. Stanford, California: Stanford University. Retrieved from https://pangea.stanford.edu/ERE/pdf/IGAstandard/SGW/2013/Axelsson.pdf

Bakker, W. H. (2014). HypPy User Manual graphical user interface. *ITC - University of Twente*. Retrieved from http://www.itc.nl/personal/bakker/hyppy.html

Bish, D. L. (2013). Parallels and distinctions between clay minerals and zeolites. *Developments in Clay Science*, *5*(December 2013), 783–800. https://doi.org/10.1016/B978-0-08-098258-8.00026-2

Bonini, M., Corti, G., Innocenti, F., Manetti, P., Mazzarini, F., Abebe, T., & Pecskay, Z. (2005). Evolution of the Main Ethiopian Rift in the frame of Afar and Kenya rifts propagation. *Tectonics*, *24*(1), 1–21. https://doi.org/10.1097/SLA.0000000000001986

Brindley, G. W. (1955). Identification of clay minerals by X-Ray diffraction analysis. In *Clay and Clay technology* (pp. 119–129). Retrieved from http://www.clays.org/journal/archive/volume 1/1-1-119.pdf

Browne, P. R. L. (1970). Hydrothermal alteration as an aid in investigating geothermal fields. In *Geothermics* (Vol. 2, pp. 564–570). Pisa. https://doi.org/10.1016/0375-6505(70)90057-X

Browne, P. R. L. (1978). Hydrothermal Alteration in Active Geothermal Fields. *Annual Review of Earth and Planetary Sciences*, *6*(1), 229–248. https://doi.org/10.1146/annurev.ea.06.050178.001305

Browne, P. R. L., & Ellis, a J. (1970). The Ohaki-Broadlands hydrothermal area, New Zealand: Minerlogy and related geochemistry. *American Journal of Science*, *269*, 97–131.

Calvin, W. M., & Pace, E. L. (2016). Mapping alteration in geothermal drill core using a field portable spectroradiometer. *Geothermics*, *61*, 12–23. https://doi.org/10.1016/j.geothermics.2016.01.005

Caritat, P. D. E., Hutcheon, I. A. N., & Walshe, J. L. (1993). Chlorite geothermometry: A review, *41*(2), 219–239.

Christidis, G. E. (2012). Zeolite Formation and Deposits. *Handbook of Natural Zeolites*, (July), 19–36. https://doi.org/10.2174/978160805261511201010028

Clark, R. N. (1999). Spectroscopy of rocks and minerals, and principles of spectroscopy. *Remote Sensing for the Earth Sciences: Manual of Remote Sensing*, *3*, 3–58. https://doi.org/10.1111/j.1945-5100.2004.tb00079.x

Clark, R. N., King, T. V. V., Klejwa, M., Swayze, G. A., & Vergo, N. (1990). High spectral resolution reflectance spectroscopy of minerals. *Journal of Geophysical Research*, *95*(B8), 12,653-12,680. https://doi.org/10.1029/JB095iB08p12653

Clarke, Woodhall, A. & D. (1990). *Geological, volcanological and hydrogeological controls on the occurrence of geothermal activity sorrounding Lake Naivasha, Kenya*. Nairobi.

Cumming, W. (2009). Geothermal Resource Conceptual Models Using Surface Exploration Data. In *Thirty-Fourth Workshop on Geothermal Reservoir Engineering*. Stanford, California: Stanford University.

Goetz , F.H. Gregg V.J, B. N. . (1985). Imaging Spectrometry for Earth Remote Sensing Author (s): Alexander F . H . Goetz , Gregg Vane , Jerry E . Solomon and Barrett N . Rock. *Science*, *228*(4704), 1147–1153. Retrieved from https://www.jstor.org/stable/pdf/1694909.pdf?refreqid=excelsior%3A198bebe8896350b87d08216b6a826f6c

Goryniuk, M. C., Rivard, B. A., & Jones, B. (2004). The reflectance spectra of opal-A (0.5-25 μm) from the Taupo Volcanic Zone: Spectra that may identify hydrothermal

systems on planetary surfaces. *Geophysical Research Letters*, *31*(24). https://doi.org/10.1029/2004GL021481
Haldar, S. K., & Tišljar, J. (2014). *Basic Mineralogy*. *Introduction to Mineralogy and Petrology*. https://doi.org/10.1016/B978-0-12-408133-8.00002-X
Hauff, P. (2008). An overview of VIS-NIR-SWIR field spectroscopy as applied to precious metals exploration. *Arvada, Colorado: Spectral International Inc*, (January).
Henley, R. W., & Ellis, A. J. (1983). Geothermal Systems Ancient and Modern : A Geochemical Review, *19*, 1–50. Retrieved from https://doi.org/10.1016/0012-8252(83)90075-2
Hunt, G. R. (1977). Spectral signatures of particulate minerals in the visible and near infrared. *Geophysics*, *42*(3). https://doi.org/10.1190/1.1440721
Hunt, G. R. (1986). Near-infrared (1.3-2.4 pm) spectra of alteration minerals- Potential for use in remote sensing. *Geophysics*, *44*(12).
Inoue, A. (1995). Formation of Clay Minerals in Hydrothermal Environments. In *Origin and Mineralogy of Clays* (pp. 268–329). Berlin, Heidelberg: Springer Link. https://doi.org/10.1007/978-3-662-12648-6_7
Inoue, A., Kurokawa, K., & Hatta, T. (2010). Application of chlorite geothermometry to hydrothermal alteration in toyoha geothermal system, southwestern hokkaido, Japan. *Resource Geology*, *60*(1), 52–70. https://doi.org/10.1111/j.1751-3928.2010.00114.x
J.A.drey, T. A. J. B. . H. P. L. . R. (1999). Alteration mapping in exploration; application of short-wave infrared SWIR spectroscopy. *SEG Newsletter*. Retrieved from https://eurekamag.com/research/029/972/029972329.php
K.Bird, D. (1983). *Calc-silicate mineralization in active geothermal systems*. Stanford, California.
Khodayar, M., Björnsson, S., Einarsson, P., & Franzson, H. (2010). Effect of tectonics and earthquakes on geothermal activity near plate boundaries: A case study from South Iceland. *Geothermics*, *39*(3), 207–219. https://doi.org/10.1016/j.geothermics.2010.06.003
Kokaly, R. F. (2018). sciencebase@usgs.gov.
Kruse, F. A. (1996). Identification and mapping of minerals in drill core using hyperspectral image analysis of infrared reflectance spectra. *International Journal of Remote Sensing*, *17*(9). https://doi.org/10.1080/01431169608948728
Kruse, F. A., Lefkoff, A. B., Boardman, J. W., Heidebrecht, K. B., Shapiro, A. T., Barloon, P. J., & Goetz, A. F. H. (1993). The spectral Image Processing System (SIPS)—Interactive Visualization and Analysis of Imaging Spectrometer Data. *Remote Sensing of Environment*, *44*(2–3), 145–163. https://doi.org/10.1016/0034-4257(93)90013-N
Lagat, J. (2014). Hydrothermal alteration mineralogy in geothermal fields with case examples from Olkaria domes geothermal field, Kenya. In *Short Course IX on Surface Exploration for Geothermal Resources*. Naivasha: UNU-GTP,Kengen and GDC. Retrieved from http://www.os.is/gogn/unu-gtp-sc/UNU-GTP-SC-05-10.pdf
Lagat, J., Arnorsson, S., & Franzson, H. (2005). Geology, hydrothermal alteration and fluid inclusion studies of Olkaria domes geothermal field , Kenya. In *Proceedings, World Geothermal Congress 2005, Antalya, Turkey* (pp. 24–29). Antalya,Turkey. Retrieved from https://www.geothermal-energy.org/pdf/IGAstandard/WGC/2005/0649.pdf
Littlefield, E. F., & Calvin, W. M. (2014). Geothermal exploration using imaging spectrometer data over Fish Lake Valley, Nevada. *Remote Sensing of Environment*, *140*, 509–518. https://doi.org/10.1016/j.rse.2013.09.007
Lund, J. W. (2008). Characteristics, Development and Utilization of Geothermal Resources-a Nordic perspective. *Geo-Heat Center Quarterly Bulletin*, *31*(1), 1–9. https://doi.org/10.1007/978-3-540-75997-3_13
Massonne.J, & Schreyer, W. (1987). Phengite geobarometry based on the limiting assemblage with K-feldspar, phlogopite, and quartz. *Contributions to Mineralogy and Petrology*, *96*(2), 212–224. https://doi.org/10.1007/BF00375235
Mathieu, M., Roy, R., Launeau, P., Cathelineau, M., & Quirt, D. (2017). Alteration mapping on drill cores using a HySpex SWIR-320m hyperspectral camera:

Application to the exploration of an unconformity-related uranium deposit (Saskatchewan, Canada). *Journal of Geochemical Exploration*, *172*, 71–88. https://doi.org/10.1016/j.gexplo.2016.09.008
Milicich, S. D., Chambefort, I., & Bignall, G. (2015). Hydrothermal Alteration : Separating Fact from Hyperbole. Melbourne,Australia: Researchgate. Retrieved from https://www.researchgate.net/publication/275964769_Hydrothermal_Alteration_Separating_Fact_from_Hyperbole
Moeck, I. S. (2014). Catalog of geothermal play types based on geologic controls. *Renewable and Sustainable Energy Reviews*, *37*, 867–882. https://doi.org/10.1016/j.rser.2014.05.032
Mortensen, A. K. (2012). Hydrothermal alteration in geothermal systems. Naivasha,Kenya: United Nations University.
Muchemi, T. M. L. and G. G. (1987). Geology and Hydrothermal Alteration of the North and West exploration wells in Olkaria, Kenya. In *Proceeding 9th NZ Geothermal Workshop* (Vol. 82).
Munyiri, S. K. (2016). *Structural Mapping of Olkaria Domes geothermal field using Geochemical Soil Gas Surveys , Remote Sensing and GIS*. United Nations University.
Musonye, X. (2015). *Sub-Surface Petrochemistry , Stratigraphy and Hydrothermal alteration of the Domes area , Olkaria geothermal filed, Kenya*. United Nations University.
Mwangi, & David. (2016). Use of Hydrothermal Mineralogy and Geological structures in Identifying drill sites in Olkaria Domes geothermal field, Naivasha, Kenya. In *Proceedings, 41st Workshop on Geothermal Reservoir Engineering* (Vol. 1956, pp. 1–13). Stanford, California. Retrieved from https://pangea.stanford.edu/ERE/db/IGAstandard/record_detail.php?id=26556
Ofwona. (2002). *A Reservoir Study of Olkaria East Geothermal System, Kenya*. United Nations University. Retrieved from https://orkustofnun.is/gogn/unu-gtp-report/UNU-GTP-2002-01.pdf
Omenda, P. A. (1998). The geology and structural controls of the Olkaria geothermal system, Kenya. *Geothermics*, *27*(1), 55–74. https://doi.org/10.1016/S0375-6505(97)00028-X
Omenda, P. A. (2010). The geology and geothermal activity of the East African Rift. In *Presented at short course V on Exploration for geothermal resources* (pp. 14–18). Naivasha,Kenya: UNU-GTP,Kengen and GDC.
Otieno, V. O. (2016). *Borehole Geology and sub-surface petrochemistry of the Domes area , Olkaria geothermal field , Kenya , in relation to well OW-922*. United Nations University.
Pontual, S., Merrry, N.,& Gamson, .P. (1997). *GMEX_Booklet1_Spectral Interpretation Field Manual .pdf*. AusSpec International Pty. Ltd.
Pontual, S., Merry, N., & Gamson, P. (2008). GMEX1-Spectral Interpretation Field Manual.pdf. AusSpec International Pty. Ltd.
Pontual, S., Merry, N., & Gamson, P. (1997a). *Epithermal Alteration Systems*. *AusSpec International Pty.* (Vol. Vol 4). AusSpec International Pty. Ltd.
Pontual, S., Merry, N., & Gamson, P. (1997b). Spectral Analysis Guides for Mineral Exploration: Vol 1 - Spectral Interpretation Field Manual. *AusSpec International Pty.* AusSpec International Pty. Ltd.
Rae, A., O'Brien, R, E., & Bignall, G. (2011). The Application of Chlorite Geothermometry to Hydrothermally Altered Rotokawa Andesite, Rotokawa Geothermal Field. In *New Zealand Geothermal Workshop 2011 Proceedings* (p. 8). Auckland, New Zealand.
Rae, S. &. (2018). Short-wave infrared (SWIR) reflectance spectrometric characterisation of clays from geothermal systems of the Taupō Volcanic Zone, New Zealand. *Geothermics*, *73*(February), 74–90. https://doi.org/10.1016/j.geothermics.2018.01.006
Rashmi, S., Addamani, S., Ravikiran, S., Rashmi, S., Addamani, S., & Ravikiran, S. (2014). Spectral Angle Mapper Algorithm for Remote Sensing Image Classification. *International Journal of Innovative Science, Engineering & Technology*, *1*(4), 201–205. https://doi.org/10.1109/CISP.2013.6745277
Raymundo.G.M, & Dubois, M. (1998). Chemical variations in chlorite at the Los Humeros

geothermal system,Mexico, *46*(6), 615–628. Retrieved from http://www.clays.org/journal/archive/volume 46/46-6-615.pdf
Reyes,A.G., M. C. B. . (1988). Petrological Identification of Multiple Heat Sources in Bacon-Manit0 Geothermal System, Tiie, 713–717.
Reyes, A. G. (1990). Petrology of Philipines geothermal systems and the application of alteratino mineralogy to their assessement. *Journal of Volcanology and Geothermal Research*, *43*, 279–309. https://doi.org/10.1016/0377-0273(90)90057-M
Reyes, A. G. (1998). *Petrology and mineral alteration in hydrothermal systems: From diagenesis to volcanic catastrophes*. United Nations University.
Ronoh, I. (2015). Appraising a Geothermal field using Hydrothermal alteration mineralogy : a Case study of the East of Olkaria Domes geothermal field ; Olkaria , Kenya. In *Proceedings World Geothermal congress* (pp. 19–25). Melbourne,Australia.
Ruitenbeek, F. J. A. Van, Bakker, W. H., Werff, H. M. A. Van Der, Zegers, T. E., Oosthoek, J. H. P., Omer, Z. A., … Meer, F. D. Van Der. (2014). Mapping the wavelength position of deepest absorption features to explore mineral diversity in hyperspectral images. *Planetary and Space Science*, *101*, 108–117. https://doi.org/10.1016/j.pss.2014.06.009
Shackleton. (1996). The final collision zone between East and West Gondwana: where is it? *Environmental Research*, *23*(3).
Shahriari, H., Ranjbar, H., Honarmand, M., & Carranza, E. J. M. (2014). Selection of less biased threshold angles for SAM classification using the real value-area fractal technique. *Resource Geology*, *64*(4), 301–315. https://doi.org/10.1111/rge.12042
Simmons, C. . (1993). Towards a Unified Theory on Calcite Formation in Boiling Geothermal Systems (pp. 145–148). Retrieved from https://www.geothermal-energy.org/pdf/IGAstandard/NZGW/1993/Simmons.pdf
Simmons, S. F., & Christenson, B. W. (1994). Origins of calcite in a boiling geothermal system. *American Journal of Science*, *294*(3), 361–400. https://doi.org/10.2475/ajs.294.3.361
Simpson, M.P , Bignall, G., Rae, A. J., Christie, A. B., & Chambefort, I. (2015). Mapping of hydrothermal minerals in New Zealand geothermal fields using reflectance spectroscopy (VNIR-SWIR) and application to mineral deposit exploration. Hong Kong: GNS Science.
Simpson & Christie. (2016). *Exploration of New Zealand mineral deposits and geothermal systems using X-ray diffraction (XRD) and reflectance spectrometry (SWIR): A comparison of techniques*. https://doi.org/10.21420/G2NP4D
Skord, J., Cashman, P. H., Coolbaugh, M., & Hinz, N. (2011). Mapping Hydrothermal Upwelling and Outflow Zones : Preliminary Results from Two-Meter Temperature Data and Geologic Analysis at Lee Allen Springs and Salt Wells Basin, *35*. Retrieved from http://www.atlasgeoinc.com/wp-content/uploads/2012/Publications/Nevada/GRC2011-Coolbaugh-2m-T-Optimized.pdf
Spider.R, K.Bird, D., & Abigail, &. (2004). Epidotes - Google Books. Retrieved December 27, 2018, from https://books.google.nl/books?id=KbB6DwAAQBAJ&pg=PA236&lpg=PA236&dq=epidote+formation+in+a+geothermal+environment&source=bl&ots=UwxURAuiSz&sig=dWKa1fPXus_lR40aBJVon9ztq5s&hl=en&sa=X&ved=2ahUKEwjoh4i7yr_fAhVOYVAKHXZOCsoQ6AEwCnoECAMQAQ#v=onepage&q=epidote%252
Stefan. (1989). Depositon of Calcium Carbonate minerals from geothermal waters-Theoretical considerations.pdf. *Geothermics*, *18*(1), 33–39.
Tardy, Y., Duplay, J., & Fritz, B. (1987). *Stability fields of smectites and illites as a function of temperature and chemical composition*.
Taylor, G. R. (2000). Mineral and lithology mapping of drill core pulps using visible and infrared spectrometry. *Natural Resources Research*, *9*(4), 257–268. https://doi.org/10.1023/A:1011501125239
Thomas, M., & Walter, M. R. (2002). Application of Hyperspectral Infrared Analysis of Hydrothermal Alteration on Earth and Mars. *Astrobiology*, *2*(3).
van der Meer, F., Kopačková, V., Koucká, L., van der Werff, H. M. A., van Ruitenbeek, F.

J. A., & Bakker, W. H. (2018). Wavelength feature mapping as a proxy to mineral chemistry for investigating geologic systems: An example from the Rodalquilar epithermal system. *International Journal of Applied Earth Observation and Geoinformation*, *64*, 237–248. https://doi.org/10.1016/J.JAG.2017.09.008

Vidal, J., Patrier, P., Genter, A., Beaufort, D., Dezayes, C., Glaas, C., … Sanjuan, B. (2018). Clay minerals related to the circulation of geothermal fl uids in boreholes at Rittershoffen (Alsace , France). *Journal of Volcanology and Geothermal Research*, *349*, 192–204. https://doi.org/10.1016/j.jvolgeores.2017.10.019

Yang, K., Browne, P. R. L., Huntington, J. F., & Walshe, J. L. (2001). Characterising the hydrothermal alteration of the Broadlands-Ohaaki geothermal system, New Zealand, using short-wave infrared spectroscopy. *Journal of Volcanology and Geothermal Research*, *106*(1–2), 53–65. https://doi.org/10.1016/S0377-0273(00)00264-X

Yang, K., Huntington, J. F., Browne, P. R. L., & Ma, C. (2000). An infrared spectral reflectance study of hydrothermal alteration minerals from the Te Mihi sector of the Wairakei geothermal system, New Zealand. *Geothermics*, *29*(3), 377–392. https://doi.org/10.1016/S0375-6505(00)00004-3

Yang, K., Huntington, J. F., Gemmell, J. B., & Scott, K. M. (2011). Variations in composition and abundance of white mica in the hydrothermal alteration system at Hellyer , Tasmania , as revealed by infrared re fl ectance spectroscopy. *Journal of Geochemical Exploration*, *108*(2), 143–156. https://doi.org/10.1016/j.gexplo.2011.01.001

Zaini, N., van der Meer, F., & van der Werff, H. (2014). Determination of carbonate rock chemistry using laboratory-based hyperspectral imagery. *Remote Sensing*, *6*(5), 4149–4172. https://doi.org/10.3390/rs6054149

7. APPENDICES

Appendix 1: SAM classified images.

OW-205 728-730 m

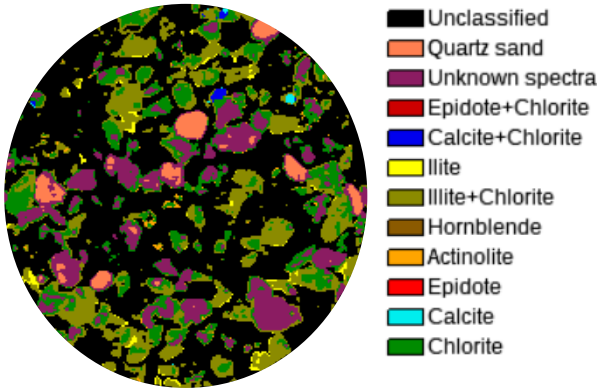

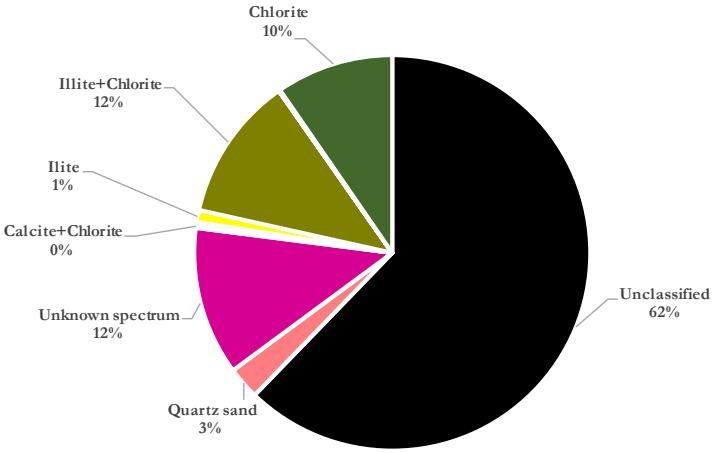

OW-916 1288-1290 m

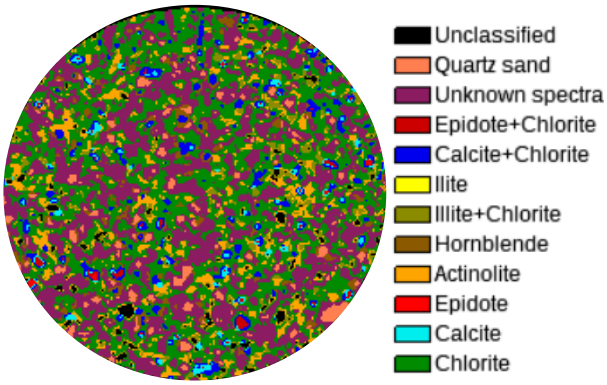

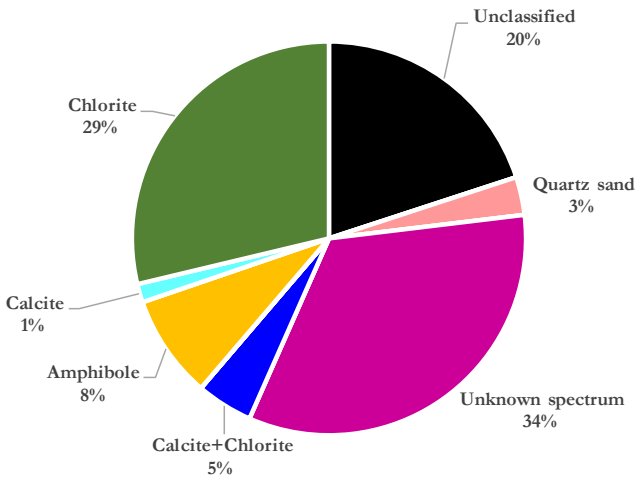

Appendix II: Samples XRD diffractograms

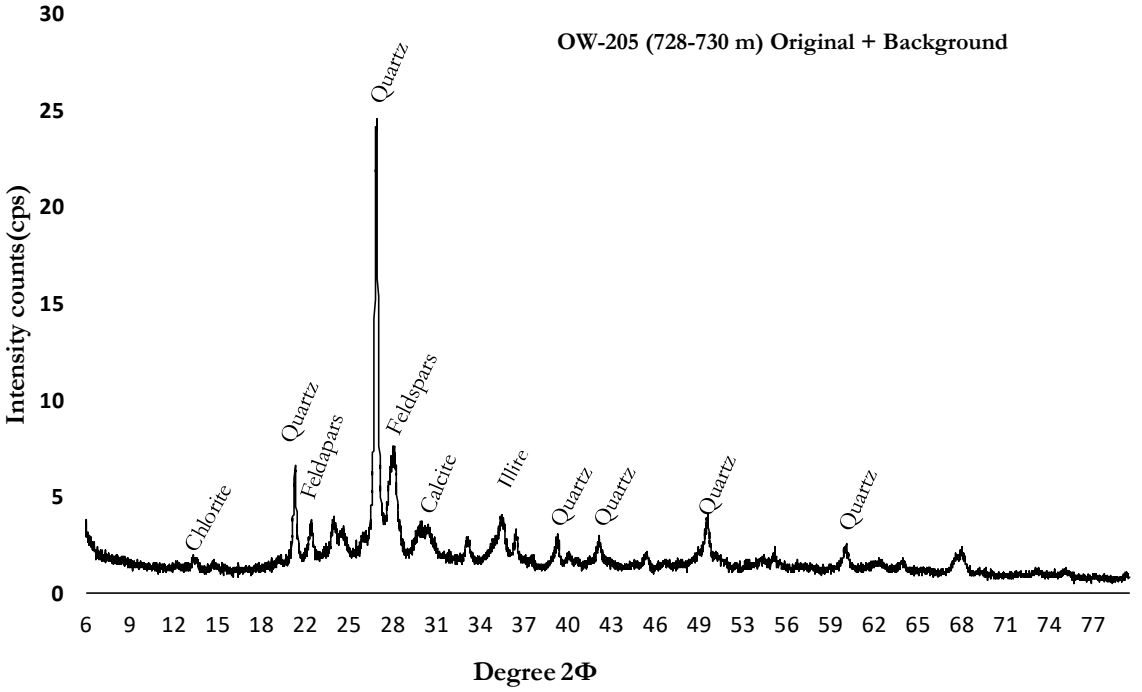

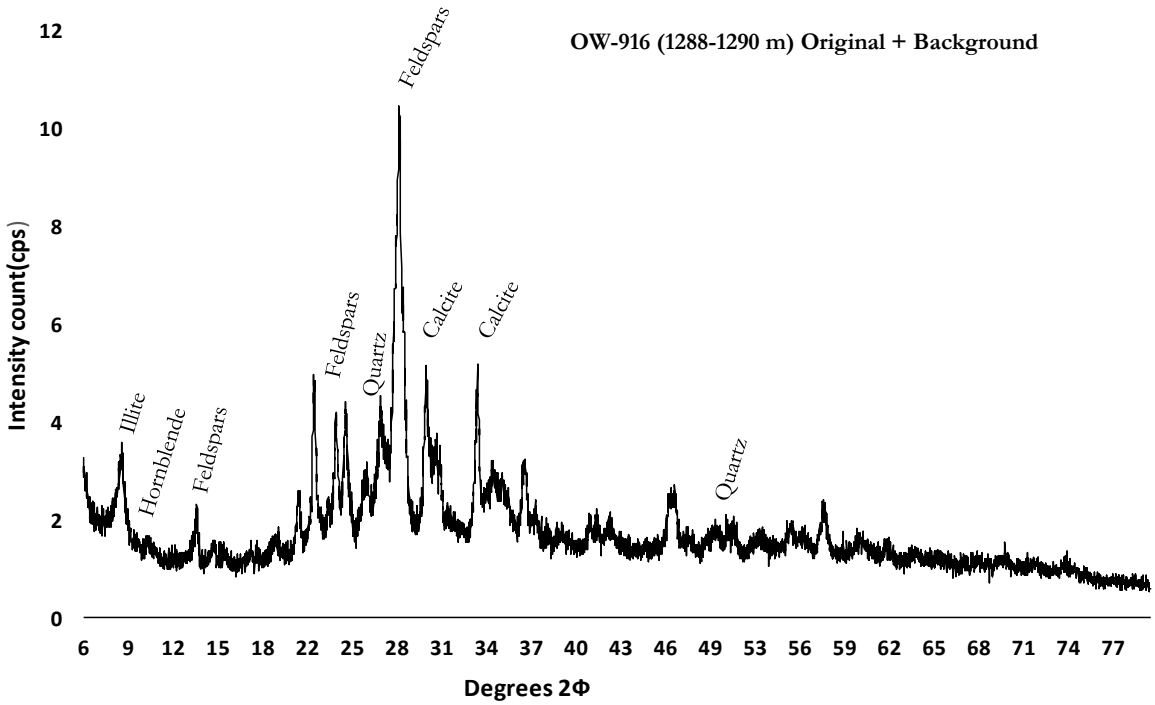

Appendix III: Relative abundances OW 205

OW205 Samlple #	Unclassified	Epidote+ Chlorite	Calcite	Calcite+Chlorite	Zeolite	Illite	Illite+Chlorite	Hornblende	Actinolite	Epidote	Chlorite
512-514	68.00	0.00	0.00	0.54	0.20	0.14	3.07	0.00	0.00	0.00	12.70
568-570	57.08	0.00	0.00	0.00	2.02	0.24	2.27	0.00	0.00	0.00	7.10
726-728	61.53	0.00	0.30	0.18	0.13	0.34	3.30	0.00	0.00	0.00	8.10
728-730	53.30	0.00	0.10	0.20	0.29	0.97	11.81	0.00	0.00	0.00	9.60
842-846	69.07	0.00	0.24	0.52	0.00	0.13	3.02	0.00	0.00	0.00	12.42
854-856	44.62	0.00	0.01	0.68	0.00	0.17	8.37	0.00	0.00	0.00	24.19
872-874	21.04	0.00	0.02	0.23	0.00	0.25	5.93	0.00	0.00	0.00	30.89
902-904	12.13	0.00	0.00	0.10	0.00	0.27	1.57	0.00	0.00	0.00	30.70
938-942	37.23	0.00	0.00	0.07	0.00	0.03	0.49	0.00	0.00	0.00	17.70
978-982	27.30	0.00	0.00	0.01	0.00	0.16	1.37	0.00	0.00	0.00	7.45
1012-1014	33.00	0.00	0.00	0.00	0.48	0.42	2.44	0.00	0.00	0.00	16.30
1060-1062	41.21	0.01	0.27	0.83	0.00	0.14	5.25	0.06	0.00	0.01	21.53
1120-1122	39.88	0.00	0.04	0.40	0.00	0.00	0.31	0.00	0.00	0.00	15.27
1122-1124	40.72	0.00	0.02	0.00	0.00	0.03	0.22	0.00	0.00	0.00	17.19
1154-1156	31.12	0.00	1.64	0.20	0.00	0.03	9.05	0.07	1.42	0.01	22.53
1300-1304	53.90	0.00	0.02	0.08	0.00	0.00	0.65	0.02	0.09	0.01	22.76
1344-1348	72.27	0.00	0.14	0.15	0.00	0.07	9.66	0.01	0.04	0.02	12.25
1384-1388	82.16	0.45	1.99	0.87	0.00	0.03	1.68	0.07	0.47	0.27	7.58
1440-1442	67.84	0.30	3.90	1.58	0.00	0.85	6.83	0.09	0.35	0.36	13.28
1538-1542	48.36	0.01	0.07	0.05	0.00	0.02	3.71	0.02	3.36	0.00	32.24
1594-1598	43.88	0.02	0.21	0.55	0.00	0.03	0.15	0.02	0.09	0.01	26.31
1646-1650	52.68	0.00	0.04	0.04	0.00	1.36	22.69	0.00	0.00	0.00	17.15
1672-1676	50.56	0.02	0.31	0.24	0.00	0.24	1.88	0.07	0.09	0.05	23.98
1684-1688	41.04	0.06	0.66	0.44	0.00	0.14	0.72	0.08	0.05	0.09	25.10
1700-1704	77.70	0.00	0.04	0.05	0.00	0.06	0.37	0.00	0.00	0.00	20.18
1838-1840	83.84	0.00	0.03	0.08	0.00	0.01	0.18	0.49	0.01	0.00	2.82
1964-1966	57.18	0.00	0.04	0.11	0.00	2.44	12.10	0.07	0.00	0.00	17.87
2066-2070	39.63	0.45	9.00	5.00	0.00	0.14	15.00	1.00	14.00	0.22	20.00
2070-2074	42.84	0.07	1.46	5.73	0.00	0.52	11.54	0.09	0.00	0.01	18.55
2168-2172	63.40	0.01	0.10	0.31	0.00	0.33	1.08	0.19	0.01	0.01	9.32
2172-2174	51.68	0.00	0.29	0.50	0.00	0.30	2.11	0.10	0.01	0.03	20.51
2376-2380	57.62	0.03	1.75	0.84	0.00	0.83	4.83	0.03	3.15	0.11	18.58
2424-2426	48.12	0.48	8.36	4.66	0.00	0.14	3.37	0.52	8.90	0.23	18.47
2514-2518	73.33	0.02	1.38	0.43	0.00	0.43	2.38	0.14	1.31	0.06	12.96
2616-2618	51.12	0.07	1.17	0.66	0.00	0.00	3.27	0.39	14.33	0.05	16.85
2640-2642	60.33	0.60	4.29	2.99	0.00	0.10	1.00	1.09	2.87	0.20	15.72
2658-2660	47.72	0.04	0.56	1.13	0.00	0.08	1.98	0.29	4.06	0.01	25.90
2678-2680	53.94	0.01	0.21	0.48	0.00	0.10	0.96	0.08	1.45	0.00	18.91
2728-2730	49.70	0.03	0.26	0.33	0.00	0.05	0.69	1.73	6.29	0.02	14.46
2730-2732	51.85	0.00	0.03	0.14	0.00	0.06	0.19	1.64	0.21	0.01	4.34
2798-2800	76.04	0.17	1.87	1.97	0.00	0.07	1.11	0.14	0.44	0.04	12.17
2846-2848	52.41	0.07	1.25	3.92	0.00	0.02	0.39	3.15	1.82	0.00	20.96
2864-2866	76.88	0.01	18.00	0.13	0.00	0.10	1.32	0.23	0.36	0.00	15.21
2914-2916	77.74	0.00	0.14	0.21	0.00	0.04	0.33	0.32	0.19	0.00	13.00
2926-2930	85.70	0.00	0.01	0.01	0.00	0.01	0.00	0.00	0.04	0.00	9.28
2940-2942	67.06	0.60	0.26	0.02	0.00	0.07	1.19	0.27	0.84	0.03	16.38

Average	**54.26**	**0.08**	**1.31**	**0.82**	**0.07**	**0.26**	**3.74**	**0.27**	**1.44**	**0.04**	**16.89**

Appendix IV: Relative abundances OW 916

OW916 Sample #	Unclassified	Zeolite	Montimorillonite	Nontronite	Epidote+Chlorite	Calcite	Calcite+Chlorite	Illite	Illite+Chlorite	Hornblende	Actinolite	Epidote	Chlorite
28-30	10.92	8.07	32.79	28.14	0.00	0.00	0.00	0.00	0.00	0.00	0.00	0.00	0.00
50-52	13.85	30.14	0.05	36.62	0.00	0.00	0.00	0.00	0.00	0.00	0.00	0.00	0.00
296-298	28.53	8.11	6.58	20.75	0.00	0.00	0.00	0.00	0.00	0.00	0.00	0.00	0.00
366-368	79.61	1.01	0.13	7.71	0.00	0.00	0.00	0.00	0.00	0.00	0.00	0.00	0.00
376-378	38.51	0.02	0.06	7.44	0.00	0.00	0.00	0.00	0.00	0.00	0.00	0.00	0.00
380-382	46.33	0.08	0.06	13.33	0.00	0.00	0.00	0.00	0.00	0.00	0.00	0.00	0.00
442-444	38.77	0.08	0.20	11.21	0.00	0.01	0.00	0.01	0.00	0.00	0.00	0.00	0.00
448-450	40.92	1.00	0.00	2.30	0.00	0.00	0.00	0.06	0.00	0.00	0.00	0.00	0.17
478-480	52.88	0.00	0.00	0.00	0.00	0.00	0.00	0.14	0.00	0.00	0.00	0.00	0.23
498-500	2.82	0.00	0.00	0.00	0.00	1.00	0.00	3.00	32.00	0.00	0.00	0.00	56.00
778-780	35.69	0.00	0.00	0.00	0.00	0.00	0.00	0.00	0.00	0.00	0.00	0.00	0.00
956-958	63.66	1.66	0.00	0.00	0.00	0.00	0.00	0.00	0.00	0.00	0.00	0.00	0.03
978-980	54.43	0.10	0.00	2.16	0.00	0.00	0.00	0.00	0.00	0.00	0.00	0.00	0.00
1018-1020	73.28	0.00	0.00	1.33	0.00	0.00	0.00	0.00	0.00	0.00	0.00	0.00	4.57
1096-1098	82.50	0.00	0.00	0.00	0.00	0.64	0.00	0.90	0.01	0.00	0.00	0.00	1.48
1164-1166	71.18	0.00	0.00	0.00	0.00	0.00	0.00	0.00	0.00	0.00	0.00	0.00	0.02
1172-1174	85.06	0.00	0.00	0.00	0.00	0.00	0.00	0.00	0.00	0.00	0.00	0.00	0.00
1226-1228	75.20	0.00	0.00	0.00	0.00	0.00	0.00	0.00	0.00	0.00	0.00	0.00	0.00
1288-1290	39.51	0.00	0.00	0.00	0.53	1.51	4.64	0.01	0.23	3.77	4.74	0.08	29.90
1292-1294	66.32	0.00	0.00	0.00	0.09	0.62	0.65	0.00	1.23	0.17	3.16	0.04	16.76
1318-1320	37.96	0.00	0.00	0.00	0.05	3.00	0.98	0.01	26.32	0.09	5.37	0.44	16.22
1338-1340	79.72	0.00	0.00	0.00	0.03	0.06	0.10	0.00	3.55	0.47	1.37	0.00	6.23
1354-1356	48.17	0.00	0.00	0.00	0.02	0.07	0.14	0.00	15.09	0.18	4.61	0.02	3.08
1690-1692	90.53	0.00	0.00	0.00	0.00	0.00	0.00	0.00	0.00	0.20	0.11	0.00	0.00
1886-1888	53.63	0.00	0.00	0.00	0.03	0.00	0.00	0.00	1.78	0.08	0.72	0.00	0.00
1888-1890	60.35	0.00	0.00	0.00	0.00	0.00	0.00	0.00	0.00	0.00	0.67	0.00	0.00
2218-2220	73.80	0.00	0.00	0.00	0.00	0.00	0.00	0.66	1.46	0.16	0.09	0.00	0.34
2226-2228	67.02	0.00	0.00	0.00	0.00	0.00	0.00	0.00	0.00	0.00	0.02	0.00	0.00
2310-2312	53.73	0.00	0.00	0.00	0.00	0.00	0.00	0.00	0.00	0.04	0.02	0.00	0.00
2410-2412	74.58	0.00	0.00	0.00	0.00	0.00	0.00	0.00	0.00	0.00	0.00	0.00	0.71
2488-2490	93.64	0.00	0.00	0.00	0.03	0.00	0.16	0.01	0.04	0.44	0.00	0.00	0.31
2490-2492	91.62	0.00	0.00	0.00	0.02	0.00	0.52	0.00	0.04	3.23	0.00	0.00	0.36
2668-2670	95.57	0.00	0.00	0.00	0.00	0.00	0.00	0.00	0.00	0.12	0.00	0.00	0.00
2724-2726	96.58	0.00	0.00	0.00	0.00	0.00	0.00	0.00	0.00	0.43	0.00	0.00	0.00
2820-2822	95.21	0.00	0.00	0.00	0.00	0.00	0.01	0.09	0.00	0.24	0.01	0.01	1.86
2870-2872	90.58	0.00	0.00	0.00	0.00	0.00	0.00	0.00	0.03	0.29	0.00	0.00	0.15
2824-2826	92.62	0.00	0.00	0.00	0.00	0.00	0.05	0.00	0.04	0.10	0.00	0.00	0.00
2968-2970	94.29	0.00	0.00	0.00	0.00	0.00	0.00	0.03	0.09	0.27	0.00	0.00	0.00
2990-2992	85.79	0.00	0.00	0.00	0.00	0.00	0.00	0.05	0.11	0.10	0.00	0.00	0.00
Average	**63.47**	**1.29**	**1.02**	**3.36**	**0.02**	**0.18**	**0.19**	**0.13**	**2.10**	**0.27**	**0.54**	**0.02**	**3.55**

Appendix V: Relative abundances OW 917

OW917 Sample #	Unclassified	Zeolite	Nontronite	Epidote+Chlorite	Calcite	Calcite+Chlorite	Illite	Illite+Chlorite	Hornblende	Actinolite	Epidote	Chlorite
50-52	59.27	15.98	14.33	0.00	0.00	0.00	0.00	0.00	0.00	0.00	0.00	0.00
140-142	89.75	0.51	1.09	0.00	0.00	0.00	0.00	0.00	0.00	0.00	0.00	0.00
190-192	78.46	0.68	12.65	0.00	0.00	0.00	0.00	0.00	0.00	0.00	0.00	0.00
220-222	54.97	13.74	13.38	0.00	0.00	0.00	0.00	0.00	0.00	0.00	0.00	0.00
282-284	46.59	21.88	12.40	0.00	0.00	0.00	0.00	0.00	0.00	0.00	0.00	0.00
308-310	73.57	6.81	7.32	0.00	0.00	0.00	0.00	0.00	0.00	0.00	0.00	0.00
330-332	78.20	0.21	2.41	0.00	0.00	0.00	0.00	0.00	0.00	0.00	0.00	0.00
338-340	93.40	0.29	2.13	0.00	0.00	0.00	0.00	0.00	0.00	0.00	0.00	0.00
364-366	96.48	0.47	0.34	0.00	0.00	0.00	0.00	0.00	0.00	0.00	0.00	0.00
426-428	87.38	0.00	8.16	0.00	0.00	0.00	0.00	0.00	0.00	0.00	0.00	0.00
430-432	77.60	0.00	11.60	0.00	0.00	0.00	0.00	0.00	0.00	0.00	0.00	0.00
470-472	82.24	0.00	3.72	0.00	0.00	0.00	0.00	0.00	0.00	0.00	0.00	3.69
480-482	75.71	0.00	7.31	0.00	0.00	0.00	0.00	0.00	0.00	0.00	0.00	3.19
536-538	84.14	0.00	4.74	0.00	0.00	0.00	0.00	0.00	0.00	0.00	0.00	0.93
580-582	67.48	0.00	14.64	0.00	0.10	0.00	0.00	0.00	0.70	0.10	0.00	3.10
626-628	68.50	0.00	15.20	0.00	0.00	0.00	0.00	0.00	0.80	0.01	0.00	0.00
650-652	88.73	0.00	1.94	0.00	0.00	0.00	0.00	0.00	0.03	0.00	0.00	0.00
772-774	73.21	0.00	1.34	0.00	0.00	0.00	0.00	0.00	0.00	0.00	0.00	0.00
774-776	66.34	0.00	0.00	0.00	0.00	0.00	0.00	0.00	0.00	0.00	0.00	0.00
794-796	77.65	0.00	0.00	0.00	0.03	0.00	0.00	0.00	0.00	0.00	0.00	0.00
800-802	81.14	0.00	2.30	0.00	0.01	0.09	0.00	0.00	0.00	0.06	0.00	0.00
838-840	87.13	0.00	0.00	0.00	0.00	0.00	0.00	0.00	0.00	0.00	0.00	0.00
870-872	84.28	0.00	0.00	0.00	0.01	0.00	0.00	0.00	0.00	0.00	0.00	0.00
930-934	81.38	0.00	0.00	0.00	0.01	0.00	0.00	0.00	0.00	0.00	0.00	0.00
1018-1022	86.25	0.00	0.00	0.00	0.00	0.00	0.00	0.00	0.01	0.00	0.00	0.00
1130-1132	91.68	0.00	0.00	0.00	0.00	0.00	0.00	0.00	0.00	0.00	0.00	0.00
1440-1442	93.55	0.00	0.00	0.00	0.00	0.00	0.00	0.00	0.00	0.00	0.00	0.00
1490-1492	90.69	0.00	0.00	0.00	0.03	0.00	0.00	0.00	0.00	0.00	0.00	0.00
1520-1524	76.65	0.00	0.00	0.00	0.00	0.00	0.00	0.00	0.37	0.01	0.00	0.00
1690-1692	91.67	0.00	0.00	0.00	0.00	0.00	0.00	0.00	0.00	0.00	0.00	0.00
1746-1748	89.22	0.00	0.00	0.00	0.00	0.00	0.00	0.00	0.00	0.00	0.00	0.00
1778-1782	88.16	0.00	0.00	0.00	0.04	0.00	0.11	0.43	0.00	0.00	0.00	3.22
1850-1852	80.78	0.00	0.00	0.00	0.03	0.08	0.00	0.09	0.01	0.03	0.00	11.93
1890-1894	82.09	0.00	0.00	0.00	0.00	0.00	0.00	0.10	0.02	0.01	0.00	6.78
1920-1922	77.03	0.00	0.00	0.00	0.05	0.00	0.00	0.00	0.00	0.00	0.00	4.30
1956-1960	81.15	0.00	0.00	0.00	0.00	0.08	0.35	4.89	0.07	0.00	0.00	8.16
2040-2042	74.10	0.00	0.00	0.00	0.02	0.01	0.08	0.49	0.00	0.00	0.00	12.81
2112-2116	85.10	0.00	0.00	0.00	0.01	0.17	0.24	1.47	0.00	0.00	0.00	8.51
2138-2140	82.69	0.00	0.00	0.00	0.00	0.00	0.00	0.26	0.01	0.00	0.00	7.38
2150-2154	77.48	0.00	0.00	0.00	0.00	0.00	0.00	0.05	0.00	0.00	0.00	14.19

2180-2182	80.70	0.00	0.00	0.00	0.00	0.01	0.01	0.17	0.01	0.00	0.00	9.53
2208-2212	81.08	0.00	0.00	0.00	0.09	0.06	0.55	1.44	0.00	0.04	0.00	8.35
2234-2236	89.59	0.00	0.00	0.00	0.00	0.02	0.08	0.55	0.00	0.00	0.00	5.60
2380-2382	73.42	0.00	0.00	0.00	0.00	0.00	0.10	1.45	0.00	0.00	0.00	0.00
2480-2482	84.92	0.00	0.00	0.00	0.00	0.09	0.00	0.13	0.08	0.02	0.00	5.42
2530-2532	83.22	0.00	0.00	0.00	0.00	0.00	0.11	0.11	0.92	0.00	0.00	3.17
2600-2602	75.88	0.00	0.00	0.00	0.00	0.00	0.01	0.09	0.00	0.00	0.00	7.50
2718-2722	81.29	0.00	0.00	0.00	0.00	0.02	0.00	0.09	0.00	0.00	0.00	0.00
2832-2834	86.39	0.00	0.00	0.00	0.00	0.02	0.01	0.21	0.00	0.00	0.00	4.30
2864-2866	90.74	0.00	0.00	0.00	0.00	0.01	0.00	0.00	0.00	0.00	0.00	0.00
2938-2940	90.79	0.00	0.00	0.00	0.00	0.02	0.00	0.00	0.00	0.00	0.00	2.03
2984-2986	87.04	0.00	0.00	0.00	0.00	0.00	0.00	0.06	0.00	0.00	0.00	5.30
Average	**80.90**	**1.16**	**2.63**	**0.00**	**0.01**	**0.01**	**0.03**	**0.23**	**0.06**	**0.01**	**0.00**	**2.68**

Appendix VI: Al-OH minimum absorption feature position in nm

Hole ID	Depth	Illite1	Illite2	Illite3
OW205	514.0	2222.0		
OW205	570.0	2219.0		
OW205	728.0	2218.0		
OW205	730.0	2218.0		
OW205	846.0	2209.0		
OW205	856.0	2221.0	2216.0	
OW205	874.0	2199.0	2221.0	
OW205	904.0	2220.0		
OW205	942.0	2217.0	2199.0	
OW205	982.0	2212.0		
OW205	1014.0	2201.0	2220.0	2217.0
OW205	1062.0	2213.0	2217.0	
OW205	1124.0	2215.0		
OW205	1348.0	2218.0		
OW205	1388.0	2218.0	2223.0	
OW205	1442.0	2221.0		
OW205	1542.0	2212.0		
OW205	1598.0	2219.0		
OW205	1650.0	2219.0	2216.0	
OW205	1676.0	2214.0		
OW205	1688.0	2223.0		
OW205	1704.0	2219.0		
OW205	1840.0	2218.0		
OW205	1966.0	2222.0		
OW205	2070.0	2218.0	2212.0	2215.0
OW205	2074.0	2215.0		
OW205	2172.0	2216.0	2223.0	
OW205	2174.0	2218.0		
OW205	2380.0	2215.0		
OW205	2426.0	2219.0		
OW205	2518.0	2216.0		
OW205	2618.0	2221.0		
OW205	2642.0	2224.0		
OW205	2660.0	2216.0		
OW205	2680.0	2216.0		
OW205	2732.0	2213.0		
OW205	2866.0	2208.0		
OW205	2942.0	2222.0		
OW916	30.0			
OW916	52.0			
OW916	298.0			
OW916	368.0			
OW916	378.0			
OW916	382.0			
OW916	444.0			
OW916	450.0	2198.0		

Hole ID	Depth	Illite1	Illite2
OW916	480.0	2202.0	2212.0
OW916	500.0	2208.0	
OW916	780.0		
OW916	958.0		
OW916	980.0		
OW916	1020.0	2203.0	
OW916	1098.0		
OW916	1166.0		
OW916	1174.0		
OW916	1228.0		
OW916	1236.0		
OW916	1290.0		
OW916	1294.0		
OW916	1320.0		
OW916	1340.0		
OW916	1356.0		
OW916	1692.0		
OW916	1888.0		
OW916	1890.0		
OW916	2220.0		
OW916	2228.0	2214.0	
OW916	2312.0		
OW916	2412.0		
OW916	2490.0		
OW916	2492.0	2217.0	
OW916	2670.0		
OW916	2726.0		
OW916	2822.0		
OW916	2826.0	2214.0	
OW916	2872.0	2214.0	
OW916	2970.0	2214.0	
OW916	2992.0	2217.0	
OW917	192.0	2222.0	
OW917	1782.0	2217.0	
OW917	1960.0	2218.0	2220.0
OW917	2042.0	2222.0	
OW917	2116.0	2219.0	
OW917	2140.0	2220.0	
OW917	2182.0	2223.0	
OW917	2212.0	2220.0	
OW917	2236.0	2217.0	
OW917	2382.0	2218.0	2216.0
OW917	2532.0	2221.0	
OW917	2602.0	2215.0	
OW917	2834.0	2213.0	
OW917	2940.0	2217.0	

Appendix VII: F-OH Minimum absorption feature position in nm

Hole	Depth	FeOH_1	FeOH_2
OW205	514.0	2260.0	
OW205	570.0	2263.0	
OW205	728.0	2248.0	
OW205	730.0	2252.0	2256.0
OW205	846.0	2256.0	2259.0
OW205	856.0	2255.0	
OW205	874.0	2256.0	
OW205	904.0	2258.0	
OW205	942.0	2259.0	
OW205	982.0	2258.0	
OW205	1014.0	2259.0	2256.0
OW205	1062.0	2259.0	
OW205	1122.0	2259.0	
OW205	1124.0	2261.0	
OW205	1156.0	2258.0	
OW205	1304.0	2260.0	
OW205	1348.0		
OW205	1388.0		
OW205	1442.0	2257.0	
OW205	1650.0	2261.0	
OW205	1676.0	2259.0	
OW205	1688.0	2265.0	
OW205	1840.0	2263.0	
OW205	1966.0	2259.0	
OW205	2070.0	2261.0	
OW205	2074.0	2258.0	
OW205	2172.0	2260.0	
OW205	2174.0	2260.0	
OW205	2380.0	2258.0	
OW205	2518.0	2258.0	
OW205	2660.0	2259.0	
OW205	2730.0	2259.0	
OW205	2800.0	2258.0	
OW205	2848.0	2259.0	
OW205	2866.0	2259.0	
OW205	2942.0	2259.0	

Hole	Depth	FeOH_1	FeOH_2
OW916	382.0	2259.0	
OW916	444.0	2261.0	
OW916	480.0	2261.0	
OW916	500.0	2257.0	
OW916	780.0	2260.0	
OW916	1236.0	2258.0	
OW916	2220.0	2259.0	
OW916	2412.0	2260.0	
OW916	2490.0	2258.0	
OW916	2492.0	2256.0	
OW916	2872.0	2258.0	
OW917	538.0	2260.0	
OW917	1524.0	2261.0	
OW917	1748.0	2262.0	
OW917	1782.0	2259.0	
OW917	1852.0	2261.0	
OW917	1894.0	2259.0	
OW917	1922.0	2261.0	
OW917	1960.0	2261.0	
OW917	2042.0	2258.0	
OW917	2112.0	2259.0	
OW917	2140.0	2259.0	
OW917	2154.0	2263.0	
OW917	2182.0	2258.0	
OW917	2212.0	2260.0	
OW917	2236.0	2259.0	
OW917	2482.0	2259.0	
OW917	2532.0	2259.0	
OW917	2602.0	2259.0	
OW917	2722.0	2255.0	
OW917	2940.0	2260.0	
OW917	2986.0	2262.0	

Appendix VIII: Measured formation temperature data.

Hole ID	Depth	Temp
OW205	100.0	89.4
OW205	200.0	100.3
OW205	300.0	102.4
OW205	400.0	103.5
OW205	500.0	103.9
OW205	600.0	134.3
OW205	700.0	192.4
OW205	800.0	204.4
OW205	900.0	221.8
OW205	1000.0	226.1
OW205	1100.0	227.8
OW205	1200.0	227.8
OW205	1250.0	222.9
OW205	1300.0	221.8
OW205	1350.0	217.4
OW205	1400.0	211.4
OW205	1450.0	207.8
OW205	1500.0	205.0
OW205	1550.0	202.7
OW205	1600.0	201.2
OW205	1650.0	200.5
OW205	1700.0	199.9
OW205	1750.0	199.0
OW205	1800.0	197.6
OW205	1850.0	195.0
OW205	1900.0	195.4
OW205	1950.0	196.3
OW205	2000.0	199.0
OW205	2050.0	200.2
OW205	2100.0	208.0
OW205	2150.0	210.1
OW205	2200.0	212.2
OW205	2250.0	213.1
OW205	2300.0	213.9
OW205	2350.0	213.5
OW205	2400.0	212.2
OW205	2450.0	212.0
OW205	2500.0	212.7
OW205	2550.0	212.7
OW205	2600.0	212.7
OW205	2650.0	212.7
OW205	2700.0	212.2
OW205	2750.0	211.4
OW205	2800.0	212.0
OW205	2850.0	212.5
OW205	2900.0	212.2
OW205	2950.0	211.6
OW205	2980.0	212.2
OW205	2980.0	212.0

Hole ID	Depth	Temp
OW916	100.0	52.7
OW916	200.0	63.8
OW916	300.0	66.8
OW916	400.0	96.1
OW916	500.0	144.3
OW916	600.0	148.8
OW916	700.0	166.4
OW916	800.0	185.0
OW916	900.0	183.6
OW916	1000.0	195.1
OW916	1050.0	204.1
OW916	1100.0	196.3
OW916	1150.0	233.1
OW916	1200.0	228.8
OW916	1250.0	236.8
OW916	1300.0	241.5
OW916	1350.0	251.3
OW916	1400.0	244.1
OW916	1450.0	241.1
OW916	1500.0	242.5
OW916	1550.0	230.8
OW916	1600.0	242.1
OW916	1650.0	240.9
OW916	1700.0	245.4
OW916	1750.0	244.5
OW916	1800.0	243.3
OW916	1850.0	242.5
OW916	1900.0	241.3
OW916	1950.0	239.2
OW916	2000.0	238.6
OW916	2050.0	237.6
OW916	2100.0	236.4
OW916	2150.0	235.4
OW916	2200.0	234.7
OW916	2250.0	233.1
OW916	2300.0	233.1
OW916	2350.0	233.5
OW916	2400.0	234.1
OW916	2450.0	234.9
OW916	2500.0	235.5
OW916	2550.0	236.0
OW916	2600.0	237.2
OW916	2650.0	238.2
OW916	2700.0	239.0
OW916	2750.0	240.5
OW916	2800.0	242.3
OW916	2850.0	243.9
OW916	2900.0	254.2
OW916	2950.0	266.0

Hole ID	Depth	Temp
OW916	2980.0	273.6
OW917	100.0	106.0
OW917	200.0	110.6
OW917	300.0	110.0
OW917	400.0	110.8
OW917	500.0	110.6
OW917	600.0	158.7
OW917	700.0	194.5
OW917	800.0	211.6
OW917	900.0	226.3
OW917	1000.0	232.4
OW917	1100.0	241.5
OW917	1200.0	252.6
OW917	1250.0	254.5
OW917	1300.0	256.5
OW917	1350.0	256.5
OW917	1400.0	256.7
OW917	1450.0	253.6
OW917	1500.0	249.1
OW917	1550.0	246.1
OW917	1600.0	243.2
OW917	1650.0	240.2
OW917	1700.0	237.8
OW917	1750.0	236.1
OW917	1800.0	235.4
OW917	1850.0	234.3
OW917	1900.0	234.6
OW917	1950.0	232.0
OW917	2000.0	232.6
OW917	2050.0	232.2
OW917	2100.0	232.2
OW917	2150.0	232.6
OW917	2200.0	234.0
OW917	2250.0	232.4
OW917	2300.0	234.1
OW917	2350.0	235.6
OW917	2400.0	236.5
OW917	2450.0	236.5
OW917	2500.0	238.5
OW917	2550.0	239.8
OW917	2600.0	240.9
OW917	2650.0	241.3
OW917	2700.0	243.5
OW917	2750.0	245.4
OW917	2800.0	246.1
OW917	2850.0	248.4
OW917	2900.0	251.5
OW917	2950.0	251.5
OW917	2980.0	274.5

Appendix VIII: Illite Crystallinity values for OW-205

No of	Sample No											
pixels	726-728	842-846	854-856	872-874	978-982	1012-1014	1060-1062	1122-1124	1344-1348	1384-1388	1440-1442	1538-1542
1	1.619	1.919	1.528	1.771	1.608	1.712	1.754	1.699	1.885	1.599	1.662	1.536
2	1.686		1.599	1.702		1.840	1.894	1.720	1.737	1.634	1.762	1.535
3	1.650		1.516	1.760		1.800	1.716	1.694	**1.811**	1.501	1.672	1.581
4	1.760		1.695	1.715		1.755	1.805	1.661		**1.578**	1.616	1.529
5	1.610		1.743	1.618		2.098	1.675	1.701			1.578	1.520
6	1.619		**1.616**	1.819		2.063	1.863	**1.695**			1.576	**1.540**
7	1.736			1.701		2.178	1.749				1.557	
8	1.739			1.752		1.799	1.843				1.799	
9	1.703			1.780		1.706	1.808				1.504	
10	1.732			1.793		1.747	1.796				1.652	
11	1.647			1.743		1.772	1.832				1.638	
12	1.740			1.638		1.700	1.877				1.829	
13	1.691			1.791		1.623	1.873				1.793	
14	1.675			1.760		1.654	**1.806**				1.689	
15	1.719			1.670		1.722					1.642	
16	1.702			1.710		1.647					1.805	
17	1.711			1.724		1.829					1.853	
18	1.613			1.703		1.776					1.519	
19	1.703			1.754		**1.801**					1.565	
20	1.536			1.781							1.903	
21	1.673			1.579							1.953	
22	1.642			1.652							1.914	
23	1.550			1.698							1.756	
24	1.532			1.688							1.873	
25	1.518			1.705							1.841	
26	1.549			1.715							1.973	
27	1.580			1.692							1.902	
28	1.552			1.678							1.861	
29	1.613			1.696							1.692	
30	1.573			**1.717**							1.626	
31	1.658										1.661	
32	1.665										1.798	
33	1.546										1.818	
34	1.567										1.828	
35	1.503										1.847	
36	1.628										1.871	
37	1.589										1.842	
38	1.553										1.762	
39	1.554										1.646	
40	1.521										1.675	
41	1.590										1.610	
42	1.521										1.587	
43	1.527										1.916	
44	1.641										1.817	
45	1.602										1.816	
46	1.578										1.832	
47	1.546										1.777	
48	1.599										1.835	
49	1.599										1.802	
50	1.597										1.816	
51	1.530										1.727	
52	1.513										1.598	
53	**1.615**										1.689	
54											1.818	
55											1.579	
56											1.761	
57											1.829	
58											1.532	

Appendix VIII: Illite Crystallinity values for OW-205

No of	Sample No										
pixels	1594-1598	1646-1650	1672-1676	1700-1704	1964-1966	2066-2070	2070-2074	2168-2172	2172-2174	2376-2380	2424-2426
1	1.918	1.521	1.552	1.927	1.623	1.427	1.552	1.623	1.494	1.461	1.544
2	1.748	1.785	1.590	1.856	1.626	1.522	1.663	1.465	1.595	1.407	1.516
3	1.961	1.786	1.581	1.841	1.651	1.535	1.612	1.469	1.512	1.421	1.448
4	1.854	1.719	1.542	1.955	1.510	1.590	1.465	1.403	1.835	1.489	1.453
5	1.856	1.869	1.649	1.698	1.563	1.559	1.406	1.436	1.773	1.442	1.413
6	**1.867**	1.615	1.563	1.814	1.622	1.622	1.503	1.561	1.792	1.419	1.918
7		1.874	1.595	1.756	1.532	1.481	1.506	1.660	1.576	1.443	1.426
8		1.766	1.721	1.791	1.502	1.497	1.577	1.742	1.568	1.450	1.552
9		1.811	1.623	1.590	1.534	1.566	1.529	1.558	1.528	1.854	1.471
10		1.682	1.543	1.774	1.556	1.694	1.538	1.401	1.406	1.609	1.740
11		1.654	1.656	1.863	1.532	1.680	1.527	1.667	1.478	1.755	1.610
12		1.848	1.636	1.639	1.518	1.659	1.589	1.403	1.535	1.650	1.486
13		1.765	1.599	1.767	1.557	1.725	1.430	1.560	1.540	1.536	**1.548**
14		1.669	1.506	1.599	1.529	1.764	1.644	1.658	1.685	1.427	
15		1.683	1.607	1.695	1.648	1.671	1.747	1.940	1.682	1.556	
16		1.653	1.533	1.596	1.601	1.494	1.813	1.817	1.401	1.571	
17		1.637	1.609	1.529	**1.569**	1.472	1.645	1.768	1.496	1.626	
18		1.590	1.990	1.573		1.476	1.610	1.856	1.418	1.551	
19		1.637	1.820	**1.737**		1.616	1.731	1.920	1.488	1.434	
20		2.038	1.772			1.462	1.497	1.722	1.556	1.734	
21		1.810	1.772			1.676	1.494	1.666	1.461	1.513	
22		1.875	1.752			1.635	1.429	1.434	1.882	1.594	
23		1.932	1.724			1.526	1.591	1.745	1.826	1.466	
24		2.066	1.765			1.604	1.474	1.715	1.612	1.931	
25		1.903	1.735			1.462	1.441	1.561	1.566	1.740	
26		1.679	1.634			1.701	1.602	1.596	1.805	1.531	
27		1.997	1.566			1.473	1.537	1.507	1.800	1.662	
28		1.864	1.770			1.407	1.472	1.488	1.806	1.588	
29		1.854	1.775			1.404	1.625	1.484	1.696	1.659	
30		1.921	1.756			1.666	1.572	1.638	1.499	1.662	
31		1.814	1.749			1.567	1.552	1.664	1.501	1.662	
32		1.612	1.782			1.528	1.624	1.671	1.498	1.548	
33		1.647	1.734			1.447	1.737	1.772	1.546	1.597	
34		1.614	1.774			1.571	1.699	1.786	1.571	1.650	
35		1.969	1.700			1.420	1.580	1.607	1.468	1.473	
36		1.652	1.690			1.429	1.440	1.519	1.441	1.492	
37		1.844	1.684			1.425	1.525	1.816	1.826	1.454	
38		1.765	1.636			1.559	1.546	1.831	1.480	1.441	
39		1.572	1.792			1.552	1.702	1.547	1.557	1.545	
40		1.981	1.782			1.477	1.547	1.772	1.605	1.550	
41		1.756	1.746			1.470	1.802	1.673	1.602	1.496	
42		1.846	1.693			1.488	1.516	1.532	1.876	1.448	
43		1.823	1.760			1.467	1.645	1.432	1.863	1.474	
44		1.720	1.672			1.569	1.871	1.420	1.925	1.425	
45		1.599	1.778			1.422	1.694	1.448	1.505	1.405	
46		1.700	1.578			1.641	1.432	1.643	1.418	1.450	
47		1.737	1.657			1.467	1.506	1.643	1.571	**1.550**	
48		1.923	1.695			1.740	1.574	1.643	1.560		
49		1.646	1.548			1.524	1.699	1.452	1.836		
50		1.582	1.559			1.483	1.587	1.465	1.788		
51		1.641	**1.679**			1.474	1.588	1.844	1.792		
52		1.647				1.481	1.435	1.626	1.424		
53		1.697				1.641	1.572	1.892	1.522		
54		1.605				1.601	1.626	1.831	1.407		
55		1.666				1.538	1.650	1.885	1.404		
56		1.619				1.409	1.547	1.950	**1.605**		
57		1.792				1.487	1.771	1.872			
58		1.857				1.681	1.765	1.863			